Three dimensional multicolor *direct* Stochastic Optical Reconstruction Microscopy and Applications in Membrane Biochemistry

Inaugural-Dissertation

to obtain the academic degree
Doctor rerum naturalium (Dr. rer. nat.)
submitted to the Department of Biology, Chemistry and Pharmacy
of Freie Universität Berlin

by
André Lampe, Dipl.-Phys.
born in Herford

July 2016

Die vorliegende Arbeit wurde in der Zeit vom Januar 2011 bis July 2016 unter Anleitung von Dr. Jan Markus Schmoranzer und Prof. Dr. Volker Haucke am Institut für Chemie und Biochemie der Freien Universität Berlin im Bachbereich Biologie, Chemie, Pharmazie und am Leibniz-Institut für molekulare Pharmakologie (FMP) durchgeführt.

1. Gutachter: Dr. Jan Markus Schmoranzer

2. Gutachter: Prof. Dr. Volker Haucke

Disputation am: 21.11.2016

Affidavit

I declare that my PhD thesis entitled "Three dimensional multicolor *direct* Stochastic Optical Reconstruction Microscopy and Applications in Membrane Biochemistry" has been written independently and with no other sources and aids than quoted.

Berlin, 13.07.2016

Acknowledgments

I would like to express my gratitude to all the people who have supported, motivated and inspired me during my doctoral studies. First of all, I owe special thanks to my supervisors Dr. Jan Schmoranzer and Prof. Dr. Volker Haucke for the opportunity of performing my PhD work under their guidance and especially thank you to Prof. Dr. Volker Haucke for providing the laboratory and environment, which made the project possible in the first place.

I would like to express my gratitude to all collaborators who contributed to this thesis, no matter whether the collaboration was crested with a publication or not. Thank you to Prof. Dr. Mike Heilemann and his group for sparking the idea of spectral demixing by providing an OptoSplit II in the first place and many fruitful discussions. Thank you, also to Dr. Kathryn Poole and Prof. Dr. Gary Lewin for the opportunity to contribute to the fascinating, yet changeful STOML3 project. Thank you to Dr. Burkhard Wiesner and Dr. Anke Teichmann for the collaboration on the intriguing FCCS project on GPCRs. I also have to thank Prof. Dr. Stephan Sigrist and Dr. Marta Maglione for contribution to the setup and for challenging new ideas how to apply super-resolution, as well as Undine Hill and Prof. Dr. Achim Leutz for collaborations. I have to thank especially Prof. Dr. Markus Sauer and his group for so many fruitful discussions, Steve Wolter for the work and collaboration on rapi*d*STORM and Dr. Tobias Klamp and Dr. Gerd Wiebusch for everything they taught me about microscopes.

Furthermore, I would like to thank all members of the AG Haucke, present and past, for the great opportunity to work with such a bunch of extraordinary people. Being around all of you in this collaborative and inspiring environment was a really great pleasure. Your advice, the scientific discussions, the unscholarly conversations, your diverse characters and the good times we have shared were so important to me - you would not believe it. Thanks you to Dr. York Posor and Dr. Jasmin Podufall for the close collaboration on our imaging projects as well as to Georgi Tadeus for the great work on the software SDmixer. Special thanks, also, to the Schmoranzer's and the sub-group, the best support one can wish for when working on a microscope.

Last, by far not least, I owe my deepest thanks to my friends and the colleagues from the field of science communication. Thank you for your constant support and for always being by my side. Finally I want to thank my parents for their unconditional support and their trust in me.

I dedicate this thesis to my goddaughter Frieda Nuhanovic.

Contents

1. Summary

Fluorescence microscopes are limited by the diffraction barrier of light. This limit is ultimately defined by the wave-nature of light itself. Approximately 200 nm is the resolution limit for fluorescence microscopes using visible light, which is bigger than the size of biological structure like vesicles, viruses, membrane channels and several other vital parts of the cell. In this thesis a super-resolution microscopy approach is described, which is capable of resolving structures with sizes below the diffraction barrier. The technique is called 3D SD-*d*STORM, an abbreviation of three dimensional spectral demixing *direct* stochastic optical reconstruction microscopy. While *d*STORM is already a widely used technique, that belongs to the family of single molecule localization-based super-resolution microscopy (SMLM), spectral demixing is a novel approach to multicolor super-resolution and its development represents a major part of this thesis. When splitting the emission of a single molecule signal spectrally, a pair of localizations will be detected. Using two different fluorophores in the experiment, the ratio of the detected intensities of each localization pair should be different and allows a distinction between the two fluorophores. By this, multicolor super-resolution without registration errors or aberration is achieved. How the physical hardware for this work was set up is described in detail and the software needed to acquire and analyze the data is discussed. A conceptual introduction to spectral demixing is given and the capabilities and functionality of the software developed within the scope of this thesis to analyze the data is shown. Multicolor imaging is not the only benefit of spectral demixing, but also its noise-reducing potential is demonstrated. Furthermore, the registration error-free reconstruction and low crosstalk of multicolor data is presented. All of those three features are rarely found in other super-resolution approaches. Spectral demixing is, without any constraints, compatible with existing solutions to super-resolve structures in three dimensions. In this thesis, the approach to 3D by astigmatism with spectral demixing is demonstrated and the required temperature stabilization of the setup is discussed. The capability of 3D SD-*d*STORM is demonstrated on examples from membrane biochemistry. Cluster sizes below the diffraction barrier of stomatin-like protein 3 (STOML3) in sensory neurons could be measured and quantified, the spatial correlation of the proteins GIT1 and bas-

soon at the neuronal active zone could be depicted as well as sortin nexin 9 rich tubular structures attached to clathrin coated pits in dynamin2 depleted cells. The versatility of the setup was further demonstrated by using it as a single molecule total internal reflection microscope (smTIRFM) investigating the oligomerization-state of G protein coupled receptors on the plasma membrane of cells. Finally the 3D SD-*d*STORM is compared and positioned in relation to the multitude of current super-resolution techniques, acknowledging its novelty and advantages but not concealing the specific drawbacks, which every super-resolution approach possesses. An extensive discussion of improvements to the setup and the techniques is given, as well as a comprehensive review of potential biological targets.

2. Zusammenfassung

Fluoreszenzmikroskope unterliegen der Auflösungsgrenze, die durch die Wellennatur des Lichts selbst vorgegeben ist. Für sichtbares Licht liegt damit die kleinste, noch abbildbare Strukturgröße bei 200 nm, was größer ist als viele wichtige Teile der Zelle wie zum Beispiel Vesikel, Membrankanäle oder auch eindringende Viren. In dieser Arbeit wird ein Ansatz zur Hochauflösungsmikroskopie beschrieben, der die Abbildung von Strukturen unterhalb der Auflösungsgrenze möglich macht. Die Technik wird 3D SD-*d*STORM genannt, eine Abkürzung für das englische "three dimensional spectral demixing *direct* stochastic optical reconstruction microscopy", das sinngemäß mit "dreidimensionale, spektral entmischte, direkte, stochastische, optische Rekonstruktionsmikroskopie" übersetzt werden kann. Während *d*STORM bereits ein weit verbreiteter Ansatz ist, der zur Familie der einzelmoleküllokalisationsbasierten Hochauflösungsmikroskopietechniken (single molecule localization-based super-resolution microscopy, SMLM) gehört, ist die Idee der spektralen Entmischung ein neuer Ansatz, um mehrfarben Hochauflösungsmikroskopie zu realisieren. Die Entwicklung der spektralen Entmischung stellt einen wesentlichen Teil dieser Arbeit dar. Wenn die Lichtemission von einem Einzelmolekülsignal spektral aufgespalten wird, kann man ein Lokalisationspaar detektieren. Benutzt man zwei unterschiedliche Fluoreszenzfarbstoffe für ein solches Experiment, kann aus dem Verhältnis der Intensitäten eines solchen Lokalisationspaares eine Unterscheidung zwischen den beiden benutzten Farbstoffen getroffen werden. Dadurch kann eine mehrfarben Hochauflösungsmikroskopietechnik realisiert werden, die frei ist von Registrierungs- und Aberrationsfehlern. Wie der physikalische Aufbau für diese Arbeit gestaltet war wird detailliert diskutiert und die Software, die nötig ist um Daten aufzunehmen und zu analysieren, wird besprochen. Es gibt eine konzeptionelle Einführung in die spektrale Entmischung, sowie eine komplette Betrachtung der Fähigkeiten und Funktionalität der für die Arbeit entwickelten Software. Mehrfarben Mikroskopie ist nicht der einzige Vorteil der spektralen Entmischung, auch das Rauschreduktionspotential dieses Ansatzes wird demonstriert. Des Weiteren kann die registrierungsfehlerfreie Rekonstruktion und das geringe Farbübersprechen demonstriert werden. Diese drei Funktionen zusammen sind kaum in anderen, aktuellen Hochauflösungsmikroskopietechniken zu finden. Die spektrale Ent-

mischung ist, ohne Beschränkung der Allgemeinheit, kompatibel mit bereits existierenden Ansätzen zur hochaufgelösten Darstellung von Strukturen in 3D. In dieser Arbeit wird der Ansatz "3D durch Astigmatismus" zusammen mit der spektralen Entmischung demonstriert und die hierfür erforderliche Temperaturstabilisierung des Aufbaus diskutiert. Die Leistungsfähigkeit von 3D SD-*d*STORM wird anhand von Anwendungsbeispielen aus der Membranbiochemie verdeutlicht. Clustergrößen, unterhalb der Beugungsgrenze, vom Protein STOML3 in afferenten Neuronen konnten gemessen und ausgewertet werden. Der räumliche Bezug zwischen den Proteinen GIT1 und Bassoon in der neuronalen, aktiven Zone konnte abgebildet werden sowie SNX9-reiche, tubuläre Strukturen an CCP (clathrin coated pits) in Dynamin2-verarmten Zellen. Die Einsatzflexibilität des Aufbaus wurde auch durch die Verwendung als Einzelmolekültotalreflektionsmikroskop (single molecule total internal reflection microscope, smTIRFM) demonstriert, wobei der Oligomerisationszustand von G-Protein gekoppelten Rezeptoren (GPCRs) auf der Plasmamembran von Zellen untersucht wurde. Schließlich wird 3D SD-*d*STORM mit einer Vielzahl von aktuellen Hochauflösungsmikroskopietechniken verglichen und eingeordnet, ohne die spezifischen Nachteile zu verschweigen, die für jede Hochauflösungsmikroskopietechnik immanent sind. Eine umfassende Diskussion der Verbesserungsmöglichkeiten am Aufbau und des Ansatzes selbst, sowie eine weitgefasste Betrachtung von möglichen, biologischen Untersuchungsobjekten wird gegeben.

3. Introduction

3.1. Microscopy and biology

The fields of molecular biology and biochemistry led to precise knowledge of the weight and sizes of all kinds of proteins and molecules involved in organization and function of a cell. The spatial relationship of these basic building blocks however, is sometimes hard to study or to model from those findings, in a bottom-up manner. Complex structures like vesicles or cluster of receptors in the membrane, to name only two out of many examples, comprised of huge numbers and a vast variety of proteins and lipids, should be studied directly in the cell.

3.1.1. The diffraction barrier of microscopes

Although many important structures in a cell are complex, often these structures are too small to study them using standard fluorescence microscopy. The minimal size of an object that can be resolved by a standard fluorescence microscope is dependent on the used excitation light wavelength. This was discovered and described by Ernst Abbe in 1873 [1], and can be summarized in the equation

$$d = \frac{\lambda}{2n \sin\alpha} = \frac{\lambda}{2\,NA} \tag{3.1}$$

with λ being the wavelength of the excitation light, n the diffraction index of the medium between sample and objective, α half of the opening angle of the objective and NA the numerical aberration of the objective. This is referred to as the diffraction barrier of light microscopy. It represents a fundamental barrier originating from the wave-like nature of light itself. An ideal microscope without any distortions or aberrations will still not break the diffraction barrier.

This [1] is cited regularly in recent studies tackling imaging with a resolution below Abbe's diffraction barrier. But it should be noted that Ernst Abbes equation was formulated with an illuminated grating in mind. Since most of the more recent work in microscopy is done with fluorescent dyes, the more phenomenological approach of John

William Strutt (third Baron Rayleigh) is worth considering. In his publication from 1879 [47] he tried to define a criterion, which would provide the minimal distance for two point-like light sources to be distinguishable from each other. The Rayleigh-criterion can be written in a similar form as equation 3.1:

$$d = 1.22 \frac{\lambda}{2NA} \tag{3.2}$$

In principle, every imaging system's resolution is limited by aberration and diffraction causing blurring of the resulting image. Aberration can be minimized by the quality of the used optical elements but diffraction arises by the wave nature of light. Due to the demand for high magnification in microscopes, the apertures of objectives are rather small, since a high magnification can only be achieved by a high curvature of the lenses used in the objectives. When apertures are small the passing light will interfere with itself and will form a ring-shaped diffraction pattern, so called Airy disks [3]. The distance by which two point light-sources are separated from each other matches the distance of the Rayleigh-criterion stated in equation 3.2 (see figure 3.1 on the facing page).

Again, this is true for an ideal microscope. But no real microscope is ideal. All the imperfections of the used optics together with the diffraction barrier comprise the optical transfer function (OTF) of a microscope. This function describes how the optics project the light from the sample onto the camera. Formally, the OTF is the Fourier transform of the point spread function (PSF), which describes the response of an imaging system to a point source. The PSF is a practical way to discuss the response to a fluorescent molecule, since these have the size of a few nanometers and are very good approximated by the assumption of being a point source [160].

3.1.2. Light and the excitation of electrons

The Rayleigh-criterion (eq. 3.2) states a minimal distance in which two fluorescent ligands can be distinguished from each other. But this criterion is only true for approaches trying to gather information from a biological sample by taking just one microscopic image. There are ways to circumvent the Rayleigh-criterion, but before those are discussed a few details about excitation of electrons by light need to be covered. Light can excite electrons in atoms and molecules. A sub-class of molecules are capable of fluorescence, which will be discussed in the next section, after the basic principles of light interaction with electrons of an atom are explained.

Visible light is electromagnetic radiation and is in the spectral range between 380 nm and 780 nm and therefore in the energy range from 1.6 eV to 2.9 eV. An electromagnetic

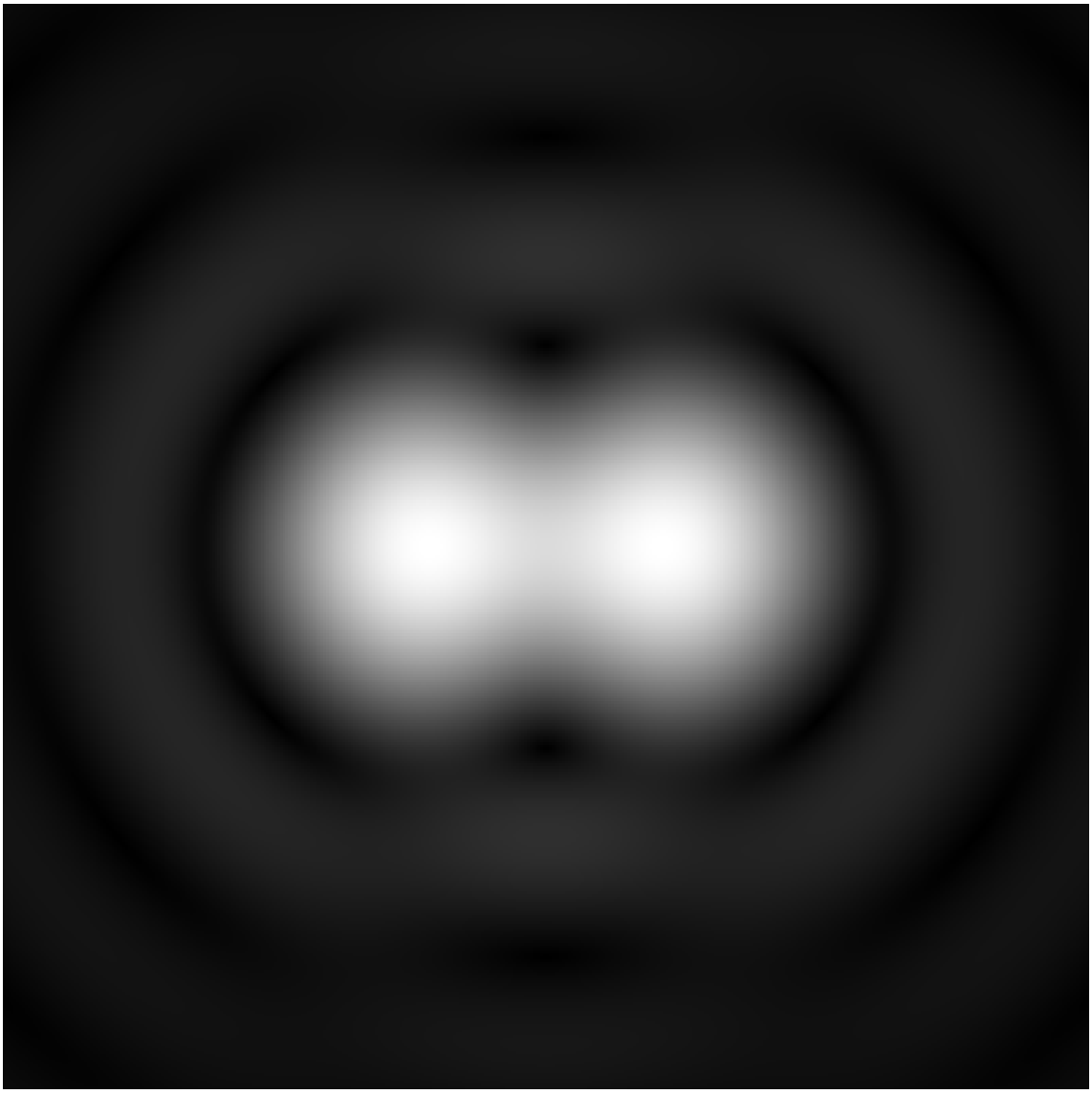

Figure 3.1.: Airy disk of two point light-sources seen through an aperture. The distance of the two sources match the Rayleigh-criterion. By Geek3 published under the Creative Commons Attribution-Share Alike 3.0 unported (CC-BY-SA 3.0). Source: https://commons.wikimedia.org/wiki/File%3AAirydisks_rayleigh_sqrt.png

wave is defined by its frequency ν, the speed of light c and the wavelength λ: $\nu = c/\lambda$. The particle nature of light, first shown by Albert Einstein in his experiments on the photoelectric effect [40], can be described with Planck's equation, which gives the energy of a single photon:

$$E = h\nu = \frac{hc}{\lambda} \tag{3.3}$$

with h being the Planck's constant. When a photon encounters a single atom, it interacts with the electron shell, given its energy is of the right value. Electrons in an atom can only be excited to discrete energy levels, and just a photon with an energy exactly matching one of those levels will be absorbed. This effect can be seen on a macroscopic level, the most prominent example being the Fraunhofer lines when observing the sun. William Hyde Wollaston and Joseph von Fraunhofer observed dark lines in the spectrum of the sun [161, 46], which could not be explained with classical physics and triggered Niels Bohr, besides other, to the development of the Bohr model, featuring discrete energy levels for the electrons in an atoms shell [21, 22]. With molecules, where the individual atoms can vibrate and rotate with respect to each other, a former discrete energy level is separated into vibrational- and rotational states. The energy differences between those are divers. Between an electronic transition the energy is in the range of 1 eV to 5 eV, for vibrational states the energy is between 0.1 eV and 0.4 eV and for the rotational states the energy is in the keV order of magnitude [65, 106, 90]. A molecule can be excited by a photon and upon emission of a photon relax back to the ground state. This process is called fluorescence.

3.1.3. Fluorescence

As already stated in section 3.1.2, the Rayleigh-criterion can be overcome. For most techniques circumventing the resolution limit (eq. 3.2), a thorough understanding of fluorescence is needed. Some approaches make use of fluorescence lifetimes or different states the electron can be excited to, enabling those techniques to extract spatial information from a biological sample with a better resolution than stated by the Rayleigh-criterion.

The mathematician and physicist Sir George Gabriel Stokes described fluorescence in 1852 [135] in a scientific way. The name fluorescence originates from Fluorite, also called Fluorspar, which is the mineral form of calcium fluoride, CaF_2. Stokes investigated this particular mineral with ultra-violet light and could detect emission of blue light. This red shift in wavelength, from shorter ultra-violet light to the longer blue light is called Stoke's shift, more precise defined as the difference between maximum of the excitation

spectrum and the maximum of the emission spectrum of the fluorescence light. The Stoke's shift is formally described as an energy difference ΔE representing the difference between excitation wavelength and fluorescence wavelength:

$$\Delta E_{Stokes} = h \cdot c \left(\frac{1}{\lambda_{exc}} - \frac{1}{\lambda_{fluo}} \right) \tag{3.4}$$

The underlying physics of this effect are only understandable with the aid of quantum mechanics, more precisely with the work of Polish physicist Aleksander Jabłoński, American physicist Edward Condon and German physicist and Nobel laureate James Franck. The Franck-Condon principle explains the intensity of vibronic transitions, which are the simultaneous changes in electric and vibrational energy levels of a molecule due to absorption or emission of a photon. Franck and Condon found that an excitation of an electron from one vibrational level into another is more likely when the vibrational wave functions overlap [45, 31]. This would represent a strict vertical ascend in energy (figure 3.2, p. 20, blue arrow) for excitation. Since vibrational states are not stable in solution and at room temperature, the first excited state relaxes to the lowest vibrational state before fluorescence occurs. By emission of a photon, the electron will go to a lower energetic state on a vertical line (figure 3.2, green arrow), hence the overlapping vibrational wave functions. The fact that an electron in the first excited state S_1 relaxes radiationless to the lowest vibrational state first, is described by Kasha's rule [76, 75] on the correlation of the spectroscopic and thermal energy differences between the fluorescence and phosphorescence levels of dye molecules. The vibrational levels in fluorescent dye molecules lie comparably close together so that upper states quickly relax to the lowest vibrational state in the electronic S_1 state before fluorescence occurs. A more vivid explanation for Kasha's rule, which is equivalent to the definition above, is that the emission wavelength of the molecule is independent of the excitation wavelength.

This can also be understood looking a the geometry of an artificial nucleus-electron system. The change to an excited state of an electron takes place on a shorter time scale (around 1 fs) than the movement of the nuclei, so that the center of mass can be assumed as fixed (Born-Oppenheimer approximation) [23]. By excitation of an electron into a higher state the dipole momentum of the molecule is changed. Since an excited state of an electron is reached in such a short time and since the maximum of the localization probability of a higher state is more distant from the nucleus than the ground state S_0, an excitation into an higher vibronic state of S_1 can be detected. The excited molecule immediately dissipates (within 10 to 100 fs) some energy as heat and the electron reaches the lowest vibrational level of the excited state [56].

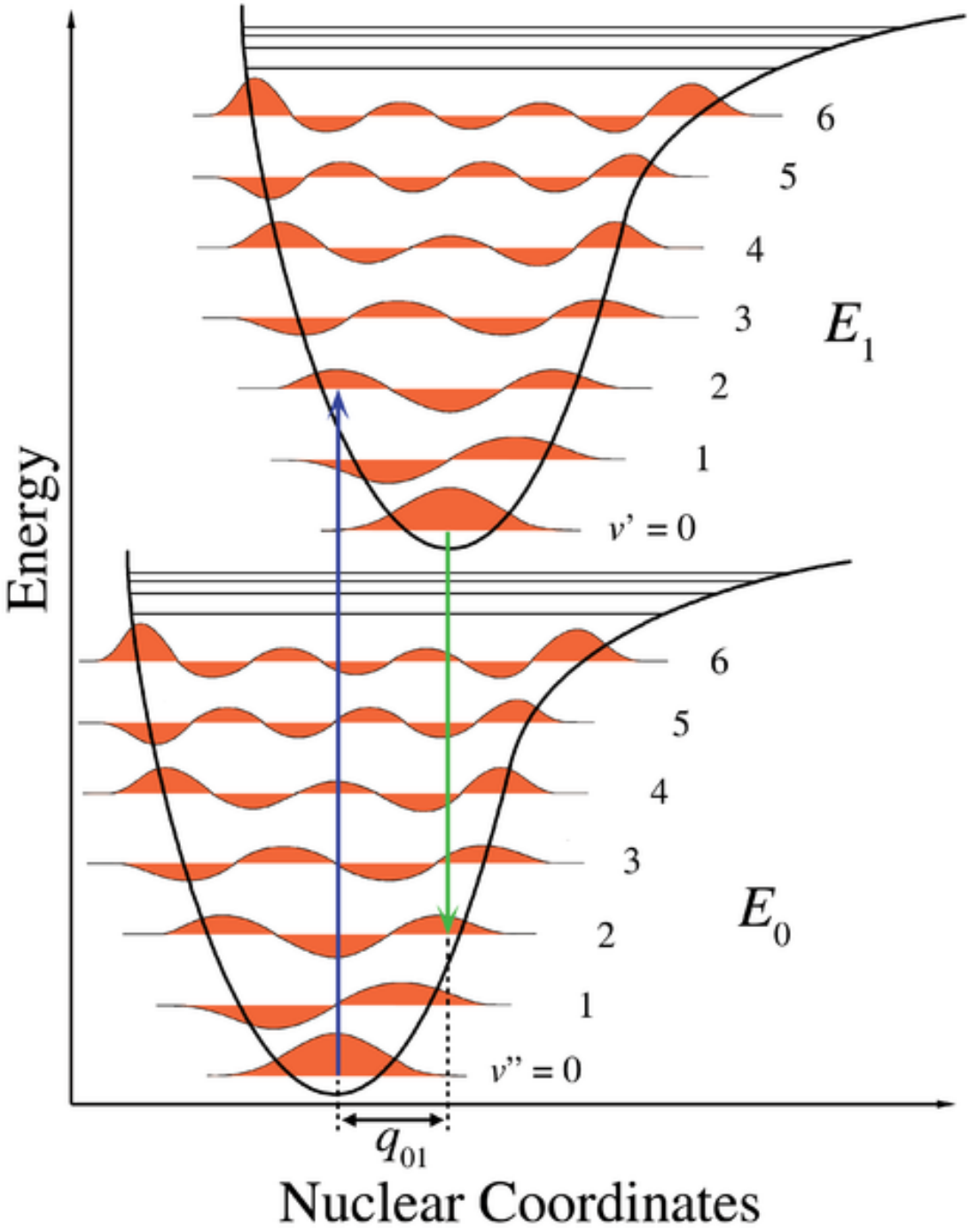

Figure 3.2.: Franck-Condon-Principle, by Samoza published under the Creative Commons Attribution-Share Alike 3.0 unported (CC-BY-SA 3.0). Source: https://commons.wikimedia.org/wiki/File:Franck_Condon_Diagram.svg

In fluorescence microscopy not only the ground state and the first excited state of a fluorophore are of interest, but also the triplet and radical states, especially in super-resolution techniques like *d*STORM. To have a schematic look at different excited states in a fluorophore the Jablonski diagram is used, named after Polish physicist Aleksander Jabłoński. In general, the Jablonski diagram illustrates electronic states of a molecule and the transitions between them [68]. Different energies are arranged vertically and the states are grouped horizontally by their spin multiplicity. Each electronic state is a thick line, which could also feature different vibrational states represented by groups of thinner lines on top of the electronic states shown in figure 3.3 on the following page. Here, also non-radiative transitions are shown, which are called internal conversion (IC) and inter system crossing (ISC). The previous explanations are a simplified representation of electronic absorption and emission processes, represented by vertical arrows. If the excited electron shows a parallel (and rectified) spin like the electron in the ground state the multiplicity M of the multi-electron system is changed:

$$M = 2S + 1 \tag{3.5}$$

where S is the resulting spin of the electrons. Since the resulting spin is the sum of the spin quantum numbers of both electrons involved and those numbers are only allowed to be $s = +1/2$ or $s = -1/2$ the multiplicity can only be $M = 1$ or $M = 3$. the first case represents the singlet states, already mentioned above, and the latter case the triplet states, if the spins of the electrons are rectified and parallel. Given that $\Delta S \neq 0$, by change of the orientation of the spin, an electron is able to make an inter system crossing (ISC) between singlet and triplet states. This change of spin orientation results in a change of the total angular momentum, which is "forbidden" according to quantum mechanics [10]. Actually the change of spin orientation takes place but on very long time scales compared to the different times within which the other described states are accessible. Relaxation from the triplet ground state T_1 to the singlet ground state S_0 occurs at a time scale of about 10^{-3} s. If this relaxation occurs upon emission of a photon, the process is called phosphorescence [84].

In summary there are two kinds of electron transfers to the ground state. On the one hand it can be a non-radiating relaxation and on the other hand it can be by emitting a photon. The ratio of these processes gives the measure of the absorbed photons to the emitted photons and is called quantum yield Φ.

$$\Phi = \frac{\Gamma}{\Gamma - k_{nr}} \tag{3.6}$$

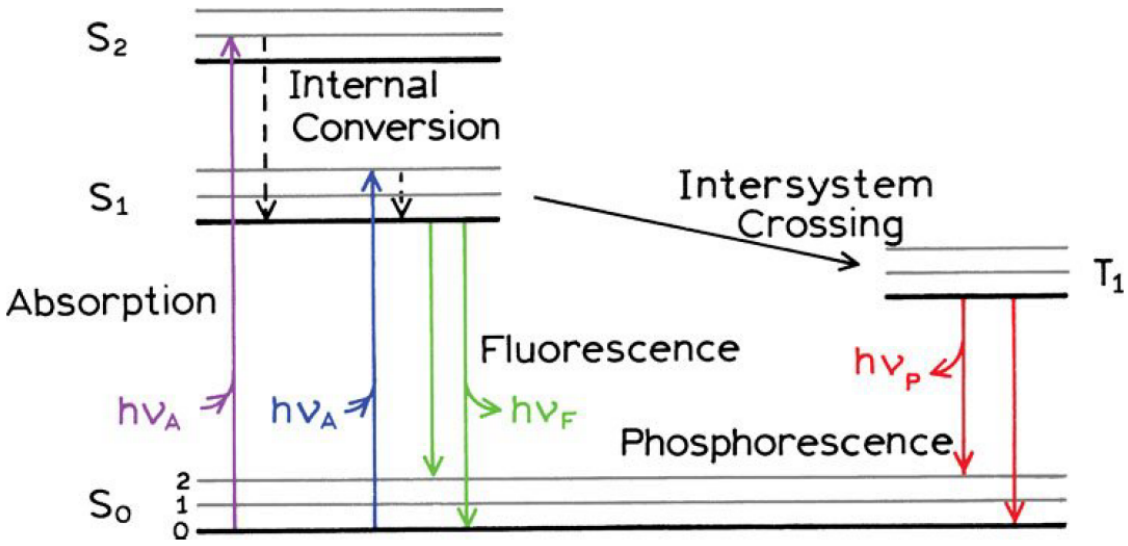

Figure 3.3.: Jablonski-Diagram [84]

where Γ is the radiative rate and k_{nr} is the non-radiative rate with Φ ranging between zero and one. Because of its long relaxation time one formally assigns the phosphorescence to the non-radiative processes in order to have a measurement in equation 3.6 for fluorescence. The average time for an excited molecule to emit its energy by fluorescence is called fluorescence lifetime and is defined as

$$\tau = \frac{1}{\Gamma - k_{nr}}. \tag{3.7}$$

The fluorescence intensity with respect to time is given by an exponential function

$$I(t) = I_0 \cdot e^{-t/\tau} \tag{3.8}$$

where I_0 is the intensity at $t = 0$ and τ the fluorescence lifetime given in equation 3.7. This states that after the averaged time τ the fluorescence intensity of an ensemble of fluorophores has dropped to $1/e$, which is about 37 % of I_0 so to speak [56, 84].

3.1.4. Fluorescent ligands

Fluorescent ligands are very diverse, ranging from small organic molecules over fluorescent proteins to semiconductor based quantum dots. The fluorescent probes used in this thesis were almost completely from the family of non-protein organic fluorophores.

All fluorophores have in common, that they possess delocalized electrons which can

be excited with photons from the visible range. Binding to a protein, for example an antibody, can be archived by the use of specific functional groups such as amino groups, carboxyl groups, thiol groups and azide groups. Some strategies, like click chemistry (azide group), can be used in living cells to label structures with internalized or membrane permeable fluorescent dyes, carrying the click chemistry counter part for a specific target in the cell [72]. The protocol for coupling fluorophores to antibodies used in this study can be found in section 4.1.4.1 on page 43. The fluorescent dyes used for super-resolution in this thesis are Alexa Flour 647, Alexa Fluor 700 and Dyomics 678. They belong to the cyanine chemical family and can also be described as carbocyanines. The molecular structures of Alexa Fluor 647 and Dyomics 678 are shown in figure 3.4.

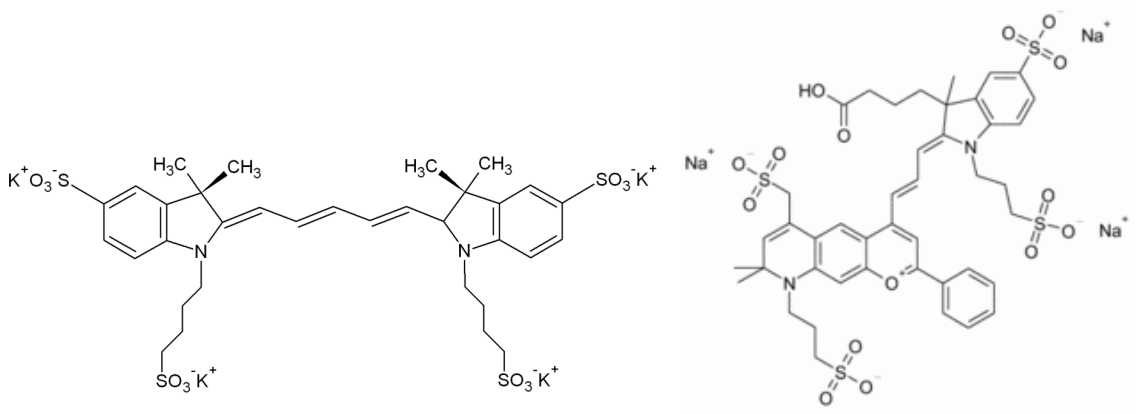

(a) Alexa Fluor 647 (b) Dyomics 678

Figure 3.4.: Structures of used organic fluorophores, provided by Life Technologies (USA) and Dyomics (Jena)

In general, fluorophores can be excited into the singlet state but also into the triplet state (by inter system crossing, figure 3.3 on the facing page). The excitation of the triplet state (T_1) can also result in photo bleaching, which destroys the fluorescence of a dye irreversibly. The T_1 state is not only long lasting, it also possesses a high photo chemical activity. A triplet state is vulnerable to oxidation and reduction processes and since fluorescence measurements are often done in water those processes take place triggered by molecular oxygen, for example. From the radical anionic state of the dye and from the radical cationic state, there are transition probabilities from each of those states, leading to the singlet ground state S_0 and also to a non-light-emitting bleached state, which is non reversible. A transition from the radical anionic state of the dye and from the radical cationic state can be achieved by irradiation with low-power 405 nm

light. As a matter of statistics an increase in the excitation intensity also increases the number of bleached dyes. An increase of the illumination time has the same effect [109].

3.2. Super-resolution - circumventing the diffraction barrier

As mentioned in section 3.1.1, many important structures in a cell are complex and often too small to be studied by standard fluorescence microscopy due to the diffraction barrier and the Rayleigh-criterion (eq. 3.2, p. 16). This can be circumvented to some degree by a variety of super-resolution approaches. The techniques can be very different from each other, but most of them are based on a fluorescence microscope. In general, a fluorescence microscope is comprised of an excitation light source, a detector, a filter-set to separate excitation and emission light, an objective and other optics. This general description can be divided into two different types, which are quite distinct from each other: A confocal fluorescence microscope and a wide-field fluorescence microscope. Both variants give rise to different approaches of super-resolution microscopy. The most prominent super-resolution approach for the confocal type is STED, which will be discussed in section 3.2.2. There are many super-resolution techniques using wide-field fluorescent microscopes, the most versatile approach is the single molecule localization-based super-resolution microscopy (SMLM), which will be described in the next section.

3.2.1. Single molecule localization-based super-resolution microscopy

The term single molecule localization-based super-resolution microscopy (SMLM) describes a category of different techniques, which differ in some details in circumventing the diffraction barrier. The most prominent member of SMLM is probably photo-activated localization microscopy (PALM), awarded the Nobel prize in chemistry 2014. More precise the honors were awarded to W. E. Moerner and E. Betzig [42, 133, 18].

It was long known that a single fluorescent molecule can be seen under a microscope [104]. However, the two-dimensional image of a point source observed under a microscope is an extended spot, an Airy disk [3] (section 3.1.1 on page 15). To identify two fluorescing point-sources as two single spots, their distance has to be equal or greater than the distance stated by the Rayleigh-criterion (equation 3.2, p. 16). In a biological sample, the labeling of the structure with fluorescent ligands is very dense, the average distance between fluorophores is usually in the range of 10 nm to 30 nm. This is far below the distance imposed by the Rayleigh-criterion to distinguish two point-sources from each other. If the distance between two fluorophores is far enough, their localizations can be found by fitting the observed emission profile to a known geometrical function, typically

a Gaussian function in two dimensions. The error of an individual measurement scales, to a first approximation, to the first square root of the number of emitted photons. The whole expression is represented by this equation:

$$\sigma = \sqrt{\left(\frac{s_i^2 + \frac{a^2}{12}}{N}\right) \cdot \left(\frac{16}{9} + \frac{4\pi s_i^2 b^2}{a^2 N}\right)} \tag{3.9}$$

where σ is the localization precision, N is the number of collected photons, a is the pixel size of the imaging detector, b^2 is the average background signal and s_i is the standard deviation of the PSF [80]. This error estimation does not account for movement or other deviation of the location or strength of the signal. If the fluorophore is bright enough, this localization-by-fitting is much more precise then the measured PSF. But a sample labeled so sparsely with fluorescent ligands that every fluorophore has a greater distance to its neighbor than the distance stated by the Rayleigh-criterion, will be insufficient to reconstruct the biological structure. From a biological point of view, the sample has to be labeled with fluorophores as dense as possible. The problem of very densely labeled samples in the SMLM techniques is solved by a virtual exchange of spacing and time. When only a subset of fluorophores is emitting light, the chances of not overlapping PSFs grow bigger, until only signals are measured with a distance greater than the distance given by the Rayleigh-criterion. When this is done in an image series with different subsets of the fluorophores in an ON state, an image could be reconstructed from all the localizations derived from that same image series. So the tight spacing of the fluorophores is circumvented by taking many images of different subsets of fluorophores in the ON state over a longer period of time. How to achieve this blinking of a small subset of fluorophores in biological samples is the main distinction between the different SMLM techniques of PALM, STORM and *d*STORM. Figure 3.5 on the following page shows the consecutive recording of fluorophore sub-sets with *d*STORM (see also figure 3.7 C, p. 31).

PALM is performed on a biological specimen, genetically altered to express photo-activatable fluorescent proteins on the structure of interest. These fluorescent proteins are driven by light between an active, ON state and an inactive OFF state. Photo-activation as well as photo-bleaching confine the life of the fluorescent proteins to a limited interval of time and a continuous emission of the fluorescent ligand is desired. Starting with most of the fluorescent proteins in the OFF state, in PALM a small subset is photo-activated and measured until this subset is completely bleached. In principle this could be exploited to count the number of fluorescent proteins in a PALM sample

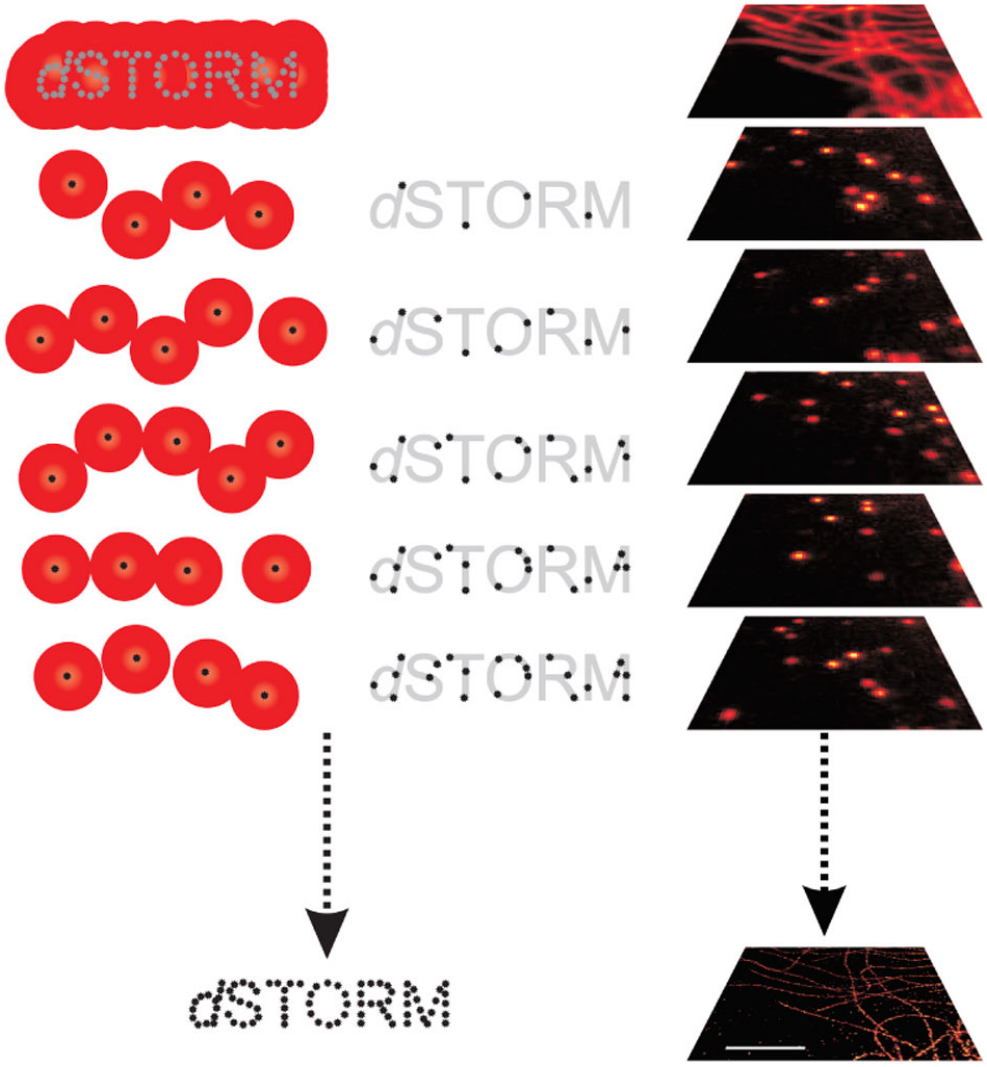

Figure 3.5.: The principle of blinking and reconstruction in *d*STORM: The target molecule of interest is labeled with photoswitchable fluorophores. Top image on the right side: labeled microtubules in a mammalian cell. At the beginning of the experiment, all fluorophores are transferred to the nonfluorescent OFF state upon irradiation with light of appropriate wavelength and intensity. Either spontaneously or photoinduced upon irradiation with a second laser wavelength, a sparse subset of fluorophores is reactivated. If the probability of activation is sufficiently low, then the activated fluorophores residing in their ON state are statistically spaced further apart than the resolution limit and their positions can be precisely determined. Repetitive activation, localization and deactivation allow a temporal separation of spatially unresolved structures in a reconstructed image (image below). Scale bar: 2 µm (modified from [128]).

[49, 8, 87].

Stochastic optical reconstruction microscopy (STORM) uses immunolabeling of the sample with antibodies. The secondary antibodies are labeled with an acceptor and reporter fluorophore set [101, 97]. The reporter fluorophores are pushed into a radical state, which is a long lasting state, because it is only accessible via the triplet state (figure 3.6). Then, a low power laser pulse is used to excite a subset of the acceptor fluorophores, leading to a change in the state of the reporter fluorophore to S_0. This activated subset of reporter fluorophores (usually Alexa Fluor 647) can be excited with a laser and the signal is used for single molecule localization. For STORM a buffer depleted of O_2 by enzymes and supplemented with a reducing agent is needed to prolong the radical, dark states of the reporter fluorophores.

The word "direct" in *direct* stochastic optical reconstruction microscopy (*d*STORM) referrers to the approach of achieving the single molecule blinking by the buffer alone, without the use of a pair of fluorophores as activator and reporter dye [57]. A buffer completely depleted of O_2 and containing a reducing agent together with a strong, initial wide-field illumination of the sample ($\sim$2 - 5 kW/cm^2) will push the majority of the fluorophores into an OFF state, leaving only a subset of fluorophores in their ON state. The latter is the fast cycling between the S_0 state and the S_1 state, due to the high excitation power-density (see figure 3.6). The blinking rate is not only adjustable by buffer conditions but can also be fine-tuned by low-power continuous wave irradiation with 405 nm (for red and far red dyes) or by pulsed, low-power 405 nm laser irradiation. How an image is reconstructed using *d*STORM is shown in figure 3.5 on the preceding page. It was debated whether the nature of the OFF state of the fluorophore is the triplet state T_1 in combination with the radical states or whether the OFF state is only comprised of the radical states F^{*+} and F^{*-} and only reached via the triplet state (figure 3.6). In 2011 it was shown by van de Linde et al. [151], that the dark state of organic fluorophores is in fact only the radical states by means of electron paramagnetic resonance (EPR) spectroscopy. In contrast to PALM, where the imaged fluorescent proteins are bleached and, therefore, lost, most of the fluorophores in the *d*STORM approach return from the OFF state. This repetitive blinking leads to a higher density of single molecule localizations and a reconstruction which is more reliable. On the other hand, the theoretical ability to count, as described for the PALM technique above, is not possible, since the single molecule localizations are indistinguishable from each other.

Another variant of the SMLM approach would be uPAINT, which is short for universal Point Accumulation for Imaging in Nanoscale Topography. Here, the blinking is achieved by continuous labeling of membrane bio-molecules. A surplus of fluorophore-coupled

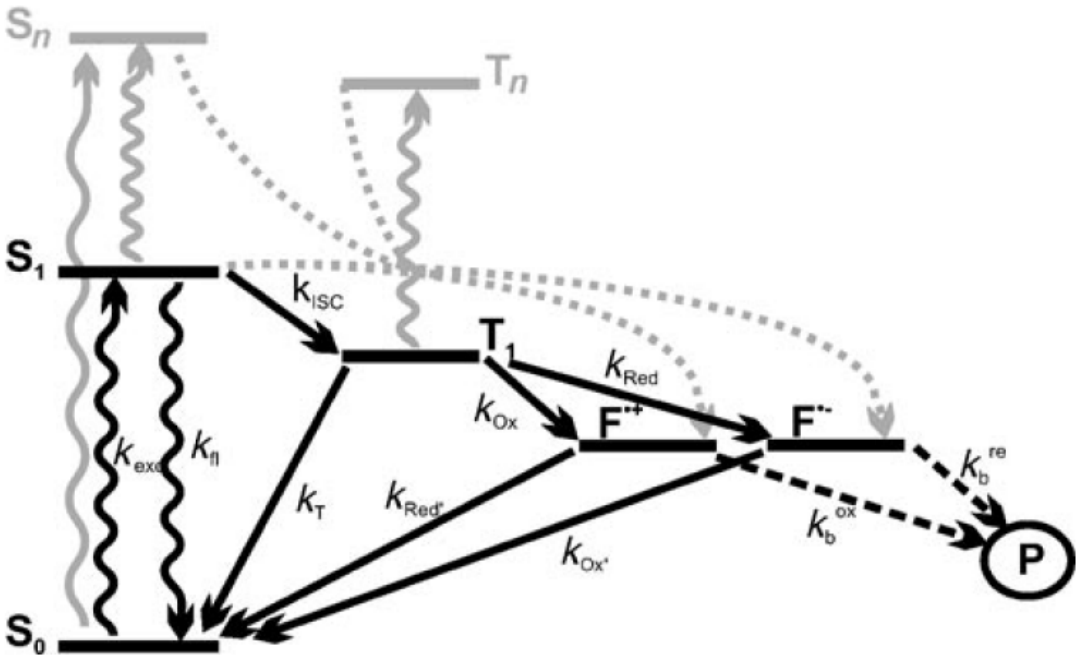

Figure 3.6.: Extended Jablonski diagram. Singlet (S_n) and triplet (T_n) states are also shown as well as the radical states (F^{*+}, F^{*-}) and the photo-bleached state (P) of a fluorophore. The different rate constants are indicated as k with different indices. Modified from [153].

antibodies or nanobodies in a large volume is in contact with the sample, and consecutive binding of those fluorescent ligands is adjusted to be so sparse that single molecules can be detected individually and even be tracked [50].

The technique of ground state depletion microscopy followed by individual molecule return (GSDIM) is very comparable with the approaches of STORM and *d*STORM. The difference was that the blinking was not induced by the buffer and relied on naturally occurring blinking of fluorophores when irradiated with higher (compared to STORM/*d*STORM) laser powers. This led to more photo-bleaching and a lower single-molecule localization density. Also, in contrast to the other techniques, it states that the triplet state of a fluorophore has to be recognized as the OFF state [24], which is debatable after the publication of van de Linde et al. in 2011 [151], showing that the dark state of organic fluorophores are in fact only the radical states by means of electron paramagnetic resonance (EPR) spectroscopy.

3.2.2. Stimulated emission depletion

The approach of stimulated emission depletion (STED) to circumvent the diffraction barrier was awarded the Nobel prize in chemistry 2014. The idea is to shrink the effective excitation volume of a confocal scanning microscope to a size below the diffraction barrier. This is achieved by using stimulated emission, a core principle of laser technology already formulated by Einstein [41]. Stimulated emission is the effect, when an excited electron is passed in close proximity by a photon of an energy within the wavelength range of this excited state of the electron. This forces the electron to relax to the ground state by emitting a photon of the same wavelength and phase of the passing-by photon. In STED a second laser with a wavelength at the far end of the emission spectra of the used fluorophore is coupled into the beam-line of the excitation laser in a doughnut-like shape, leaving a tiny area in the middle of this combined beam without the stimulated emission effect (see figure 3.7 B, p. 31). The excitation beam does not need to be shaped in a special way. All fluorophores outside the small area in the middle are excited and immediately depleted of their energy by stimulated emission of the doughnut-shaped second beam [78, 121]. This combined beam of light is used in a confocal microscope setup and its fluorescence is detected by an avalanche photo diode (APD). To produce an image x and y coordinates are then scanned step by step [115]. As the light passes through a pin-hole at the focal point in front of the APD off-focus light will not be detected by the APD.

The achievable resolution of STED is around 50 nm laterally and 120 nm axially, inferior to most SMLM approaches. Also, the power-density applied to the sample is

higher compared to most SMLM techniques enhancing the risk of photo-bleaching and photo-damage of the biological structure. The big advantage of STED is the fact that is does not need any post-processing as SMLM or SIM do, so the super-resolved image is immediately visible after acquisition.

3.2.3. Structured illumination microscopy

The wide-field structured-illumination microscopy technique (SIM) is also called patterned illumination. The resolution with this technique is enhanced by measuring Moiré fringes [157] caused by the interference of the illumination pattern and the sample [26, 54]. Mats Gustafsson, a pioneer in the field of SIM, summarized: "Otherwise-unobservable sample information can be deduced from the fringes and computationally restored." [55]. The increase in spatial resolution is achieved by collecting information from the frequency space outside the observable region. The Fourier transformation of a SIM image contains superimposed additional information from areas of reciprocal space. Many images are acquired by shifting and rotation of the structured illumination. Combining those images and revers-transforming the resulting image back from Fourier space will give the super-resolved image (see figure 3.7 A, p. 31). The technique relies on extensive post-processing of the acquired data and achieves a resolution of 100 nm lateral and about 250 nm in z-direction [127]. The huge advantage to every other super-resolution technique is the potential simultaneous use of four lasers, delivering four color super-resolved images with one acquisition.

3.2.4. Other approaches

Several other approaches exist to circumvent the diffraction barrier. The near-field scanning optical microscope (NSOM) operates in the near-field where resolution is not limited by diffraction but by the size of the used aperture. This means that the tiny tip aperture has to be only nanometers away from the molecule it wants to measure. The approach is complicated from a technical point of view and is limited by the number of photons capable of passing through a tip aperture with the size of only a few nanometers [37, 164]. To increase the number of photons aperture free NSOM (ANSOM) has been developed. It uses a tip very close the the fluorophore to only enhance the local electric field that interacts with the fluorophore [43]. This approach can be enhanced further by the use of bow-tie nanoantennas [111, 112].

Somehow misleading is the name of a technique operating in the far-field with the name near-field optical random mapping microscopy (NORM). This technique observes the

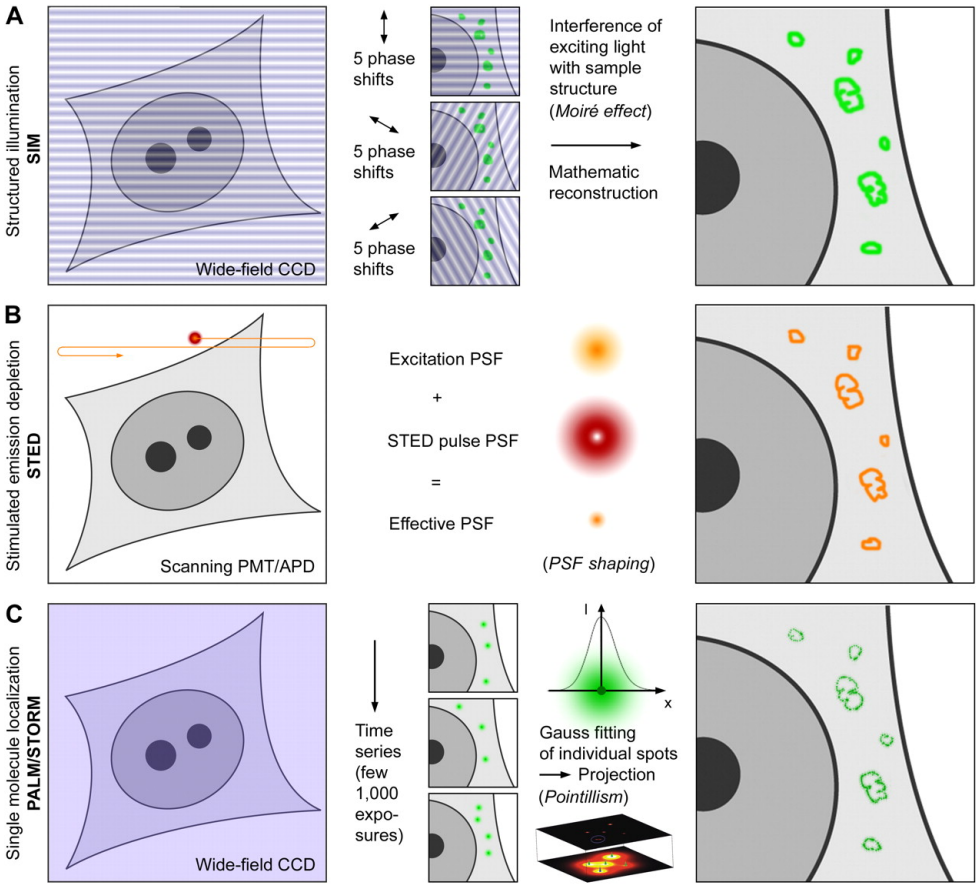

Figure 3.7.: Super-resolution imaging principles. (A) In SIM the sample plane is excited by a non-uniform wide-field illumination. This combines with the sample information originating from structures below the diffraction limit to generate moiré fringes. The image detected by the CCD camera thus contains high spatial frequency sample information shifted to a lower spatial frequency band that is transmitted through the objective. A mathematical reconstruction allows, from a series of 15 raw images per slice, to reconstruct a high-resolution image with doubled resolution in xy compared with wide-field resolution. (B) In STED microscopy the focal plane is scanned with two overlapping laser beams. The first laser excites the fluorophores, the second longer wavelength laser drives the fluorophores back to the ground state (stimulated emission). A phase plate in the light path of the depletion laser generates a donut-shaped energy distribution, leaving only a small volume from which light can be emitted that is then being detected. Thus, the PSF is shaped to a volume smaller than the diffraction limit. (C) SMLM assures that only a relatively low number of fluorophores are in the ON state. These molecules are detected on a CCD camera as diffraction-limited spots, whose lateral position is determined with very high accuracy by a fit. Single molecule positions from several thousand raw images are then used to reconstruct an image (modified from [127]).

Brownian motion of nanoparticles in an immersion liquid by using a far-field microscope. Many images of the same region are collected to map the intensity shifts derived from those image series [102].

4Pi microscopy could be described as a progenitor of STED (see section 3.2.2). A 4Pi microscope is set up as a laser scanning microscope with two opposed objectives and the possibility to illuminate the sample coherently and, by this, the axial resolution can be reduced from typical 500 - 700 nm to 100 - 150 nm [58]. This can be done in combination with the STED technique.

Super-resolution optical fluctuation imaging (SOFI) is closely related to SMLM approaches without the need for PSF fitting by directly computing the temporal autocorrelation of pixels in an acquired image series. It can be superior to SMLM techniques only when the density of active fluorophores is higher than typically used in SMLM [137, 48].

3.3. Labeling density and sampling rate in SMLM

The approach of single molecule localization-based super-resolution microscopy (SMLM, see section 3.2.1) was explained by an abstract thought-experiment: If the fluorophores used to label a biological structure are so far apart that the emitted signals are not overlapping, the localization of those fluorophores can be determined by a Gaussian fit (equation 3.9 on page 25), which is only dependent on the number of photons and not on the diffraction barrier of the microscope (section 3.1.1 on page 15). Such a sparsely labeled sample would not be useful to address biological questions. Therefore, the concept of blinking has been established, where only a subset of fluorophores is in the ON state at a given time. This enables an analysis of densely labeled samples. It could also be referred to as an exchange of space and time, since a spatial problem, not being able to localize every light emitter without overlapping PSFs, is solved by taking many images of non-overlapping PSFs of fluorophores over an extended period of time.

The statement that a sparsely labeled sample would provide almost no information about the sample is not far fetched. But for super-resolution approaches a not so obvious question has to be asked: How densely labeled a sample has to be to gain structural information? The basic principles to answer this question are defined by the Nyquist-Shannon sampling theorem, named after electronic engineer Harry Nyquist and mathematician and electronic engineer Claude Elwood Shannon [51]. Originating from the field of digital signal processing, the theorem made a connection between continuous-time signals and discrete-time signals. The theorem only applies to a class of mathematical

functions, whose Fourier transform is not zero in a finite region of frequencies. But it makes a statement that can be interpreted for the labeling density of samples in super-resolution microscopy. The Nyquist criterion is defined as the inequality

$$B \leq f_S/2 \tag{3.10}$$

where f_S is the sample rate and B is the bandlimit [129]. The analogon in fluorescence microscopy would be a continuous biological structure that has to be "sampled" by discrete fluorescent molecules on said structure. In contrast to digital signal processing, for fluorescence microscopy there is a limit, an effective sampling rate, given by the diffraction barrier of microscopes (section 3.1.1). For non-super-resolution microscopy a labeling density of the sample with lower distances between fluorophores than stated by the Rayleigh-criterion (see equation 3.2) will not gain more information about the structure, since the fluorophores are not distinguishable from each other below that distance. Typical distances are around 200 nm, which is easily achievable by antibody staining. However, for super-resolution the labeling density of the sample has to be higher to "encode" all structural information in the resulting, super-resolved image. SMLM techniques are capable of resolutions of about 20 nm [101, 57, 42], implying that a labeling density of at least 10 nm has to be reached to gain the maximal structural information from the sample. This is a definition for the one dimensional case. Since biological samples are comprised of two dimensional (e. g. approximation for the plasma membrane) and three dimensional structures, a mean distance of 10 nm for every spatial direction has to be achieved. This imposes a problem as the standard staining protocols for labeling biological structures use a primary and a secondary antibody, measuring more than 10 nm as a complex. Nonetheless a sufficient labeling density can be achieved, because most targets are on the surface of a larger structure (e. g. clustered receptors on the plasma membrane). Then, the structures can be labeled densely enough, since the dimensions of interest are confined to the two dimensional surface the target it is bound to. In contrast to PALM, all other SMLM techniques can not directly measure the mean distance between individual fluorophores, since they are indistinguishable from each other [133, 130, 83]. The STED or SIM approaches are not single molecule methods, so this question is not even addressable.

3.4. Multicolor and three dimensions in SMLM

3.4.1. Multicolor

The techniques STORM/*d*STORM, PALM and GSDIM can all be summarized to SMLM (section 3.2). There are examples for successful multicolor application for every variant of SMLM approaches [97, 133, 24, 57]. Every cited example was groundbreaking in terms of improved resolution but the multicolor capability of each approach was adapted from the standard techniques of fluorescence microscopy. Especially when applied to co-localization experiments, errors in color separation and multichannel registration impose a serious problem, since those errors are in the order of magnitude of the achievable resolution. Color separation errors are usually caused by wrong color assignment to localizations, in standard fluorescence microscopy termed as bleed-through or color crosstalk. This is due to the standard concept of a filter set defining the color as it was used for decades in fluorescence microscopy. A color is assigned to the acquired image by the filter set is was taken with. In the special case of STORM [97], which uses pairs of fluorescent dyes, different dyes for excitation and a single one for read-out (reporter), the problem is not even assessable by measurement. This approach circumvents the problem of multichannel registration, since the read-out channel is always the same and color differs only by activation, but there is no chance to identify a falsely activated reporter. To engage this problem, rather complicated correction algorithms are used [16].

Registration errors originate from chromatic errors in the optical path, especially from image distortion by different dichroic mirrors to separate colors, but also by focus mismatch [113]. These errors grow bigger the further apart the emission wavelength of the used fluorophores are. Most of the multicolor SMLM approaches employing sequential illumination of spectrally separated fluorophores, but they rely on error-prone alignment procedures of the different channels, either based on manual correction, semi-automatic correction using fiduciary markers or self-similarity recognition algorithms [144, 7, 150, 16, 71]. All those approaches introduce an error between channels into the data set, at least in the range of 10 nm, which is about half the minimal localization precision of the listed techniques and should be taken into account, especially in co-localization experiments. But also simultaneously excited fluorophores are used to achieve multicolor by a dichroic emission splitter in the detection pathway to distinguish the probes by their emission spectra [85, 13, 24, 71]. A vast variety of the physical setup, precision of the alignment, technical procedure and ability to separate the color channels can be found here. In most cases not all issues from registration errors to color crosstalk are discussed, some even suffer from quite high crosstalk between the color channels or

calculate the crosstalk from one channel to the other only, and not back and forth.

Since all SMLM techniques are based on the idea of reconstructing an image point by point, based on localization obtained from the detection of single molecules, the opportunity arises to rethink also the concepts of color separation and multichannel registration. The need to separate (or identify) different fluorophores by emission filters, which was a basic prerequisite of conventional fluorescence microscopy, can be achieved differently. Since only single localizations have to be assigned to a specific fluorophore and not an image of the entire field of view, the color assignment could also be done individually. One possibility is to separate the emission of two fluorophores, which are spectrally well distinct, but are overlapping in their emission to a certain extend. When splitting the emission of both fluorophores, a pair of localizations will be detected by the camera. In theory, the ratio of the detected intensities of each localization pair should be different and allow a distinction between the two fluorophores. This approach is called spectral demixing and its advantages and disadvantages will be discussed in detail in chapter 5.2.

3.4.2. Three dimensions

Given the idea of localizing signals from individual fluorescent molecules in every SMLM technique, it is worthwhile to think about what one gains in addition to a resolution below the diffraction barrier. The raw image sets contain the lateral position of fluorescing molecules clearly distinct from each other, since not overlapping signals are mandatory for determining the x- and y-positions of each molecule. In 2008 Bo Huang presented the idea of astigmatism to the SMLM approach [20]. By introducing a cylindrical lens into the detection pathway of the microscope, the image of each localization is distorted with respect to its axial position as shown in figure 3.8 on the following page.

But determining the z-position of a localization from transversal distortions of the image can be done in different ways [118]. The approaches of double-helix PSF [114] and phase ramp imaging localization microscopy (PRILM) [12], can be categorized as lobe splitting approaches, since the PSF is split into two lobes whose relative position encodes the position in z-direction. Then there is the technique of splitting the emission light equally and project it onto two cameras or side by side on the same camera. The focal planes in each light path are set in such a way that they differ by a few hundred nanometers enabling the recording of two section of the PSF with known offset in z-direction and the reconstruction of axial positions. This approach is called biplane [96]. But since the technique of 3D SD-dSTORM uses astigmatism to access information in z-direction only, this is discussed in more detail.

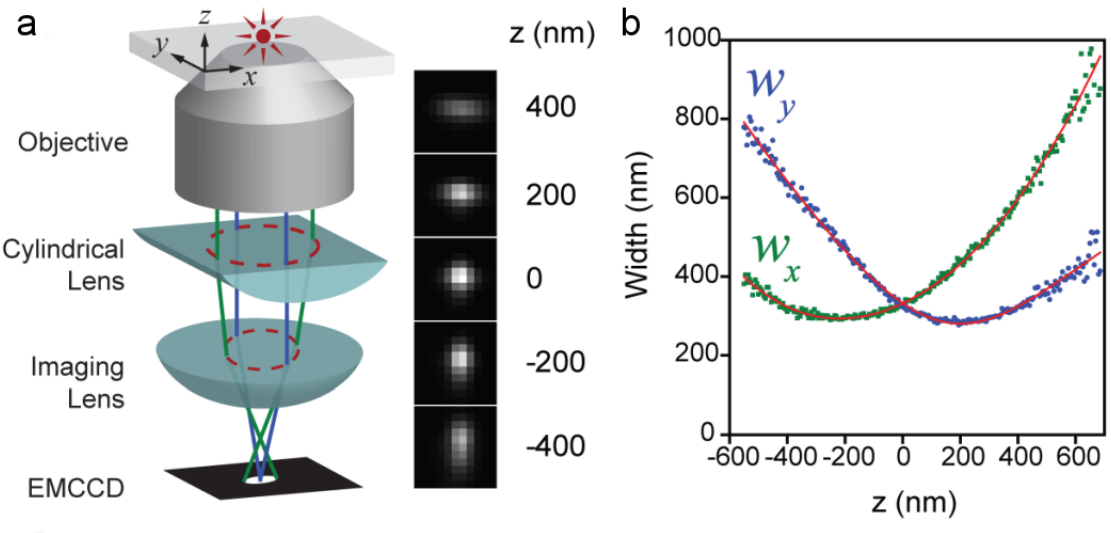

Figure 3.8.: Concept of 3D by astigmatism. a) simplified optical diagram of determining the z-position of a fluorophore from the distortion of the image in x and y by introducing a cylindrical lens into the detection pathway. Individual images of a fluorophore with its corresponding positions in z are shown on the right. b) Calibration curve as described in [19, 20], width of the localization w_x and w_y as functions of z (modified from [20]).

We used the software rapi*d*STORM to localize single molecule signals. The authors of rapi*d*STORM explained in Proppert et al. [118] different strategies of decoding z-positions from a Gaussian approximation, that correlates to the following equation (see also equation 3.9):

$$G = B + \frac{A}{2\pi\sigma_x\sigma_y} \exp\left[-\frac{1}{2}\left(\frac{(x-x_0)^2}{\sigma_x^2} + \frac{(y-y_0)^2}{\sigma_y^2}\right)\right] \tag{3.11}$$

The so called sigma-difference look-up, estimates σ_x and σ_y from a calibration data set with known z-positions, indexed by $\sigma_x - \sigma_y$ [122], the quadratic approximation suggested by Holtzer et al. [61] was derived from physical assumptions about PSF broadening. This led to the quintic approximation used by Huang et al. [20] (see also figure 3.8) with correction terms up to the fourth order to correct for imperfections of the optics. In the software rapi*d*STORM the z-coordinates of a localization are derived from a cubic basis splines (cubic B-splines) approximation, which is equally or better performing in terms of localization precision than the approximations mentioned before [118].

3.5. Limitation of current super-resolution approaches

As described in section 3.2, there is more than one way to get a resolution below the diffraction barrier with a light microscope. Since the scope of this thesis encompass SMLM techniques, the limitations of those are discussed in more detail. Nevertheless, approaches like STED (section 3.2.2 on page 29) or SIM (section 3.2.3) are worth to compare to.

First of all, it should be noted that no super-resolution technique is "breaking" the diffraction barrier, it is rather a circumvention with several different trade-offs, depending on the used technique. Therefore, some approaches are suited better for special tasks, while other tasks are not accessible at all or only with enormous effort and some drawbacks.

When approached from the point of view of a biologist, SIM is the technique with the least drawbacks and the most versatile of all of the super-resolution techniques. Tasks like live cell imaging, four color experiments and 3D could in theory be combined with this technique [147]. Combining all of those task is a challenging endeavor but could be done with the right choices of fluorescent ligands and the right strategy. However. the fact that the technique is only providing a resolution of about 100 nm laterally and about 250 nm in z-direction is a drawback compared to other super-resolution approaches, which are all capable of achieving a better resolution. Additionally, SIM images are reconstructed after

acquisition by a high demanding algorithm. On one hand, this leaves the opportunity to apply refinement filters to the raw data before post-processing, on the other hand, the resulting images are only viewable after processing for five to fifteen minutes.

Waiting for an image to be processed is not an issue when using STED. This is the only technique, which is able to show the results of a measurement immediately, clearly an advantage to other super-resolution approaches. But the drawbacks are numerous. Considering the name stimulated emission depletion, the strain applied to the used fluorophores is huge. Not only that the power density of the combined beams of excitation light and STED-beam are in the range of megawatts per square centimeter, orders of magnitude higher than every other technique, but the fluorophores are excited and depleted more often than the emission light originating from them is used for the resulting image. It has been shown that STED is capable of 3D imaging [110] with a claimed resolution of about 40 nm laterally and about 95 nm in z-direction, calculated by averaging many measurements, though. The accessible range in z-direction is confined by a couple of hundred nanometers, hence the effects of photo-bleaching by applying such high laser-powers. This would place STED between SIM with a lower resolution and SMLM approaches with higher resolution. The capability of STED to do imaging with two colors has been shown as well as application in living cells [36], but with lower resolution and more focusing on the general structure than on cell dynamics. The used high lasers powers make it a difficult task to even find two fluorophores that work well for multicolor imaging. The immediate nature of the technique, involving no post-processing, also inhibits considerations to advance the technique by the more and more evolving computational sciences, which is not the case for SIM or SMLM approaches.

Since SMLM approaches are only different in the way they achieve blinking and their probes, it makes sense to look at SMLM in general. In most cases the SMLM techniques are capable of two colors. Applications with more than two colors have been demonstrated but are far away from being used regularly. Different strategies exist for three dimensional imaging (section 3.4.2) with a resolution between 50 nm to 70 nm in z-direction, down to about 10 nm with some special approaches leading to even more drawbacks [73]. However, the range in z-direction is confined to about 0.8 µm to 1.4 µm. Imaging several slices and combining them to a larger image in z-direction was hardly ever done, due to loss of a huge portion of fluorophores still capable of blinking after imaging the first z-stack. This happens not only due to the fact that photo-bleaching is occurring (wanted in PALM, not avoidable in the other approaches) but also due to the need of even more localizations for a decent 3D reconstruction compared to 2D. This is discussed in more detail in section 5.3 on page 72. All SMLM techniques have in

common, that an additional color could be added, which is not super-resolved and can aid to set the biological question addressed by super-resolution into perspective. Also, every SMLM approach was demonstrated to be suitable for live-cell imaging [52, 83, 130]. But, as in the STED approach, most techniques are not able to super-resolve dynamical aspects in live-cell imaging, except for some tracking variants of uPAINT, *d*STORM and PALM. The latter approaches are able to measure more dynamic aspects of live-cells, but the simultaneous, super-resolved static structure to go with the recorded tracking data is often not achieved. However, the SMLM approaches feature the highest achievable resolution amongst all of the super-resolution techniques, in some cases, involving acquisition times over an hour, a resolution in the single digits nanometer range in biological samples was demonstrated. In addition to this, the SMLM approaches can provide data on positions of individual molecules, as well as distances between them. This is a big advantage, since all other approaches can not access this information. The disadvantage of long post-processing can be overcome by faster algorithms and ultimately by faster computers. By applying more sophisticated analysis ideas to the post-processing procedure, as demonstrated here with SD-*d*STORM, further improvements and a variety of new strategies for SMLM techniques are possible.

For every technique, the dose of high intensity light to a sample has to be considered, especially in life-cell experiments. Just recently a study investigated this: Wäldchen et al., "Light-induced cell damage in live-cell super-resolution microscopy" [156]. In conclusion, from a biological point of view, looking at super-resolution techniques could be a depressing task. Most of the time the circumvention of the diffraction barrier, achieving a higher resolution in a biological sample, comes with major drawbacks on the experimental side: higher light dosage, lower temporal resolution, the need for special probes and buffer condition, to just name a few. To address a biological question with super-resolution is deemed to be a time-consuming task, with several technical obstacles to overcome. The field of super-resolution with light microscopes is overlapping with biology, chemistry, physics, computer science and engineering alike and is a good example for the blurred lines in the life sciences between fields. However, super-resolution microscopy grants access to parameters and resolutions, which were not approachable by any measurement technique before. In spite of every drawback, described in the paragraphs above, super-resolution microscopy is a new tool to investigate the building-blocks of life itself and is about to close the resolution gap to electron microscopy. And to put all limitations and technical difficulties to circumvent the diffraction barrier into perspective, there is a saying, which origins are unknown: "There is no such thing as a free lunch".

4. Materials & Methods

4.1. Materials

4.1.1. Chemicals and consumables

Chemicals and consumables were purchased from GE Healthcare (Freiburg), Gibco (Eggenstein), Greiner (Solingen), Life Technologies (Gaithersburg, U.S.A.), Merck (Darmstadt), Roth (Karlsruhe), Serve (Heidelberg), Sarstedt (Nümbrecht), Schott (Mainz), Sigma-Aldrich (St. Louis, U.S.A.), Thermo Scientific (Schwerte) and Dyomics (Jena).

4.1.2. Tissue culture

4.1.2.1. NIH 3T3 cell line

The 3T3 cells originated from a cell line established in 1962 by George J. Todaro and Howard Green [145]. The cell line has become the standard fibroblast cell line and was obtained from Swiss albino mouse embryo tissue. The prefix NIH is short for National Institute of Health and was added to specify where the originating cultures are kept. They were kept in DMEM containing fetal calf serum as described in table 4.3.

4.1.2.2. BS-C-1 cell line

BS-C-1 cells were derived from the kidney of the African green monkey [62]. They were kept in DMEM containing fetal calf serum as described in table 4.3.

4.1.3. Antibodies

Target	Host	Supplier/Source
α-tubulin	M	Sigma
tubulin	M	Epitomics
phosphotyrosine	Rb	BD Transduction Laboratories
clathrin heavy chain	Rb	Abcam
AP-2α	M	Hybridoma cell line
anti-mouse Alexa Fluor 488		Life Technologies Inc (USA)
anti-mouse Alexa Fluor 647		Life Technologies Inc (USA)
anti-rabbit Alexa Fluor 647		Life Technologies Inc (USA)
anti-mouse Alexa Fluor 700		Life Technologies Inc (USA)
anti-rabbit Alexa Fluor 700		Life Technologies Inc (USA)
unlabeled anti-mouse	Dk	Jackson ImmunoReasearch Laboratories Inc
unlabeled anti-rabbit	Dk	Jackson ImmunoReasearch Laboratories Inc

Table 4.1.: Table of used antibodies

4.1.4. Fluorescent ligands

Name	Supplier
Alexa Fluor 647	Life Technologies Inc (USA)
Alexa Fluor 700	Life Technologies Inc (USA)
Alexa Fluor 488	Life Technologies Inc (USA)
Dyomics 678	Dyomics (Jena)
vector plasmid pEYFP-N1	Clonetech

Table 4.2.: Table of used fluorescent ligands

The fluorophores used for SD-*d*STORM are Alexa Fluor 647, Dyomics 678 and Alexa Fluor 700 (see table 4.2, page 42). The fluorophore Alexa Fluor 647 only differs by two sulfur side-chains from the widely-used fluorescent dye Cy5 [105]. Alexa Fluor 647 possesses a quantum yield of $\Phi = 0.33$, a molecular weight of 1300 g/mol, a fluorescence life time of $\tau = 1.04 \cdot 10^{-9}$ s in water and an extinction coefficient at the maximum of the absorbance of $2.5 \cdot 10^5$ $\mathrm{mol^{-1}cm^{-1}}$. The Stoke's shift of Alexa Fluor 647 is 17 nm with the absorption maximum at 649 nm and emission maximum at 666 nm [154]. The supplier of Dyomics 678 shared the parameters for this particular dye. The dye possesses a mass of 1124.14 Da, a molar absorbance of $1.5 \cdot 10^5$ $\mathrm{M^{-1}cm^{-1}}$, $CF_{280} = 0.135$ and $CF_{260} = 0.215$. The absorption maximum is at 674 nm and the emission maximum is at 694 nm

for Dyomics 678. Alexa Fluor 700 possesses a quantum yield of $\Phi = 0.25$, a life time of $\tau = 1.01 \cdot 10^{-9}$ s and an extinction coefficient at the maximum of the absorbance of $2.9 \cdot 10^5$ $M^{-1}cm^{-1}$. The maximum of absorption is at 702 nm and the maximum of emission is at 723 nm.

4.1.4.1. Fluorophores coupling to antibodies

A vast variety of fluorophores is available as NHS-Esther conjugates. The dye Dyomics 678 was only available as a NHS-Esther conjugate, and needed to be coupled to unlabeled anti-mouse/anti-rabbit antibodies mentioned in table 4.1. NHS-Esther readily react with amino groups of proteins. The optimum pH range for NHS-Esther coupling is pH 8.0 – 9.0. At this pH amino groups of proteins, i.e. the ε-amino groups of lysines are to a high degree unprotonated and highly reactive towards dye-NHS-Esther.

1. 1 mg of antibody was dissolved in 500 µl 50 mM $NaCOH_3$ Labeling-Buffer at 8.1 pH (see table 4.3 on page 45).

2. to obtain a degree of labeling (DOL) for Dyomics 678 of about 2 add a 2.5 molar excess of reactive dye in DMSO to the protein solution.

3. Incubate the reaction mixture protected from light for 1 h on a turning wheel at room temperature.

4. Since a part of the applied dye NHS-Esther will hydrolyze during the labeling reaction, this must be removed from the protein conjugate by using a NAP-5 column (GE Healthcare)

   a) preequilibrate the column with about 5ml PBS three times

   b) put in the reacted mixture (top of to 500 µl of total volume if necessary)

   c) elute the dye-protein conjugate using 1ml PBS in Steps of 200µl and capture it in individual tubes

   d) the second and third tube will show a slightly colored solution and can be used for staining. The protein concentration and DOL has to be measured, see section 4.1.4.2

5. To prevent denaturation of the conjugate after elution, bovine serum albumin (BSA) or another stabilizer may be added

4.1.4.2. Degree of labeling (DOL)

To get the degree of labeling of the used antibodies, an absorption spectrum from 260 nm up to the absorption maximum of the used fluorophore, taken from every eluted solution is needed for this analysis. The concentration of the conjugate and the DOL can be derived by the following equations:

$$c = \frac{[A_{280} - (A_{max,dye} \cdot CF_{280})]}{\varepsilon_{dye}} \tag{4.1}$$

$$DOL = \frac{A_{max,dye}}{c \cdot \varepsilon_{max}} \tag{4.2}$$

where c is the concentration of fluorophore-protein conjugate, A_{280} the absorption at 280 nm of the dye, $A_{max,dye}$ the absorption at the dyes absorption maximum, CF_{280} the correction factor for the dye at 280 nm, ε_{dye} the extinction coefficient of the Protein (e.g. IgG: $\varepsilon_{dye} = 203000$) and ε_{max} the extinction coefficient of the dye and DOL is the degree of labeling (mean number of dyes per protein).

4.1.5. Buffers, media and solutions

All used buffers, media and solutions are listed in table 4.3.

Name	Composition
Cell culture medium (3T3)	DMEM (Dulbecco's modified Eagle's medium) 4.5 g/l glucose from Gibco, 10 % (v/v) heat inactivated fetal calf serum (FCS), Antibiotics (50 units/ml Penicillin, 50 µg/ml Streptomycin)
Cell culture medium (BS-C-1)	DMEM (Dulbecco's modified Eagle's medium) 4.5 g/l glucose from Gibco, 10 % (v/v) heat inactivated fetal calf serum (FCS) and 10 mM HEPES.
10x PBS	1.37 M NaCl, 27 mM KCl, 43 mM Na_2HPO_4, 14 mM NaH_2PO_4, pH 7.4
Goat serum dilution buffer (GSDB)	10 % (v/v) goat serum, 20 mM sodium phosphate buffer pH 7.4, 100 mM NaCl, 0.3 % (v/v) Triton-X-100
Permeabilization-Buffer	phosphate buffered saline (PBS) with 0.05% Triton-X
Labeling-buffer ("NACHO3")	50 mM $NaCOH_3$ in water at 8.1 pH
single color *d*STORM Buffer	PBS, pH 8, 100 mM MEA, containing oxygen scavenger 0.5 mg ml^{-1}(Sigma), 50 mg ml^{-1}catalase (Roche), 10 % glucose
"old" SD-*d*STORM Buffer	PBS, pH 8, 250 - 500 mM MEA, containing oxygen scavenger 0.5 mg ml^{-1}(Sigma), 50 mg ml^{-1}catalase (Roche), 10 % glucose
actual SD-*d*STORM Buffer	50 mM TRIS, 10 mM NaCl, pH 8, containing oxygen scavenger 0.5 mg ml^{-1}(Sigma), 50 mg ml^{-1}catalase (Roche), 10 % glucose, 420 mM β-mercaptoethanol
D_2O SD-*d*STORM Buffer	50 mM TRIS, 10 mM NaCl, pH 8 in heavy water, containing oxygen scavenger 0.5 mg ml^{-1}(Sigma), 50 mg ml^{-1}catalase (Roche), 10 % glucose in heavy water, 420 mM β-mercaptoethanol

Table 4.3.: Table of used buffers, media and solutions

4.1.6. Staining protocol

GSDB staining

This protocol uses the goat serum dilution buffer (GSDB), permeabilization-buffer and 10x PBS (diluted to 1x PBS) from table 4.3 on the preceding page.

1. Fix cells for 5 min at -20 °C in cold MeOH, add about 800 µl per well of a six-well-plate or use 4 % paraformaldehyde (PFA) for 30 min at room temperature
2. wash cells three times with PBS
3. permeabilize cells for 5 min with permeabilization-buffer
4. wash cells three times with PBS
5. incubate cover slips with cells for 1 h upside down on a 100 µl droplet of GSDB on a Parafilm covered glass surface in a dark enclosure
6. in the meantime: dilute antibodies into GSDB and centrifuge for 5 min at room temperature, top speed
7. incubation with primary antibodies at room temperature for 1 h upside down on a 100 µl droplet of antibody solution on a Parafilm covered glass surface in a dark enclosure.
8. wash three times for 5 min in PBS, dilute secondary antibodies into GSDB and centrifuge for 5 min at room temperature, top speed
9. incubation with secondary antibodies at room temperature for 1 h upside down on a 100 µl droplet of antibody solution on a Parafilm covered glass surface in a dark enclosure.
10. wash three times for 5 min in PBS

After this, the cover slip is ready for mounting.

4.2. Devices and equipment

All used devices and equipment, which were used for building the setup and preparing the samples, are listed in table 4.4 on the next page. Everything used in the custom-build setup is described in section 5.1 on page 51.

Device	Company
Autoclave Systec model V-65	Systec, Wettenberg
Centrifuge Eppendorf 5417-R	Eppendorf, Hamburg
Incubator Heaerus for tissue culture	ThermoElectron, Langenselbold
pH meter SevenEasy electrode	Mettler-Toledo, Gießen
Plasma-System ZEPTO	Diener electronic GmbH + Co. KG, Ebhausen
PM100A Laser Power Meter	ThorLabs Inc., USA
S130C Laser Power Sensor	ThorLabs Inc., USA
S121C Laser Power Sensor	ThorLabs Inc., USA
Tempereatur-Feuchte-Datenlogger TFD 128	ELV, Leer
Various DELL Workstations and Server	DELL, USA
Water purification Milli-Q Ultrapure Water Purification System	Millipore, Schwalbach

Table 4.4.: Table of devices and equipment

4.3. Microscopy

4.3.1. Cover slip preparation

To reduce fluorescence background on the used cover slips and to prepare them for coating with poly-L-lysine (PLL), the cover slips were acid washed. At first they were put in ceramic racks and then washed in different reagents, within covered glass containers. Washing steps are as follows:

1. 1M HCl (1 h at RT)
2. wash three times with ddH_2O
3. 100% acetone(1 h at RT)
4. wash three times with ddH_2O
5. 70% ethanol (absolute) (1 h at RT)
6. 100% ethanol (absolute) (1 h at RT)
7. dry in oven at 100 °C for 1 h

Afterwards, the cover slips were put in sterile dishes and sealed with Parafilm. When used for BS-C1 cells or 3T3 cells, the cover slips were used as described. Some applications, like membrane sheeting, or some cell lines, like PC12 cells, also require a poly-L-lysine (PLL) coating of the cover slips. Before the coating with PLL, the cover slips were surface-functionalized in a plasma oven for ten minutes. After the low-pressure, plasma environment of the oven, the cover slips were immediately distributed into six-well-plates and 500 µl of 0.1 mg/ml PLL in MilliQ-Water (sterile filtrated) was applied to the surface as a droplet on each cover slip. The surface-functionalization of the glass provided an evenly spread of the PLL solution. This was incubated at least 30 minutes. Afterwards, the droplet was carefully removed and the coverslip was washed once in sterile MilliQ-Water. The six-well-plates containing the cover slips were kept in the sterile workbench for as long as the excess water had vaporized. Only dry coverslips were used to let cells in solution adhere to them.

4.3.2. Fluorescent bead immobilization on cover slips

To calibrate the three dimensional axial scale of the setup, fluorescent beads (TetraSpec, Life Technologies) were immobilized on coverslip, prepared as described in section 4.3.1 on the previous page. The immobilization was achieved by applying poly-L-lysine (PLL) to the beads and the cover slips. 0.5µl of the TetraSpec-Beads stock solution was added to 50 µl of 0.1 mg/ml PLL in MilliQ-Water, mixed well and applied to a dry cover slip for five minutes. After five minutes the cover slip was washed once with PBS and then immediately mounted in the same solution used for 3D SD-*d*STORM imaging.

TetraSpec-Beads could also be applied directly to a sample using the same method. An already stained, washed and not dried coverslip with cells on it was kept in a dry well of a six-well-plate and 50 µl of the solution described above containing the TetraSpec-Beads was added. After five minutes it was washed once in PBS and immediately mounted in the imaging buffer.

4.4. Software

Several different programs were used to analyze and present the data of this thesis. The Software, which was developed during the project is also listed here, but is discussed in great detail in chapter 5 on page 51. The software controlling the acoustic-optical tunable filter (AOTF) was written by Ricardo Henriques [122] and was altered to fit the parameters of the setup. A listing of the software with all modification is shown in appendix C on page 151.

Software Name	Company or URL	Usage
UCSF Chimera [38]	http://www.cgl.ucsf.edu/chimera/	prototyping 3D representation
Fiji [67]	http://fiji.sc/Fiji	ImageJ-based image processing package
FreeCommander 64bit	http://freecommander.com/	raw data management
GIMP 2.8	http://www.gimp.org/	assembling Figures
GNU Octave	https://www.gnu.org/software/octave/	tests of SD-*d*STORM algorithm
GNUplot	http://www.gnuplot.info/	fitting and statistics
JabRef 2.9	http://jabref.sourceforge.net/	literature management
Laser Control [122]	https://code.google.com/p/quickpalm/	controlling the 405 nm Laser
Lyx 2.0.6	http://www.lyx.org/	writing the thesis
MatLab	MathWorks GmbH, Ismaning	early tests of SD-*d*STORM algorithm
µManager [9]	https://www.micro-manager.org/	controlling the microscope
Notepad++	https://notepad-plus-plus.org/	textfile data readout
rapi*d*STORM 3.1.1 [134]	http://www.super-resolution.biozentrum.uni-wuerzburg.de/research_topics/rapidstorm/	finding localization in raw data
SDmixer [138]	see appendix A on page 149	pair-finding and reconstruction
Origin 8.5 PRO	OriginLab Corp., USA	graphs, fitting and statistics
Python 2.7	https://www.python.org/	drift correction, prototyping
Ubuntu 10.04.4 LTS	http://www.ubuntu.com/	OS of Software development PC
TFD-128 Software v1.02	ELV, Leer	temperature data readout
total Commander 64bit	http://www.ghisler.com/	raw data management
Windows 7	Microsoft, USA	microscope control/analysis
Windows XP	Microsoft, USA	microscope control

Table 4.5.: Table of used software

5. Results

5.1. The SD-*d*STORM Setup

5.1.1. Layout of the microscope

The used setup was custom-build. Starting with an initial set of equipment, the setup was based on the one described by Henriques et al. [122]. Essentially the setup consisted of a wide-field microscope with a custom laser combining section and a custom telescope to couple the laser beam into the microscope. This telescope could be adjusted to focus everywhere on the back focal plane (BFP) of the objective and thus could be operated in normal wide-field and TIRFM mode [6, 11, 95]. Differences, changes and the rework of the laser combiner will be discussed in the following.

The optical devices were assembled on a CleanTop Optical Table (TMC vibration control) and the control devices and computers were housed in a customized 19 inch server-cabinet (HP, USA). The microscope was a customized Nikon Ti Eclipse (Nikon, Japan), possessing two filter turrets. For all measurements a high numerical objective (Apo 100x 1.49 NA, Nikon, Japan) was used. The microscope was also equipped with an auto-focus (Perfect Focus II, Nikon, Japan), keeping the used objective at level during measurements. The setup was divided into two "arms", the acquisition side and the excitation side. The latter consisted of several light sources. Although only three were used, the whole setup will be described in the following. The aim of this work was also to build a multipurpose setup, as versatile as possible. An option is given to choose between illumination with a fluorescent lamp (Intensilight, Nikon), providing a continuous spectrum, and excitation with laser light. The available lasers are listed in table 5.1 on the following page.

A schematic of the laser setup is shown in figure 5.1 on page 53. The lasers of the 405 nm, 488 nm and 568 nm were aligned parallel to each other. A beam expander (2x Quioptiq) was mounted in front of the 488 nm and the 568 nm laser. The 568 nm beamline was facing a 45° angled mirror to cross the path of the light originating from the other two lasers. In the crossing point of the beams, dichroic mirrors were placed to overlay the beams, at first to combine the 488 nm and 568 nm beams using "LaserMUX 503

Name	Wavelength [nm]	Peak Power [mW]	Beam Diameter [mm]
Quioptiq 405	405	80	2.5
Coherent sapphire 488 LP	488	150	1.5
Coherent Sapphire 568 LP	568	150	1.5
Toptica iBeam Smart 640	643	150	1
Toptica iBeam smart 660	661	130	1

Table 5.1.: Lasers of the laser combiner part of the setup

edge" and then using "LaserMUX 427 edge" to add the 405 nm beam. Two mirrors were used to reflect the combined beam into an acoustic-optical tunable filter (AOTFmC-400.650-TN, AA Optoelectronics). The latter was controlled using open source software (QuickPALM, Laser Control Software [122]), internally adapted to the specifics of our Lasers (appendix C on page 151). In the off state of the AOTF the beam was guided into a beam-dump consisting of a bend copper-pipe to minimize scattered light inside the enclosure around the lasers. When a specific wavelength was switched on by the AOTF, a 45° angled mirror was hit, about 7° to the right of the beam dump. A second angled mirror was used to reflect the light onto a dichroic mirror (zt 561 RDC) which overlays all beams from the ON-angle of the AOTF with the beam from the 643 nm or the 661 nm laser. These red lasers were located 90° turned from the other beam path, since the used dichroic only reflected below 570 nm. Selection between 643 nm and 661 nm beams was done by a flap-mirror, which would block the 643 nm beam and reflect the 661 nm when positioned upright and would simply pass 643 nm beam, while 661 nm is not reflected to the combining dichroic mirror, when the flap-mirror is in the downside position.

The rather long light path behind the AOTF to the last dichroic mirror was constructed for calibration, since a perfect overlay of three beams is easier achieved when small angular differences show a bigger deviation from the optical axis. Calibration was done using two or more iris apertures positioned at the exact same height and reduced beam intensities with neutral density filters (1 - 4 OD, ThorLabs Inc., USA). The described part is further referred to as the laser combiner.

The combined beam from the laser combiner was reflected via a periscope onto the level of the entry port of the research microscope, and aligned into the EPI-TIRF illuminator by three mirrors. The introduction of these mirrors allowed a fine alignment without the need to manipulate the laser combiner. The EPI-TIRF illuminator consisted of a beam expander (factor 10) composed of two lenses (L1 = 10 mm, L2 = 100 mm) and a

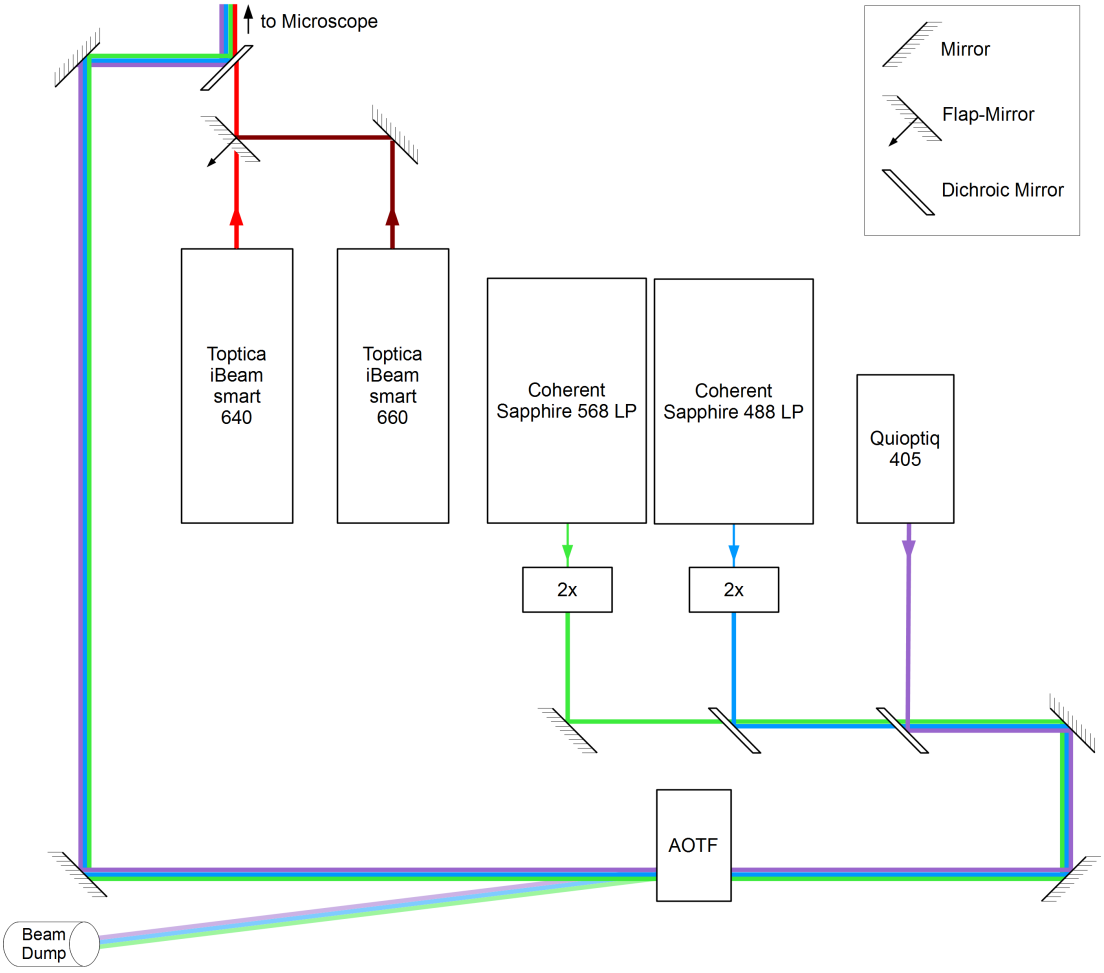

Figure 5.1.: Schematics of the laser combiner

focus lens (L3 = 500 mm) to focus the beam on the back focal plane (BFP) of the high numerical aperture objective. L2 was installed on separately adjustable x/y translation stages, while L3 was mounted on x/y/z translational stages. This was done to fine adjust the focus on the BFP and to move the beam laterally in the BFP to reach EPI or TIRF conditions. The laser beams were reflected into the objective via the upper turret of the microscope. For experiments presented in this thesis, a filter cube of this turret was only equipped with a dichroic mirror. The used dichroics for all experiments shown in this work are listed in table 5.3.

Name	suited laser lines [nm]	emission windows [nm]
Semrock Di01-R405/488/561/635	405, 488, 568, 643	425-465, 500-550, 575-620, 655-805
HC DL No 497/661	488, 643	495-635, 655- >800

Table 5.2.: Dichroic mirrors used to reflect laser light on the back focal plane of the objective

The sample was mounted on a x/y motorized stage and a Nano-Scan-Z (Pro Scan III XYZ, Prior), both computer controlled. Furthermore, an enclosure from OkoLabs was installed around the microscope and temperature controlled at a steady 24 °C ± 0.2 °C. The temperature control was essential for acquisition of 3D data (see section 5.3.2 on page 78). The interior of the enclosure could be illuminated by LED-bands (Conrad Elektronik) that were fixed on the ceiling of said enclosure. Switchable power supplies were custom-build using parts from Conrad Elektronik.

Emission light was passing through a dichroic mirror (table 5.2) underneath the objective and is magnified by an internal 1.5x lens of the microscope. When performing 3D SD-*d*STORM data acquisition, a cylindrical lens (Melles Griot, custom part, f = 10 m) was introduced underneath the turrets, housing the filter cubes and dichroic mirrors. The left camera-port of the microscope was equipped with a ten-slot filter wheel from Prior and also controlled by the Pro Scan III XYZ. For all experiments described here, an empty position of the filter wheel was used, or a position with the long pass filter BLP01-635R. The filter wheel could also be used as a C-mount enabling the attachment of a camera directly to the port at the end of the filter wheel. At this position an OptoSplit II (Cairn Research, UK) was mounted to split the image of the microscope spectrally into two images side by side on the same EMCCD camera chip. A schematic of the OptoSplit II is shown in figure 5.2 on the next page. The design of this device is loosely based on technology described by Kinosita et al. [81], but includes additional functions, like

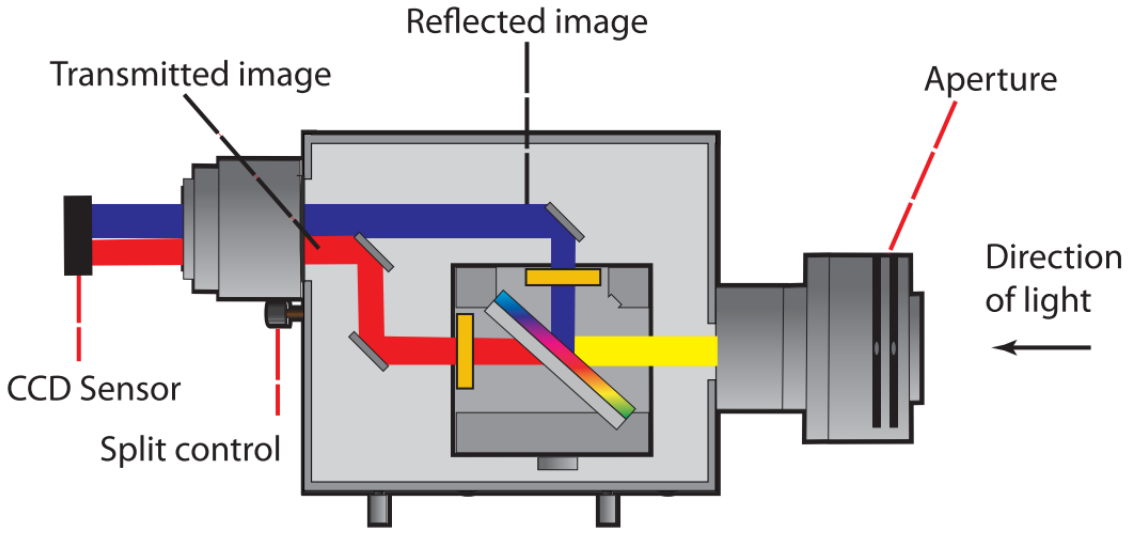

Figure 5.2.: Schematic of the OptoSplit II, modified from Cairn Research

internal Name	dichroic mirror	transmission channel	reflection channel
3D SD-*d*STORM	690 DCXR	none	none
first SD-*d*STORM	710 DCXR	HC 687/40	ET 794/160

Table 5.3.: Filters and dichroic mirrors used in the OptoSplit II Filter Cubes. The 3D SD-*d*STORM case employs a BLP01-635R in front of the OptoSplit II to block the laser wavelength. [85, 86]

- rotating mirror cradle to give precise symmetrical control of the degree of separation whilst maintaining identical path length
- half-size fully silvered mirror at the output for recombining the images
- fine adjustment controls for camera focus and vertical alignment

As seen in figure 5.2 a rectangular aperture was placed at the position where the chip of the camera would be to obtain a defined region of interest. The OptoSplit II features own filter cubes with positions for a dichroic mirror and filter-fittings for each image projected onto the camera at the end of the device. Two different combinations were used as listed in table 5.3. The 3D SD-*d*STORM uses a BLP01-635R in front of the OptoSplit II to block the excitation laser and was fitted for the Alexa Fluor 647/Dyomics 678 pair, while the first SD-*d*STORM was optimized for the Alexa Fluor647/Alexa Fluor 700 pair from [85].

The images were acquired by a computer-controlled Andor EMCCD DU-897E with 512 x 512 pixels with a pixel size of 16 µm. As long as not differently noted, the em-gain of the camera was set to 60 and was running in frame-transfer mode. The PC used for controlling and acquiring data was a DELL T3500 with a Quad-Core CPU and 12 GB RAM, running Windows7 64bit. Most of the components were controlled by µmanager [9]. Toptica lasers of 643 nm and 661 nm wavelength were controlled by Hyper Terminal adapted from Windows XP to Windows7 and the AOTF was controlled by a software written by Ricardo Henriques [122] and adapted for our laser lines. The program code of the python script with the marked changes can be found in appendix C on page 151.

5.1.2. Sample drift

The position of the sample in x, y and z was not steady over time, due to turbulent air from the temperature stabilized OkoLabs enclosure, hypothetically caused by laser illumination produced heat and oscillation from the outside not damped by the optical table. To correct for this drift in each set of acquired image series we used a custom-written Python 2.7 based program that identifies fluorescent TetraSpec beads as fiduciary markers within the sample. This was done after the image series were analyzed by rapi*d*STORM 3.1.1 [134]. The output files of rapi*d*STORM 3.1.1 were text files with the quantities of position in x, y and optional z, the frame number and intensities, beside other quantities for every found localizations. Beads can be recognized as very bright localizations, remaining over hundreds of consecutive frames with a small deviation from frame to frame in position. The decision whether a localization is a fiduciary marker was made by several parameters: an intensity threshold, with usually $>$10000 ADC, the minimum number of appearances, usually 1000 frames, the maximum allowed localization precision, usually $<$8 nm and the maximum deviation of the fiduciary marker within a window of ten frames, usually $<$20 nm. The position of the beads were tracked and the entire image series was corrected for the combined track of every bead by a matrix operation. The accuracy of this was calculated from the standard deviation σ of the distances of the corrected bead localizations. Typically, we achieved drift correction accuracies of 5 nm in the two-dimensional case and about 10 nm in the three-dimensional case. Drift correction in 3D comprised the tracking of the fiduciary markers in all three dimensions, but allowed correction for drift in x and y directions only. This was done because the setup was running a reliable steady auto-focus system, but tracking of the beads also in z was necessary as localizations from fluorophores could have appeared above and underneath a bead and could have led to false shift in x and y position when the z component of the coordinate set would have been ignored.

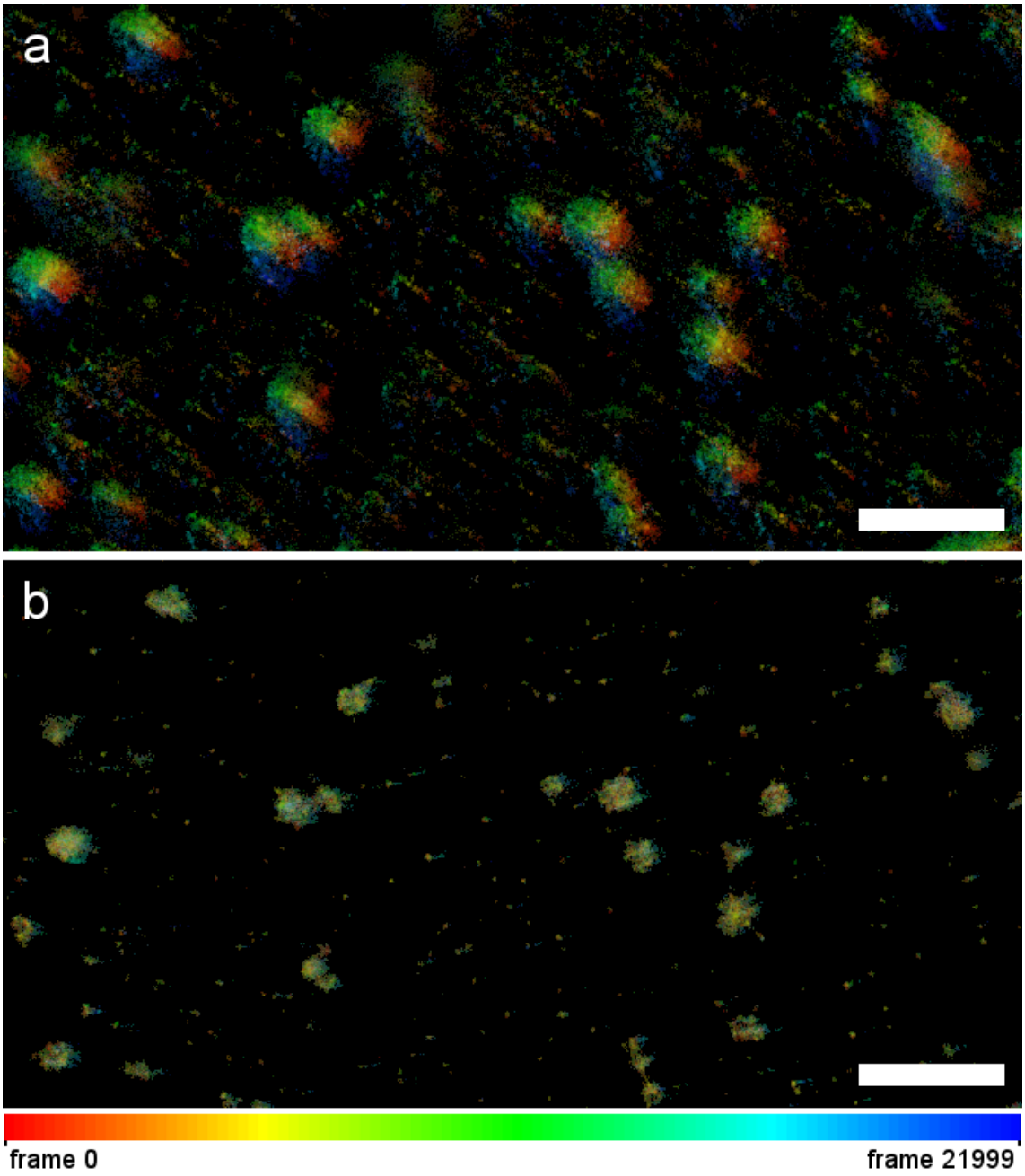

Figure 5.3.: Sample drift and correction. Both panels show the super-resolved field of view of figure 5.8 on page 67, panel c, color coded with frame number. The color scale bar at the bottom shows the development over time and begins with frame 0 at the left, red end and runs to frame 21999 at the right, blue end. a) before drift correction, b) after drift correction. White scale bars in a) and b) are 1 µm

The program was written and developed by Gregor Lichter and is described in detail in [89]. It was running on a separate DELL workstation featuring two Six-Core CPUs, 48 GB RAM, running Windows 7, 64 bit or Ubuntu 10.04.4 LTE. This was necessary due to the high computational power demands of the drift correction, especially in the 3D case.

Figure 5.3 on the previous page shows a super-resolved image, without and with drift correction. The drift shown here is a good representation of how the setup behaves normally. The reconstruction of the non-drift-corrected data set seems to display extensive drift, but given the dimensions of the images, the localizations never deviate more than about 150 nm from the reconstruction of the drift corrected data set. In a standard fluorescence microscope this would hardly be visible as the size of the depicted structures is below the diffraction limit. The images show the development over time coded by color, with red and blue representing the start (frame 0) and the end of the measurement (frame 21999), respectively.

5.2. Multicolor *d*STORM by spectral demixing

When using a SMLM approach, in contrast to standard fluorescence microscopy, many images of individual fluorophores are taken to reconstruct the image after acquisition point by point. Doing this with more than one color imposes some challenges, as discussed in sections 3.4.1 and 3.5. This thesis describes a spectral demixing approach to achieve multicolor *d*STORM using simultaneously excited and spectrally overlapping fluorophores. The basic principle was published in [85], using Alexa Fluor 647 and Alexa Fluor 700 as fluorophores, and later discussed in more detail and extended to 3D with Alexa Fluor 647 and Dyomics 678 in [86].

5.2.1. Spectral demixing and pair-finding

Amongst the currently available organic fluorophores, Alexa Fluor 647 and other carbocyanine dyes are most efficient for single molecule localization [100, 97, 57]. This is based on their photostability, brightness with up to 6000 photons per ON cycle, and their ability to exhibit a prolonged OFF state in an oxygen-free, reducing buffer. Two pairs of carbocyanines were found to show sufficient blinking for SMLM in the same buffer. For the pair Alexa Fluor 647 and Alexa Fluor 700 a buffer containing 100 mM to 300 mM β-mercaptoethylamine (MEA) was found to work best [85]. The pair Alexa Fluor 647 and Dyomics 678 needed a buffer containing 420 mM β-mercaptoethanol (β-ME) and was prepared using D_2O for a higher quantum yield [86] (section 5.2.2 and table 4.3).

To distinguish between overlapping emission spectra of two fluorophores, a dual-channel emission splitter was employed to project two images side-by-side onto one camera, one in the shorter wavelength range and one in the longer wavelength range of the emission spectrum of the fluorophores (similar to [24, 144, 13]). The filters and the dichroic mirrors were matched to block efficiently the 643 nm laser line for simultaneous excitation of both fluorophores and to block the 405 nm laser, which was used for adjusting blinking rates. Selection of the dichroic mirror and filters were also done with respect to the cross-bleed between the short- and the long-wavelength-channel required for spectral demixing (see section 5.1 on page 51 for precise parameters). This was expected to result in one localization in the short-wavelength-channel and one localization in the long-wavelength-channel for every fluorescent signal of every fluorophore used. A representation of the emission spectra of Alexa Fluor 647 and Dyomics 678 is shown with the used dichroic mirror and an example of the field of view of the camera (figure 5.4a, page 60).

Our algorithm was searching for paired localizations in output-files of rapi*d*STORM 3.3.1 [134]. The distance between the detection channels (offset in x, y and z), pixel-size and fluorophore characteristics were given as parameters. In one channel every localization was treated as an origin of a vector with the length of the distance between the two channels. At the end of this vector was a search area with variable radius, usually 156.5 nm, which equals 1.5 px in the raw data sets (figure 5.4c). Since this rather small margin is very important for finding pairs, the right offset between channels had to be precise. Therefore we introduced an offset optimization functionality, using a subset of the localization with several tiny shifts (typical 21 nm) in every direction. The final offset was determined by finding the absolute maximum in this 2D matrix (section 5.2.4). When a single localization was found within the search radius at the end of the offset vector, the originating localization and the found one were considered as paired and moved from the list of localizations to the list of pairs. If more than one localizations were found, the results were not transferred to the list of pairs but discarded. This was done as localizations with more than one candidate for pairing could have led to a false color assignment, especially when the intensities of those two or more found localizations differ significantly from each other. One could argue that such a set of more than two localizations, where the candidates for pairing only differ in a small margin in the intensity, do not have to be removed as a false color assignment would rather be unlikely. But since the number of those multi-candidate pairs was in the order of 0.01%, this "smart pair-sorting" was never implemented in the algorithm and will be discussed in section 7.1.1.

From the list of localizations a plot was created with localization intensities of the short-

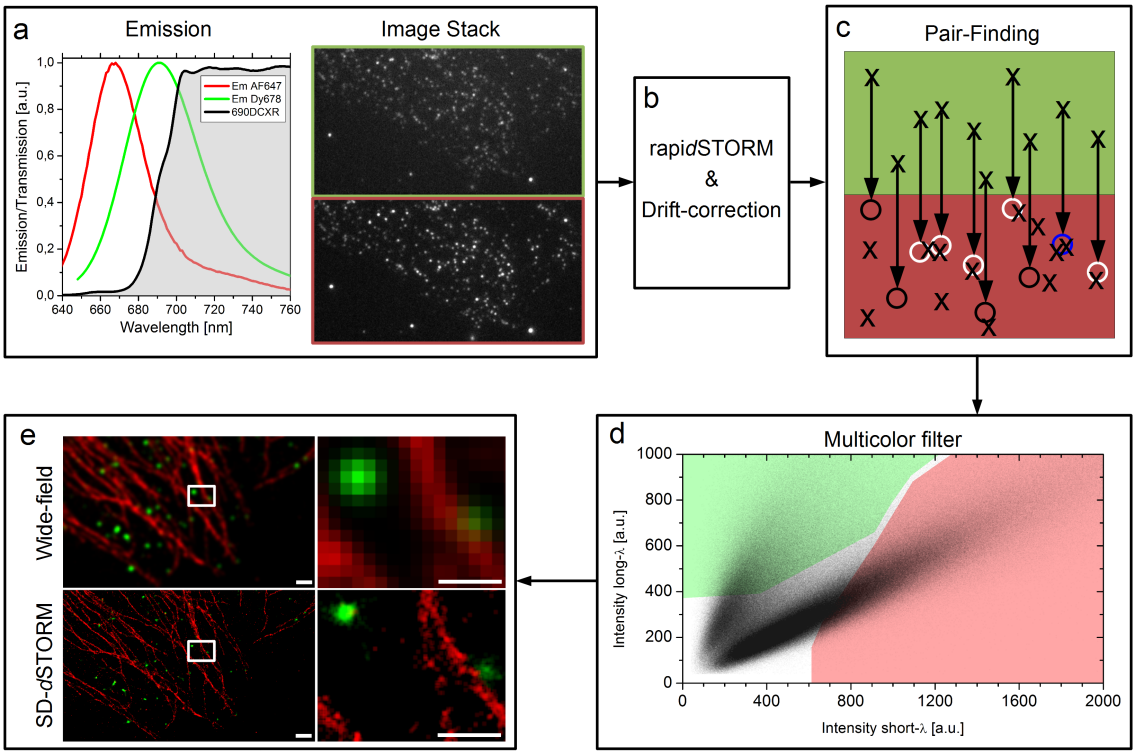

Figure 5.4.: Workflow of multicolor SD-*d*STORM. (a) Left: emission spectra of AF647 (red) and DY678 (green) and transmission spectra of the dichroic emission splitter (690DCXR, black, gray area). Right: single frame of image stack of both short (red frame) and long (green frame) wavelength sides of the split emission view showing single molecule signals from NIH 3T3 cells immunostained for microtubules (AF647) and clathrin heavy chain (Dy678). (b) rapi*d*STORM is used to localize single molecules in the whole image stack from (a) and the resulting localizations are corrected for sample drift. (c) Illustration of the pair-finding algorithm: the black 'x' indicates localizations, the black arrows indicate the offset vector and the circles indicate the search area at end of the offset vector. The numbers of identified localizations within the search areas (circles) are indicated by the color of the circles: white = precisely one, black = none, blue > one. (d) 2D intensity histogram of short and long wavelength sides from the sample described in (a). The custom color filter mask (white area) excludes localization pairs while the pale red and green areas assign specific colors to the localization pairs. (e) Rendered wide-field and reconstructed SD-*d*STORM image of the sample described above. Scale bars: 1 µm (large view, left), 500 nm (sub-region, right). [86]

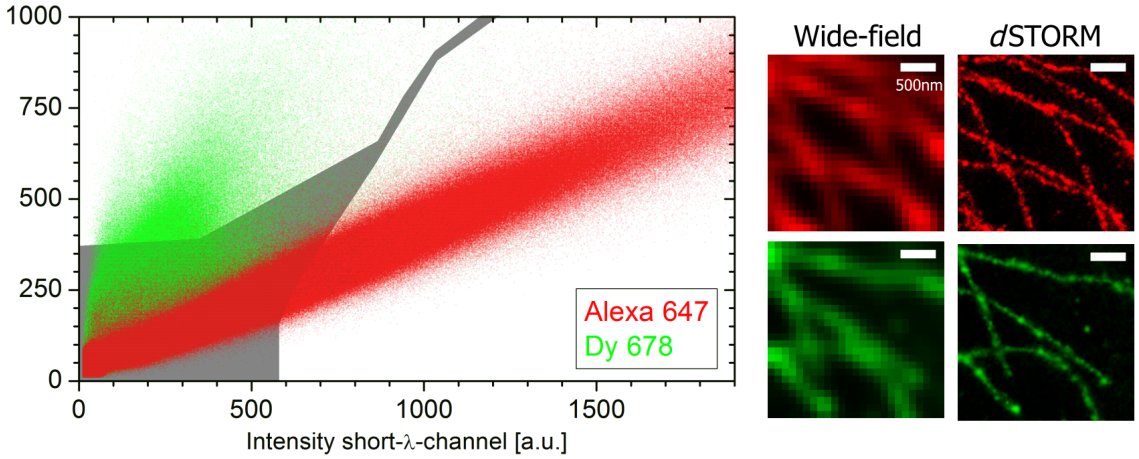

Figure 5.5.: Custom design of color filters to minimize crosstalk. NIH 3T3 cells were immunostained separately for microtubles with Alexa Fluor 647 and Dyomics 678 and imaged using SD-*d*STORM. After pair-finding the intensities measured in short and long wavelength sides of the emission splitter for each localization pair were plotted into a two-dimensional intensity histogram. Custom color filter masks (white areas) are designed to assign specific colors to each pair, while the gray area excludes localization pairs. The filters are tuned to minimize color crosstalk to less than 1 % as the sum of crosstalk from the Alexa Fluor 647 and the Dyomics 678 area, and vice versa. Examples of wide-field and *d*STORM reconstructions of the single color experiments are shown on the right. Scale bars are 500 nm. Modified from [85].

wavelength-channel displayed on one axis and from the long-wavelength-channel on the other axis. Fluorophores show distinct populations in this plot, dependent on the used dichroic mirror in the OptoSplit II. When areas are provided where only localization-pairs of one fluorophore population is located, the software can assign color to localization-pairs based on those provided areas. To optimize color separation, two single color experiments were performed with each fluorophore separately. The intensities from the short- and long-wavelength-channel of the single color localization pairs were plotted together in differently assigned colors in a two-dimensional histogram. Those two different populations of localization pairs from the two different fluorophores were used as a template to generate the filters to assign a "fluorophore-identity", meaning a color to a certain area within this two-dimensional histogram. Such a two-dimensional intensity histogram is shown in figure 5.5.

After fine-tuning the filter masks, the sum of all the false color assigned localizations pairs were minimized. This false assignment is also referred to as "crosstalk". It should be

Filter stringency	Crosstalk short to long	Crosstalk long to short	Crosstalk total	Loss of localizations short	Loss of localizations long	Loss of localizations total
normal	0.50 %	1.1 %	1.60 %	-	-	-
medium	0.10 %	0.9 %	1.00 %	2.0 %	7.1 %	9.1 %
high	0.05 %	0.7 %	0.75 %	4.4 %	17.0 %	21.4 %
very high	0.03 %	0.5 %	0.50 %	8.4 %	33.0 %	41.4 %

Table 5.4.: Percentage of crosstalk between short-wavelength fluorophore Alexa Fluor 647 (short) and long-wavelength fluorophore Alexa Fluor 700 (long) was calculated from the number of localizations occurring in the other fluorophore assignment-area (filter) in the two dimensional histogram. The normal filters were taken as a baseline and other, more stringent filters were compared to this, varying mostly in the size of the area in which a localization pair would be assigned to either of the two fluorophores. The loss of localizations in each case is indicated as the percentage of the localizations obtained using the normal filter (100 %) [85].

noted that this is the sum of all false assigned localizations from the first dye in the area of the second dye and vice versa. The tuning of the filters was achieved by moving the borders of the fluorophore specific areas consecutively and calculating the crosstalk for each step. In the case of the pair Alexa Fluor 647 and Alexa Fluor 700 crosstalk could be reduced to 1.6 % maintaining enough localization for a trustworthy reconstruction [85] and for the dye pair Alexa Fluor 647 and Dyomics 678 crosstalk below 1 % was achieved [86]. For the pair Alexa Fluor 647 and Alexa Fluor 700 different filters with increasing stringency were tested and crosstalk and loss of localizations were calculated, shown in table 5.4.

Pairs not located in an area with an assignment to a certain fluorophore were neglected. It should be noted that those filters are not linear and also not emerging from the origin of the two-dimensional histogram (figure 5.4d). From the list of localization-pairs with assigned colors, two TIFF images (stacks in the 3D case) were reconstructed using the given parameters, typically with a 10 nm Pixel-size in x and y (25 nm in z)

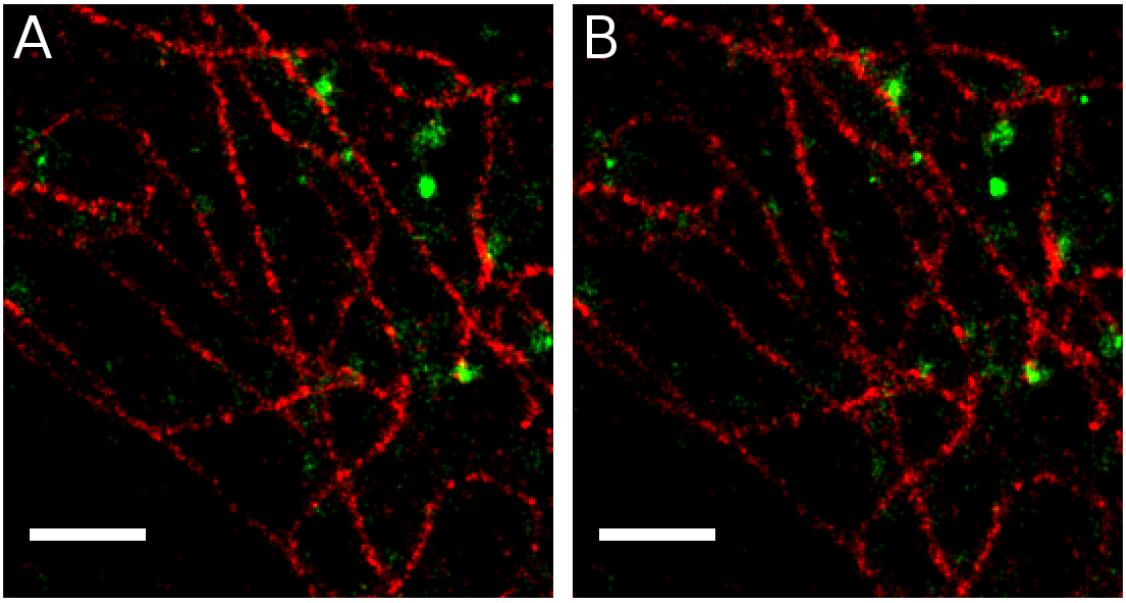

Figure 5.6.: Comparison of SD-*d*STORM reconstruction from short- and long-wavelength-channel with Alexa Fluor 647 (red) and Alexa Fluor 700 (green) in imaging buffer containing water. Reconstruction was done using all paired localizations in the short (A) and the long (B) wavelength-channel. Scale bar 1 µm [85].

and blurred with a Gaussian function with the localization precision of each fluorophore (25 nm/66 nm for Alexa 647, 25 nm/66 nm for Dyomics 678, see section 5.4). The resulting images were of the same size as the images derived by rapi*d*STORM, showing both channels and enabling the direct check for proper reconstruction from both sides (origin-localization in short and origin-localization in long channel) and for compatibility to techniques involving channel-overlay. This advantage was already discussed in [85]. A reconstruction with offset vectors originating from either side is shown in figure 5.6. The image was acquired using the first SD-*d*STORM filter setup (table 5.3) and the old SD-*d*STORM Buffer (table 4.3). Thus, the two resulting images show localizations where they were measured without an error beyond localization precision.

In the course of this project a software was developed to automate the process of pair-finding, filter application to the two-dimensional histogram and image reconstruction, also in 3D. The very early evolution of this software was written in MatLab and was not fully automated then and rather slow in finding localization pairs. As for example, the reconstruction shown in figure 5.6 was acquired with this early version and needed two hours to find the localization pairs and reconstruct each of the images. This early version

did not have the capabilities to handle a 3D dataset. We developed a more elaborate version of the software, which implements all the features presented in this chapter. After testing the first improved version of the code in open GNU Octave (General Public License) and development as a C++ project (Linux command line tool), the software finally was named SDmixer, running on Windows 7, 64 bit or higher, with an easy to use graphical user interface. We published the results [138] and made ready-to-use installers available for download at Source Forge. The source code is also available in an open source manner at GitHub. The links are listed below:

- Installer: http://sourceforge.net/projects/sdmixer/
- Manual: sourceforge.net/projects/sdmixer/files/SDmixer_Manual.pdf
- Source code: https://github.com/gtadeus/sdmixer2

The data structure for a SD-*d*STORM measurement is shown and explained in section 5.5 on page 83. Potential improvements to the spectral demixing approach are discussed in section 7.1.1 on page 99.

5.2.2. The effect of heavy water (D_2O)

It has recently been demonstrated that replacing H_2O with D_2O significantly enhances photon yield due to the reduced absorbance of D_2O [82]. This effect is purely physical in nature and does not influence the photochemical properties of the fluorophores. With near infrared emitting dyes such as Alexa Fluor 647 and Dyomics 678 we observed an increase in photon count of about 5 %, due to less absorbance of the used buffer. This is shown in figure 5.7 on the facing page. The experiment was performed for the following dye and buffer conditions with at least six replicates per condition: Alexa Fluor 647 with and without D_2O in the buffer and Dyomics 678 with and without D_2O in the buffer. The localizations were pooled before statistical analysis. The y axis of figure 5.7 was scaled down for simplicity.

Approximately 5 % overall gain in intensity for localizations of Alexa Fluor 647 and Dyomics 678 could be observed with D_2O in the imaging buffer (figure 5.7). To maximize the photon yield for the dye pair Alexa Fluor 647 and Dyomics 678, imaging buffers for those fluorophores were always prepared with D_2O, if not noted otherwise. Most of the experiments involving the pair Alexa Fluor 647 and Alexa Fluor 700 were finished before the beneficial effects of heavy water in an imaging buffer were known and published. No experiments with the pair Alexa Fluor 647 and Alexa Fluor 700 mentioned in this thesis were performed with an imaging buffer containing D_2O.

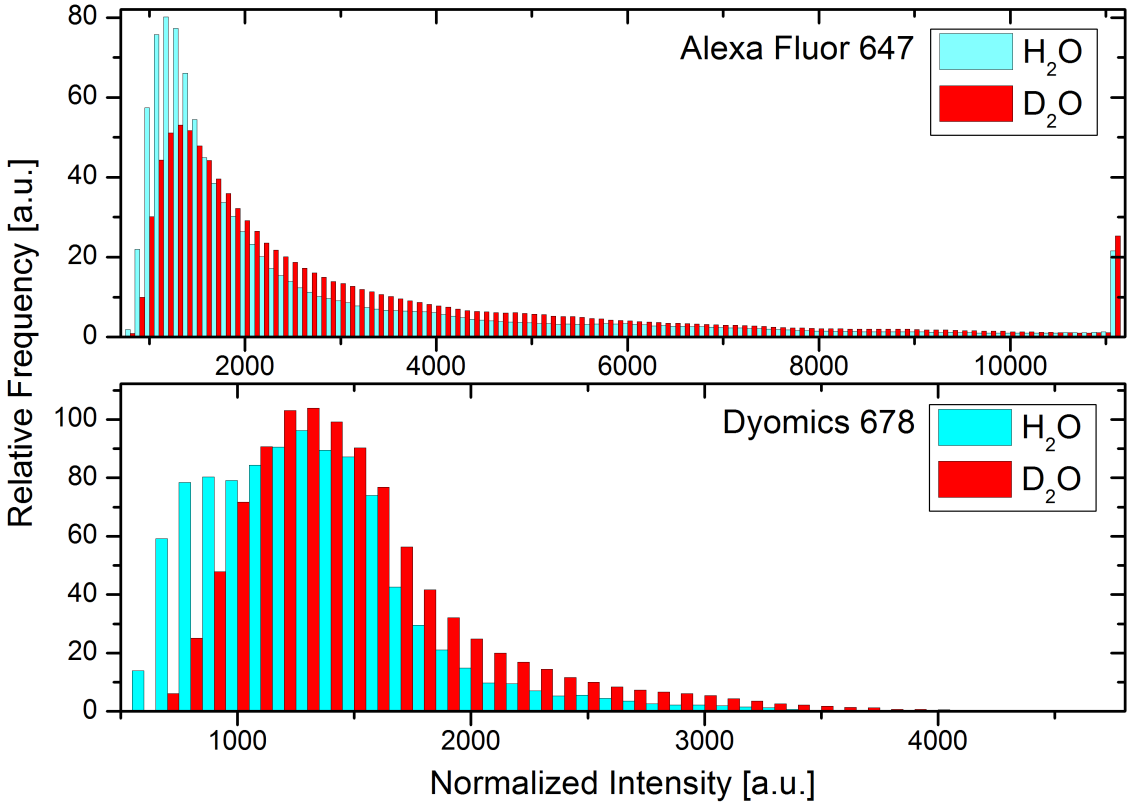

Figure 5.7.: Effects of heavy water on the fluorescence intensity. NIH 3T3 cells were immunostained for microtubles (Alexa Fluor 647 or Dyomics 678) and imaged using *d*STORM. Single molecule intensities of *d*STORM image sequences were measured and plotted in a histogram (bin = 100 a.u.) for Alexa Fluor 647 (top) and Dyomics 678 (bottom). The right-shift of the red (D_2O) population indicates a significant gain approximately 5 %, in intensity [86].

5.2.3. Accuracy of multicolor registration

To test the accuracy of multicolor representation using the pair-finding approach of spectral demixing, immobilized Alexa Fluor 647 labeled secondary antibodies, co-labeled with Dyomics 678 using the NHS-Esther coupling protocol were imaged (section 4.1.4.1). The coupling of additional fluorophores to antibodies already commercially labeled proofed to be rather insufficient, such that only a fraction of all antibodies carrying Alexa Fluor 647 is also showing a signal of Dyomics 678. A large field of view is shown in figure 5.8 with a size of 36 µm by 17.5 µm, demonstrating accurate registration between the two colors over this large area. The different regions of interest (panel 1 to 8) show no deviation from an exact overlay of the two colors. Individual localizations are shown in panel 8', from which panel 8 was reconstructed (see section 5.2 on page 58).

Perfect multicolor registration using spectral demixing is also demonstrated on NIH 3T3 cells immunolabeled for clathrin heavy chain with Alexa Fluor 647 and AP-2 with Dyomics 678 that are both components of the same diffraction limited endocytic structure called clathrin coated pits (figure 5.8b, c). Streaks in panel c could be interpreted as a sign of sample drift. That this is not the case is shown in figure 5.3 on page 57, which is using the same raw data set from which figure 5.8 was derived. The image was acquired using the 3D SD-*d*STORM filter setup (table 5.3) and the D_2O SD-*d*STORM Buffer (table 4.3).

5.2.4. Offset optimization for the pair-finding algorithm

Since the exact offset between the two wavelength-channels of the described setup is crucial for the reconstruction of images, the procedure of "Offset Optimization" was included into the algorithm. This optional procedure searches for a global maximum of pairs in a given offset range by paring up a subset of localizations with small, consecutive shifts of the offset vector in x and y, usually in steps of 21 nm. Nevertheless, a good initial estimate of the offset in x and y is important, since a search with four steps in each direction in a subset of only a tenth of the data will take longer than the actual pair-finding process in the whole dataset. This was also done in the three-dimensional case only in x and y, since the offset in z was directly determined by the 3D calibration procedure described in section 5.3 on page 72.

Figure 5.9 on page 68 shows a large area, in which the offset vector was varied. The used dataset was a 2D image sequence with 10000 frames, acquired from a sample of NIH 3T3 cells, stained for microtubuli with Alexa Fluor 647 and for clathrin heavy chain with Dyomics 678. Every pair-finding process, for all shifts of the offset vector in x and

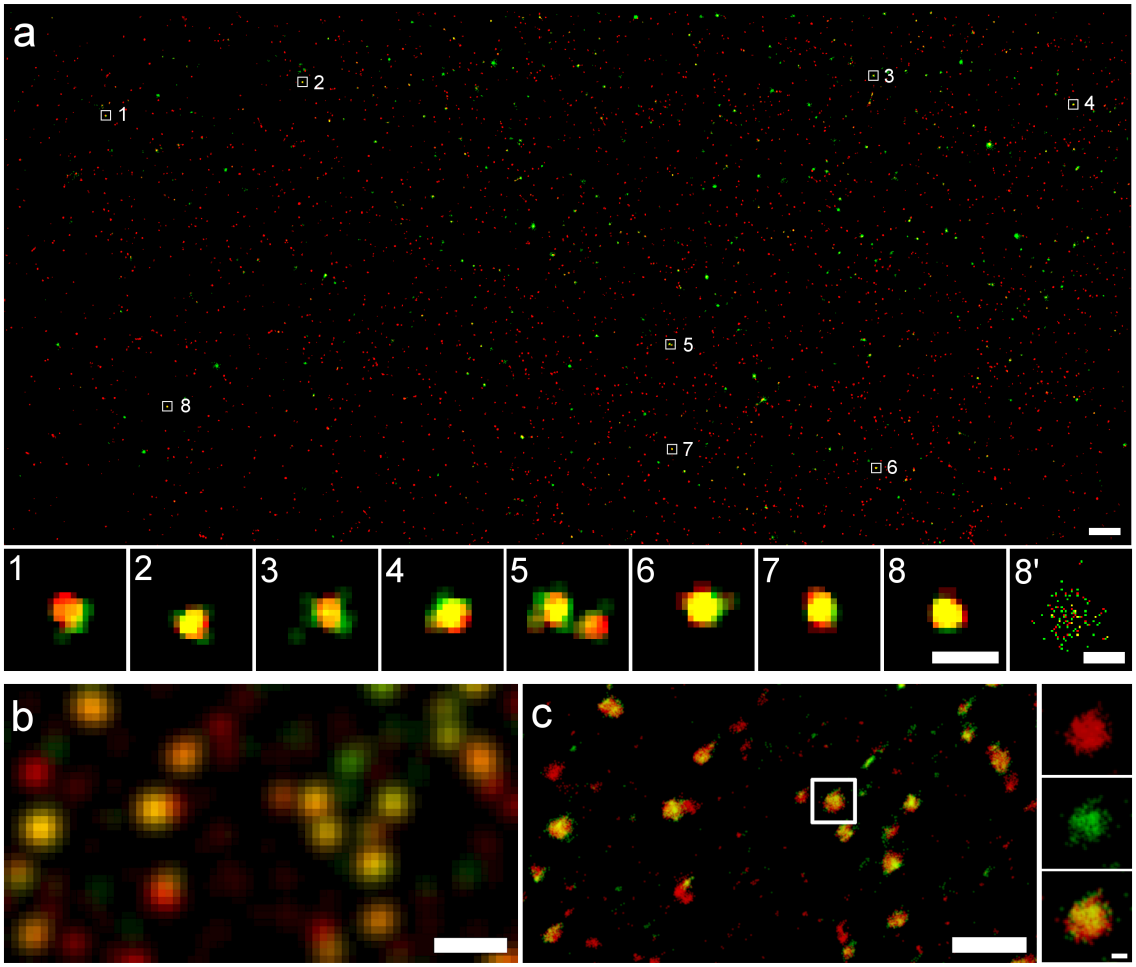

Figure 5.8.: Multicolor registration: (a) Alexa Fluor 647 labeled antibodies were double-labeled with Dyomics 678 and immobilized on a poly-L-lysine coated coverslip and imaged in SD-*d*STORM. The field of view shown is 36 µm × 17.5 µm. The numbered boxes magnified below (1–8) show spots of repeatedly blinking double-labeled antibodies. Image 8´ shows the raw single molecule localization coordinates (single 1 nm pixels) without Gaussian blur. (b), (c) NIH 3T3 cells were immunostained for clathrin heavy chain (AF647) and AP-2 (Dy678) and imaged in (b) wide-field (rendered) and (c) SD-*d*STORM. Scale bars: (a) large view 1 µm, magnified boxes 1–8 100 nm, box 8´ 10 nm. (b), (c) large view 1 µm, magnification 100 nm [86].

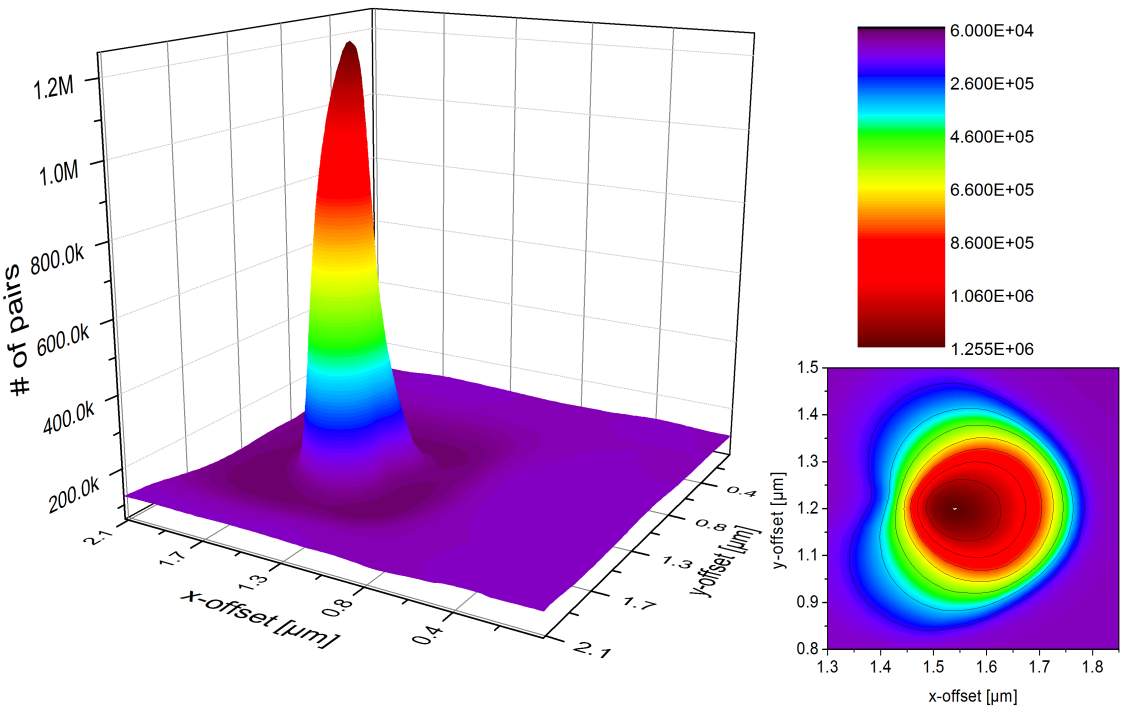

Figure 5.9.: Quantification of the offset optimization. The offset vector was subsequently varied in x and y in a range of 2.1 µm in both direction. The plot shows the number of identified pairs with respect to the offset.

y, was applied on the entire dataset and not only on a subset of the 10000 frames. The figure shows a distinct maximum. This not only shows that a well chosen offset vector is important, but also proofs that the pair-finding approach does not artificially increase any signals or suppresses noise by other means than by paring localizations present on the observed structure. The latter ability is discussed in more detail in section 5.2.5.

5.2.5. Improved signal-to-noise with pair-finding

All data obtained from SMLM techniques is inherently noisy. All approaches suffer to some extend from falsely identified localizations, especially in thicker samples with fluorescence from the off focus areas. The only means to reduce the occurrence of false localizations from off focus fluorescence or background is raising the intensity threshold in the localization software. Hence, only strong signals are identified as localizations and off focus light is more unlikely to result in localizations. To find the optimal threshold for the best reconstruction can be rather difficult and time consuming, since it has to be determined on a case to case basis. While low thresholds result in a high noise level with a descent density of localizations to represent the imaged structure, high thresholds can compromise the density of localizations to form the structure, thereby not only lowering noise but also lowering the reconstruction quality of the imaged structure.

Signal-to-noise increase by up to a factor of four is a benefit of the spectral demixing approach, since it offers a second level of noise reduction besides the intensity threshold to identify a localization. Localizations from off focus light have a very small probability to occur as pairs. Noise-reduction is built into the spectral demixing approach: the pair-finding procedure uses two localizations to reconstruct one color-specific localization. This capability makes it worthwhile to use pair-finding even on single-color images. To test whether the pair-finding algorithm itself reduces noise, microtubles immunolabeled with Alexa Fluor 647 near the center of a NIH 3T3 cell were imaged. At this particular area of the cell the background emission from the dense intracellular cytoskeleton is higher compared to the thin periphery of the cell. A significant increase of the signal-to-noise ratio in this single color labeled sample was observed, up to a factor of four (figure 5.10). The image was acquired using the 3D SD-*d*STORM filter setup (table 5.3) and the D_2O SD-*d*STORM buffer (table 4.3). Figure 5.10 shows a reconstruction (panel a) with (upper-right) and without pair-finding (lower-left). The noise levels were much higher in-between the tubular structure without pair-finding. This is also shown in more detail in the magnified region of interest in panels b1 and b2. Depending on the initial threshold, pair-finding typically results in the loss of about 20–50 % of the total number of detected localizations. To test if structural information is discarded, the unpaired localizations

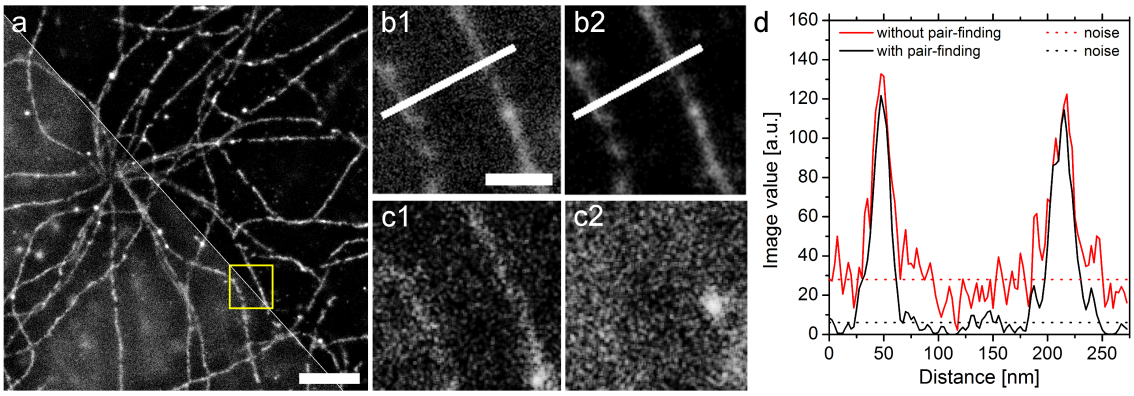

Figure 5.10.: NIH 3T3 cells were immunostained for microtubules with Alexa Fluor 647 and imaged using SD-*d*STORM. a) SD-*d*STORM reconstruction: lower-left without pair-finding, upper-right with pair-finding, scale bar 1 µm. b) Magnification of ROI in a (yellow box): b1 without, b2 with pair-finding. c) Reconstruction from the same ROI in a of unpaired localizations from short- (c1) and long-wavelength-channel (c2). For visibility, the contrast in c is raised 5-fold compared to b1, b2. Scale bar is 200 nm for b+c. d) Intensity profile from lines plotted in b1, b2. This noise reduction leads to a 4-fold increase in S/N (4.6 without pairwise sorting, 19.4 with pairwise sorting) [86].

were reconstructed in panels c1 (short-λ-channel) and c2 (long-λ-channel) of the same region of interest. While panel c2 shows no localization resembling the structure, panel c1 is showing some unpaired localizations fitting the displayed structure. This was expected since a perfect balance between an equal number of localizations from the structure is not anticipated. The signal intensity in the pair-sorted case was not visibly reduced, but the levels of noise in-between the structure was, as shown in panel d. This demonstrates that by optimizing the initial threshold, the pair-finding algorithm significantly reduces single molecule noise while only sacrificing minimal structural information.

Dividing photons from a single molecule signal into two channels resulted in slightly lower localization precision, but it was far less than typical uncertainties introduced by overlay of two colors measured separately (typical 15 nm) [113]. To investigate the dependency of noise on either threshold or the pair-finding, we analyzed the data set shown in figure 5.10 using different initial thresholds with or without pair-finding. The results are shown in figure 5.11. The image was acquired using the 3D SD-*d*STORM filter setup (table 5.3) and the D_2O SD-*d*STORM buffer (table 4.3). A low initial threshold without pair-finding included large numbers of localizations but yielded high noise levels. On the other hand, high thresholds without pair-finding resulted in similar noise reduction

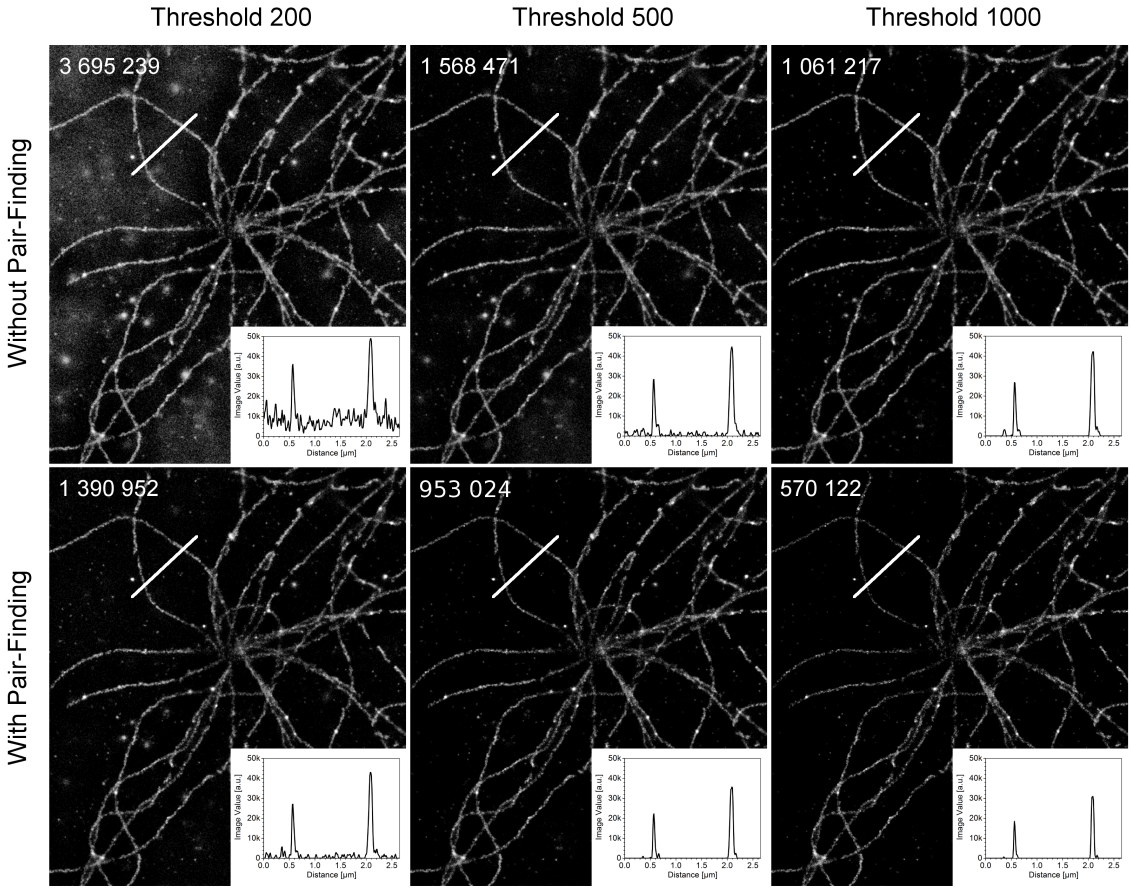

Figure 5.11.: Relation between single molecule threshold and noise. NIH 3T3 cells were immunostained for microtubules with Alexa Fluor 647. SD-*d*STORM images reconstructed with different intensity thresholds using rapi*d*STORM 3.3.1. without pair-finding (top) and with pair-finding (bottom). The number in the top-left corner of each image is the total number of localizations used to reconstruct the image. The intensity values of the image along the white line were plotted and are shown in the lower-right corner of each image [86].

than using low initial thresholds with the pair-finding algorithm. It should be noted that far more localizations were available for reconstructing the image in the case of low threshold with pair-finding compared to the high threshold case, featuring a low noise reconstruction.

Even for single color imaging, the pair-finding approach was beneficial, since a second level of noise reduction was introduced by pairing localizations. Working only with thresholds for localizations detection is fine for flat, low off focus light areas, but can lead to noisy pictures in thick, densely labeled areas of a cell. The necessity of a high fluorophore density for every super-resolution approach is described and discussed in section 3.3 on page 32. The second level of noise reduction of SD-*d*STORM can be even more useful in three-dimensional reconstruction, especially with two colors, which will be discussed in section 5.3.

5.3. Three dimensions

5.3.1. 3D by astigmatism

It is possible to acquire 3D information from two dimensional image series, showing individual molecules distorted by a cylindrical lens, as described in section 3.4.2. This approach can also be used in combination with the pair-finding algorithm of spectral demixing *d*STORM. A custom made cylindrical lens (Melles Griot, France) with a focal length of 10 m was introduced in the detection pathway directly underneath the fluorescence filter cube turrets. A simple schematic following the work of Huang et al. [20] of the optical setup is shown in figure 5.12. Also presented in figure 5.12 are images of fluorophores at different axial positions.

Fluorescent beads (TetraSpec, Life Technologies) were used to calibrate the three dimensional axial scale of the setup with the introduced cylindrical lens. The beads were immobilized on acid-cleaned coverslips using PLL (see sections 4.3.1 and 4.3.2). For initial calibration attempts, cover slips with fluorescent beads only were used to test the parameters of the setup. Later on, the fluorescent beads were added directly to every sample, since they could also be used as fiduciary markers to correct for sample drift (section 5.1.2).

The acquisition routine to obtain raw data for 3D calibration was the following: The microscope was focused with low laser intensities (about 0.5 mW) emitted from the 643 nm laser to the plane of the beads, usually directly on top of the cover slip. It was taken care that at least ten fluorescent beads were in the field of view with not a single case of two or more beads directly adjacent to each other. Then, the sample was moved up

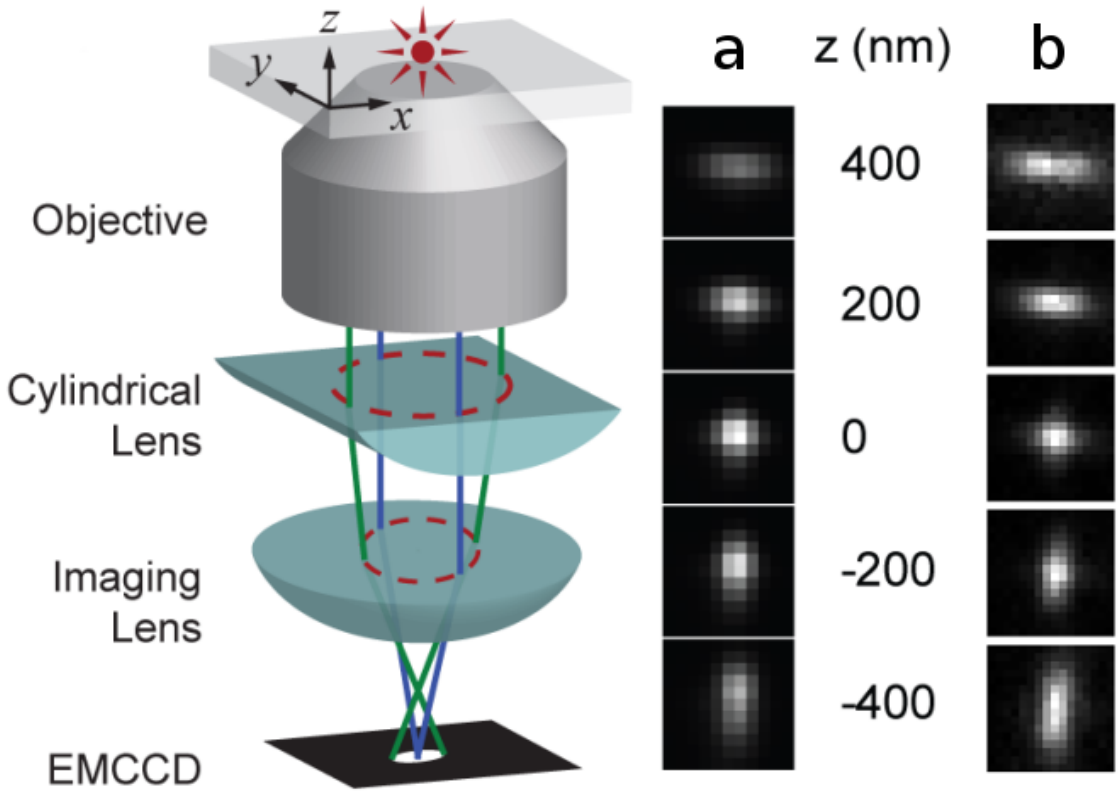

Figure 5.12.: Schematic of the 3D by astigmatism principle. a) lateral distortion of a fluorophore with respect to its position in z. b) images show a single Alexa Fluor 647 at different z-position, in the short-λ-channel acquired with the setup presented here (modified from [20]).

by 1.5 µm, using the Nano-Scan-Z. Importantly, to avoid overexposure in the field of view (FOV), the laser intensity was adjusted accordingly and image-series acquisition was commenced in steps of 10 nm in z-direction resulting in 301 images. Running this experiment with different illumination times and different laser intensities, we obtained the same results. In experiments where the beads were added to the sample, the low emission intensity of usually 0.5 mW was preferred to higher intensities to minimize photo-bleaching effects in the sample before acquisition.

The data set was opened in Fiji (see section 4.4) and a single bead was cut out in both wavelength-channels with all layers of the 301-layer image stack. These image stacks were analyzed using rapi*d*STORM 3.1.1 [134] and the process of 3D calibration was done according to the manual of rapi*d*STORM, which can be found at

- https://idefix.biozentrum.uni-wuerzburg.de/doc/rapidstorm/manual.pdf.gz.

The output of rapi*d*STORM contained data about the distorted area in x and y given in pm^2 and the z-position could be computed by the layer-number of the used image stack. Also, the sigma-table for the b-splines calculation is derived (described in detail in section 3.4.2). To check if the obtained sigma-table was valid for a 3D calibration, the x and y distortions were plotted against the z-coordinate. To get the offset between the short- and long-wavelength-channel in a SD-*d*STORM approach, distortions in x and y against z of the same bead in each channel were plotted as shown in 5.13 on the facing page.

An obvious criterion to judge whether such a plot will grant a valid 3D calibration is to check if the distortions with respect to z shows no inflection point (monotonic function). Any existing inflection point can not be ignored and needs to be corrected by e.g. adjusting the objective ring. Since an inflection point in this function of the calibration could lead to two z-coordinates with the same values in distortion, acquiring images will lead to false localization in the axial direction. Also a straight, horizontal trend in just one of the distortions will lead to false localizations in z and indicates the need for readjustment. Importantly, the conditions at which this calibration was taken, have to be kept constant during all measurements. In the presented setup this could only be achieved by very precise controlling of the temperature within the enclosure. Deviations of only 2 °C would void the calibration. Measurements of the enclosure with and without stabilized temperature are shown in section 5.3.2.

The crossing-point of the distortion in x and y in figure 5.13 corresponds to the point labeled “0 nm” in figure 5.12. The distance in z between the two crossing-points of the plots originating from the same bead were imaged in different wavelength-channels. Also

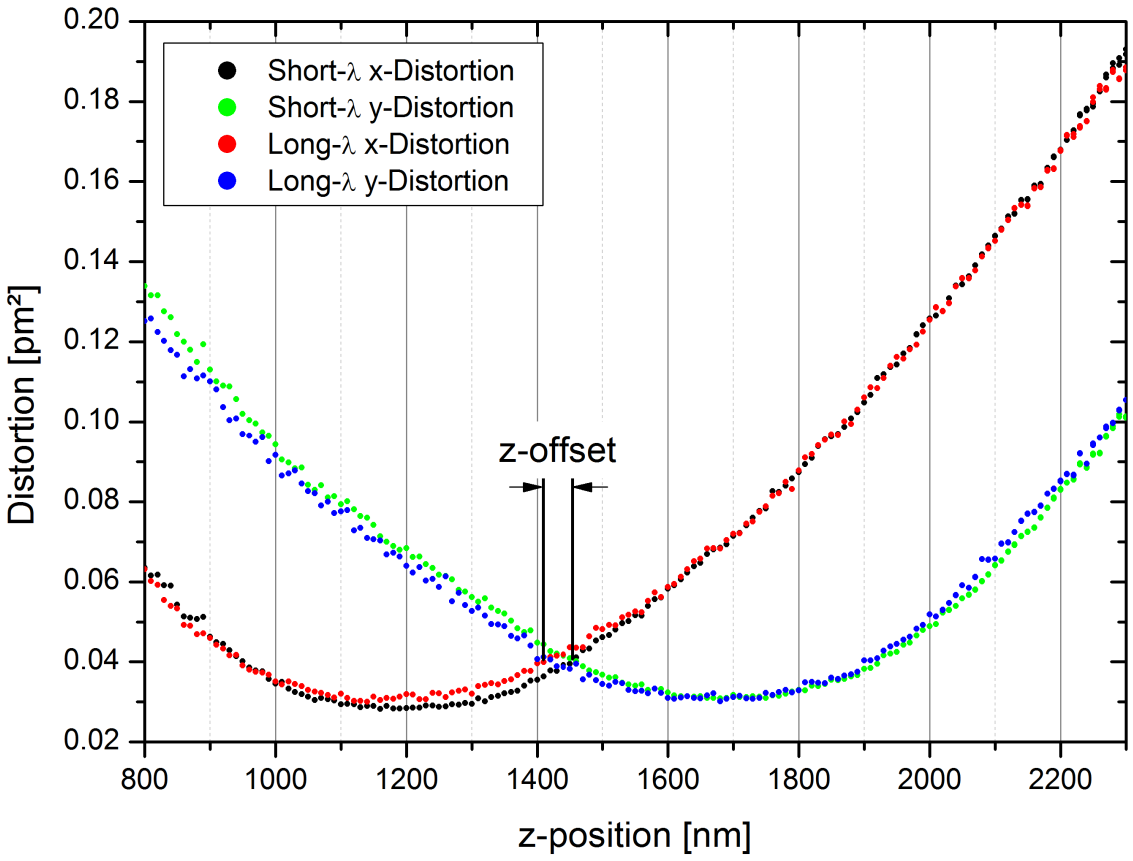

Figure 5.13.: Bead-based 3D calibration. TetraSpec beads were immobilized on a coverslip and imaged over a z-range of 3 µm using an astigmatism lens and 10 nm z-steps. The distortions of the bead images in x and y dimensions were measured using rapi*d*STORM 3.3.1 and plotted for short and long wavelength sides of the split view over z. The z-offset between x- and y-distortion was measured to be 50 nm in this example [86].

shown in figure 5.13 is a direct measure of the offset for the pair-finding algorithm. We experienced offsets between 20 nm and 60 nm as typical for the described setup. This offset does not contribute to the minimal localization precision. It is just a parameter to optimize the ability of our pair-finding-software SDmixer to find the maximal possible number of pairs in a given dataset (section 5.2.4). This turned out to be very important for 3D measurements. Since in the 2D case all localizations are used to reconstruct one image, in the 3D case the localizations are distributed also in z-direction. Assuming a minimal obtainable localization precision of 66 nm in the axial direction (section 5.4), a distance between image-planes of 25 nm in the reconstructed image stack for a 3D SD-*d*STORM measurement is sensible. With that, the localizations are distributed to 32 different image-planes, when calculating with a range of 800 nm. The range in z, in which a localization can be detected is widened by the cylindrical lens, but this will not lead to a 32-fold increase of localizations. Three- to eight-fold increases have been seen, but numbers vary a lot and are highly dependent on the field of view and the sample. Less localizations are available for three dimensional reconstruction compared to two dimensions, which makes a 3D super-resolved image of a biological structure a far greater challenge than the reconstruction of a 2D image. The reconstruction will generate a TIFF-stack with a pixel-size of 10 nm in x and y and a distance between the layers of the TIFF-stack of usually 25 nm. These values are about 2.5-fold smaller than the optimally obtainable resolution (see section 5.4). To prevent image rendering artifacts, a whole number factor between pixel dimensions and optimally obtainable resolution was avoided, hence the decimal factor 2.5. The reconstructed image stacks were processed using a Gaussian blur on the single molecule localizations with the full width half maximum (FWHM) of the determined localization precision.

The method was first tested in a single-color sample. NIH 3T3 cells were stained for clathrin heavy chain with Alexa Fluor 647 and prepared for three dimensional SD-*d*STORM imaging. The calibration was done as described above and the dataset was pair-sorted to reduce noise as discussed in further detail in section 5.2.5. A single clathrin coated pit (CCP) is shown in figure 5.14 on the next page, revealing its basket structure. The measured size of the CCP of roughly 200 nm corresponds well to the expected value of the clathrin structure, which should have a size of 150 nm [97], in addition to the size of the primary and secondary antibodies. Also the size in z-direction of about 280 nm (15 xy-slices with 20 nm distance in z) is expected due to 67 nm optimal obtainable resolution of Alexa Fluor 647 in z-direction. The image was acquired using the 3D SD-*d*STORM filter setup (table 5.3) and the D_2O SD-*d*STORM Buffer (table 4.3).

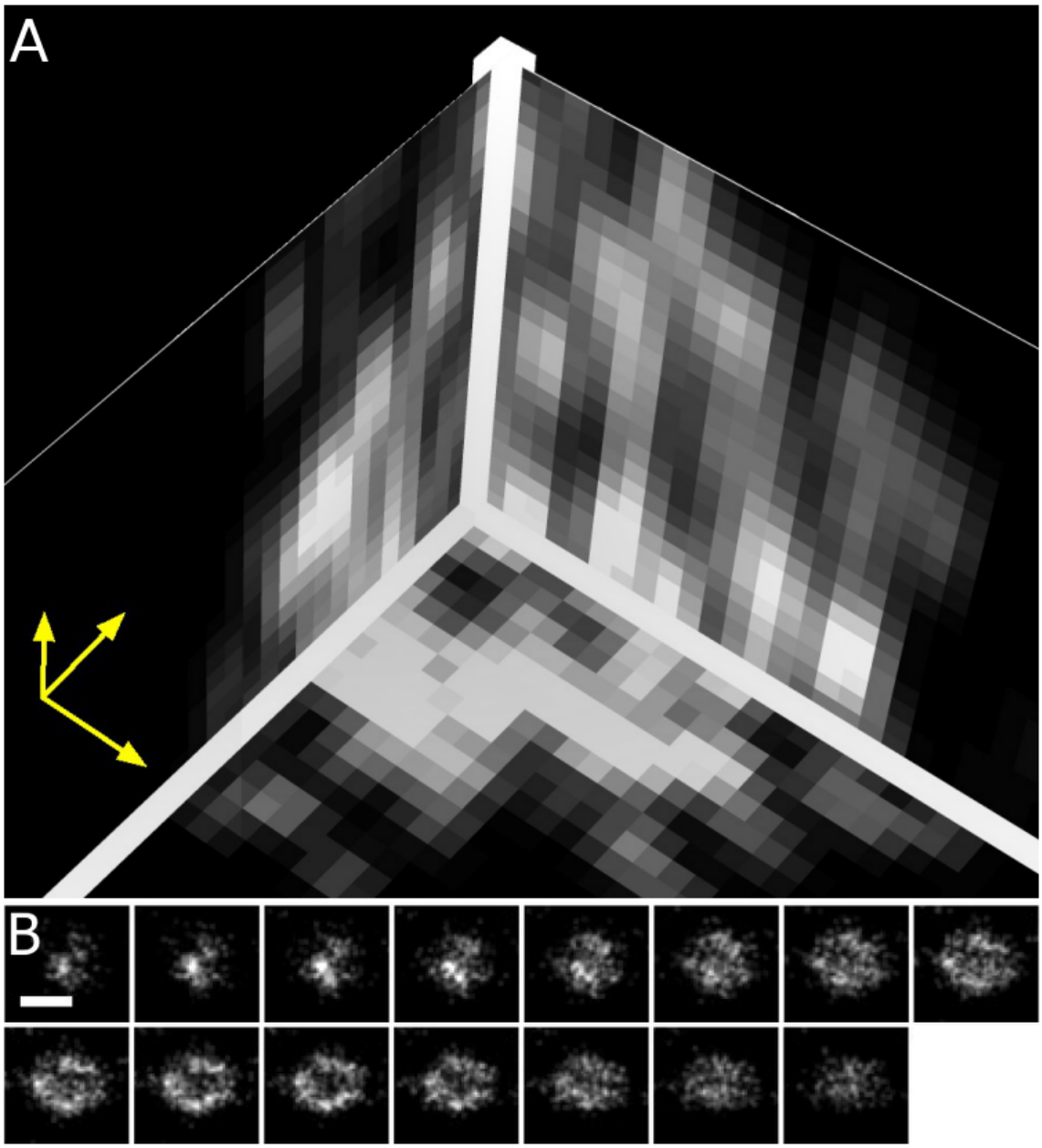

Figure 5.14.: Single-color 3D SD-*d*STORM: NIH 3T3 cells were immunostained for clathrin heavy chain (Alexa Fluor 647) and imaged with 3D SD-*d*STORM using astigmatism. A) Orthoslice view of a clathrin coated pit. The x/y-plane is at the bottom. The yellow arrows represent scale bars, 50 nm in every direction. The image was reconstructed using UCSF Chimera (table 4.5). B) x/y-slice gallery along z from data in A with z-steps of 20 nm. Scale bar: 200 nm.

An example for multicolor 3D reconstruction of microtubles and clathrin-coated-pits is shown in figure 5.15 on the facing page. The image was acquired using the 3D SD-*d*STORM filter setup (table 5.3) and the D_2O SD-*d*STORM buffer (table 4.3). The figure shows a representation with color coded z-information, a dual-color reconstruction of several planes as well as a measurement of reconstructed microtubles in z-direction. The axial width of the reconstructed microtubles of 100 nm and 160 nm is in line with the optimally obtainable resolution discussed in section 5.4. Possible improvements to 3D are discussed in section 7.1.3 on page 102.

5.3.2. Temperature stability

The temperature at the sample stage of the microscope was not stable over the course of experiments involving the fluorescence lamp or the lasers, even when the fluorescence lamp was only turned on and not used to acquire images. Temperature stability is crucial, especially when taking images for three-dimensional reconstruction in SD-*d*STORM. To control potential temperature deviations, the temperature was measured using a TFD 128 (ELV, table 4.4).

Figure 5.16 on page 80 shows that the temperature at the sample stage was influenced by the use of light sources and whether the microscope and stage was switched on or not. Temperature varied from just below 17 °C up to nearly 24 °C during the observed time period. For 3D SD-*d*STORM acquisition a change of the temperature of only 2 °C was found to void the calibration. To stabilize the temperature inside the enclosure around the microscope, several settings of the rooms air-conditioning and of the enclosures heating unit were tested. The most useful setting was found to be 23 °C for the room air-condition and 24 °C for the enclosure heating unit (OkoLabs). The temperature stability achieved with these settings is shown in figure 5.17. Although temperature equilibrium was reached within two hours, the setup was kept on (except the light sources) during the week and only powered down on experiment-free weekends. This was done to avoid heat-sink effects, which could occur and are difficult to detect by air temperature measurements, even when in close proximity to the sample stage.

A not investigated problem was the potential heating effect of the 643 nm laser during the acquisition of the raw data. This usually takes between five and twelve minutes and during that time the sample could have been heated by the laser that was emitting about 150 mW. Since the volume of the imaging buffer was only 100 µl, even tiny absorption effects could have led to a significant raise in temperature despite of the high thermic capacity of water. So far, no negative effects in the three dimensional reconstruction could be found indicating such a behavior, but since measurements of such a temperature

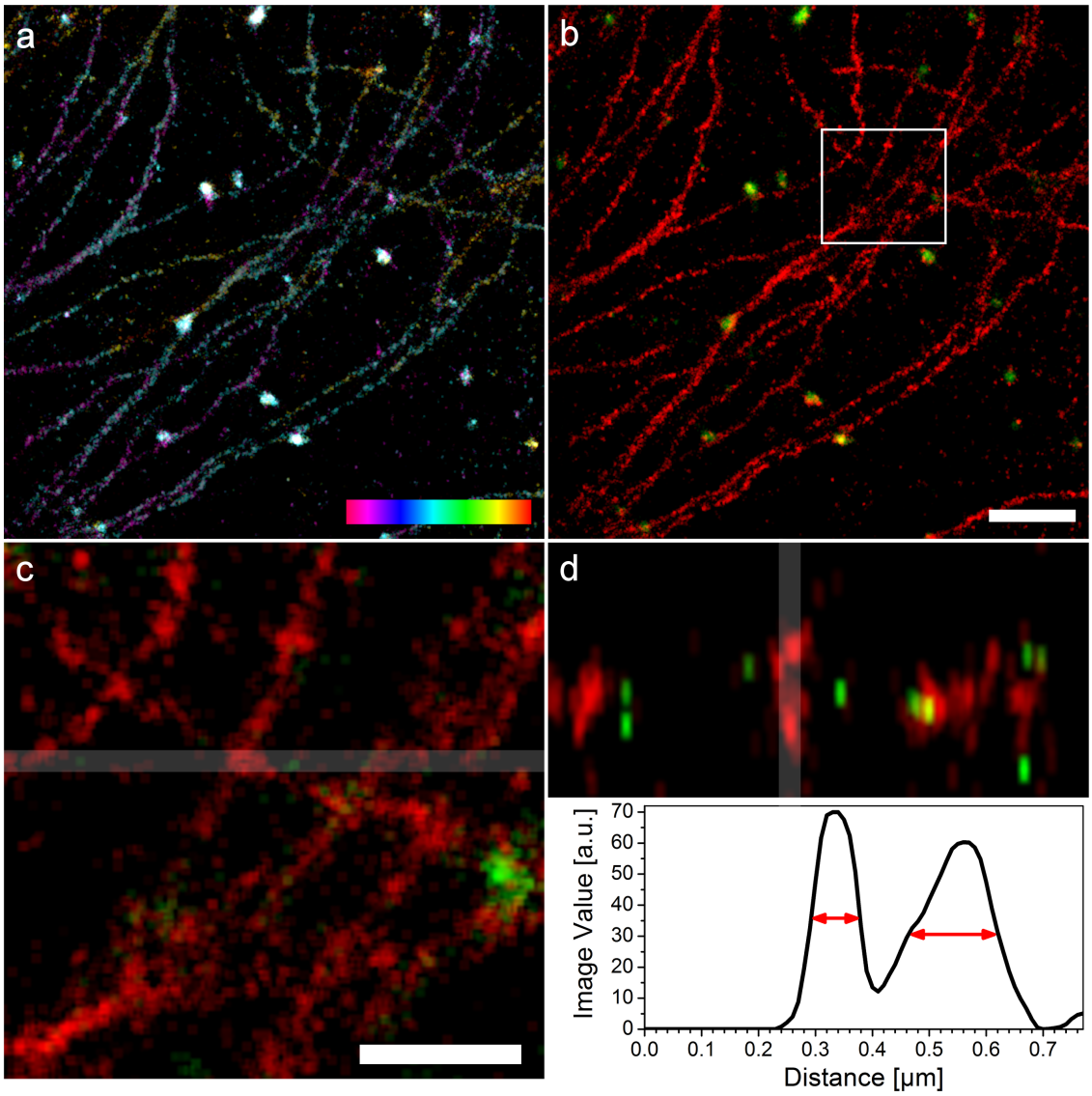

Figure 5.15.: 3D SD-*d*STORM. NIH 3T3 cells were immunostained for microtubules (Alexa Fluor 647), clathrin heavy chain (Dyomics 678) and imaged with 3D SD-*d*STORM using astigmatism. (a) Color-coded z projection from a whole stack of non-demixed dataset, the color bar ranges 200 nm from left (magenta) to right (red). (b) Projection of three SD-*d*STORM z-planes, scale bar 1 µm. (c) Area marked in (b), the gray area marks the area of x–z-projection in (d), scale bar 500 nm. (d) Projection of four x–z-planes, the gray area marks the region of the axial (z) intensity line profile shown below. Image values of the line profiles represent the values after reconstruction and Gaussian blur. Modified from [86].

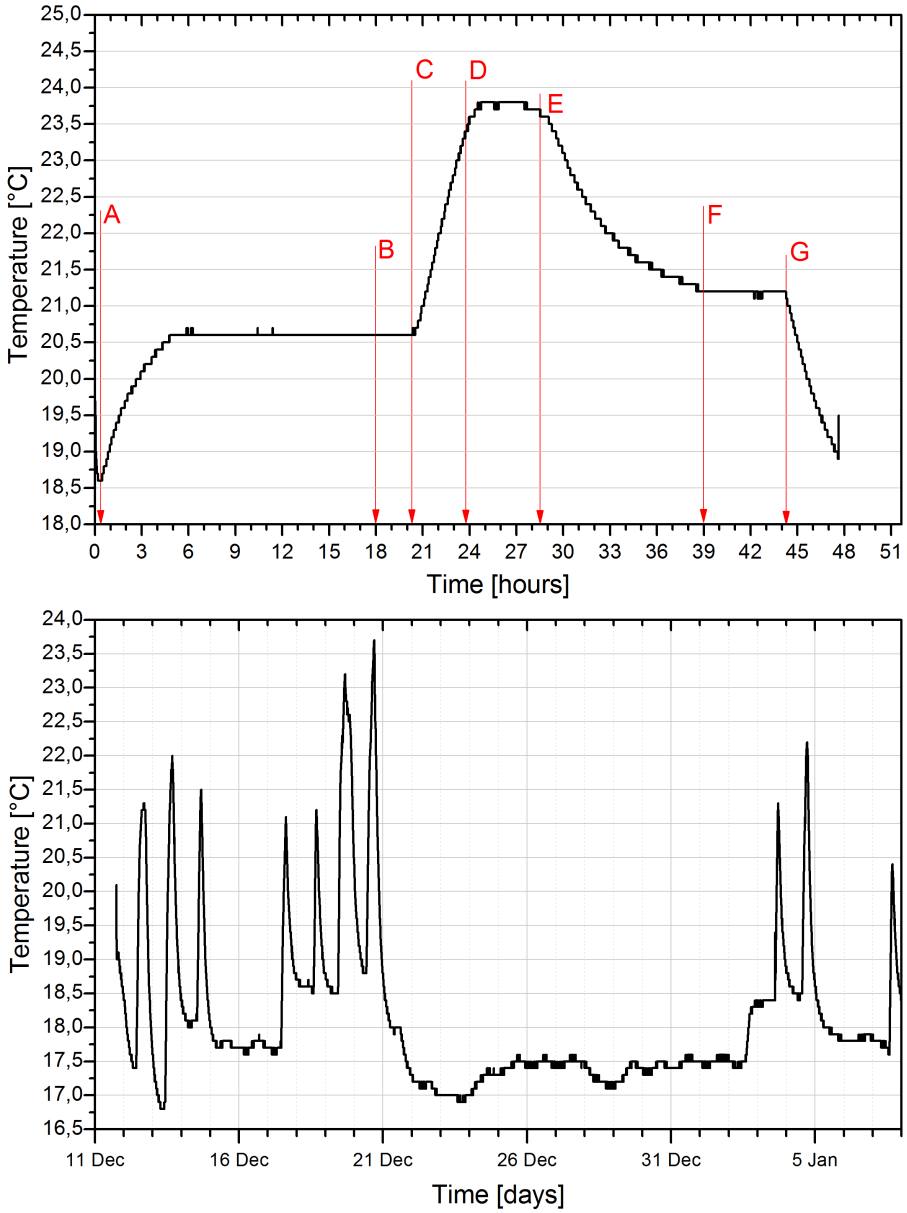

Figure 5.16.: Temperature on the sample stage plotted against time. The upper graph shows a time course over 48 hours, the red arrows highlight the following events: A) powering up the microscope and sample stage, B) next day, C) beginning of experiments with fluorescence lamp, D) fluorescence lamp power down, experiments with lasers only, E) experiments done, lasers powered down, F) still switched on microscope and stage reached temperature equilibrium, G) power down of microscope and sample stage. The lower graph shows a time course of several laser experiments without the use of the fluorescence lamp from December 11th 2012 to January the 8th 2013. The System was powered down on the weekends and over the Christmas holidays, only light sources were powered down during the week.

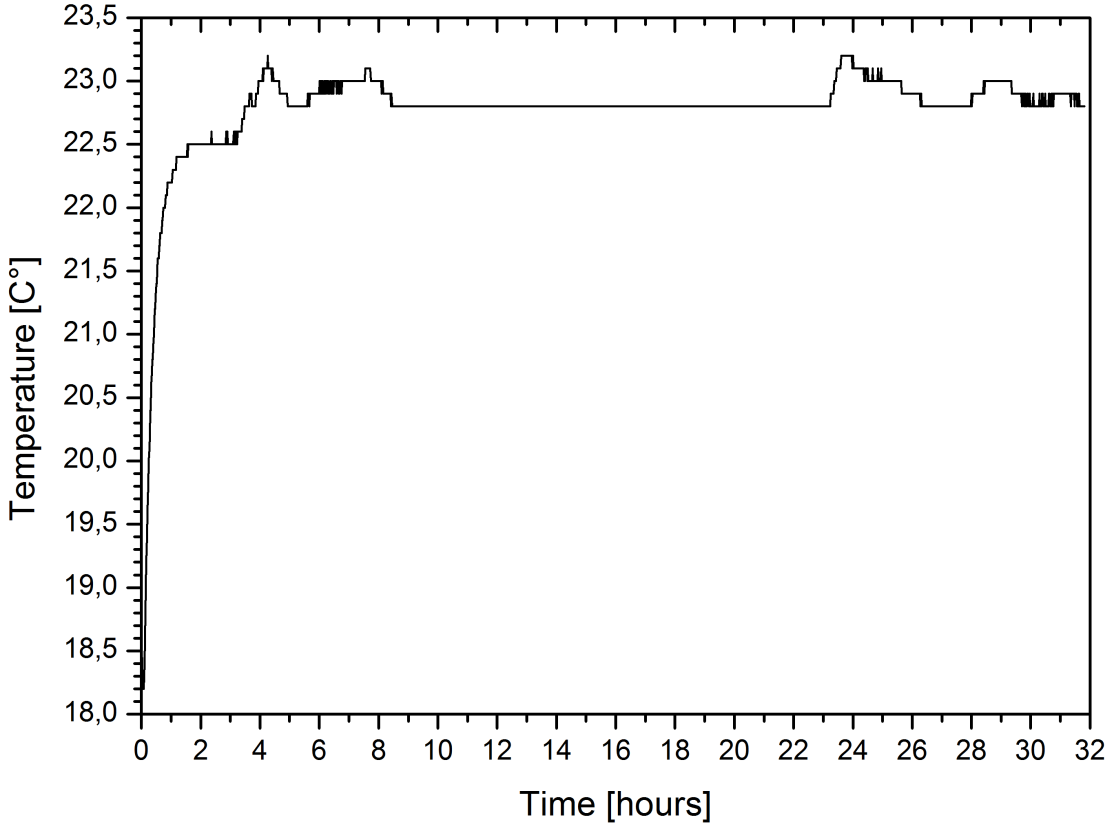

Figure 5.17.: Temperature on the sample stage plotted against time. The measurement was taken with running air conditioning in the room and the incubator heating set to 24°C. During this measurement three experiments with laser light were performed lasting several hours.

change in the sample could not be done with the equipment at hand, a temperature change during acquisition can not be ruled out. This is discussed in further detail in section 7.1.3 on page 102.

The movement of the air inside the enclosure contributed a lot to sample drift. A drift of about half the magnitude of the drift shown in figure 5.3 on page 57 has been detected without heating and air-flow inside the enclosure. This sample-drift showed a predominantly linear direction. Hence, if sample drift would have occurred without temperature control, it would have pointed to a heating effect in the sample during measurement as mentioned above. Such a drift still had to be corrected for as described in section 5.1.2 on page 56. Given that a 3D calibration would have been voided after a short time without temperature control, the air-conditioning and the enclosure heating unit were used in every measurement.

5.4. Experimental localization precision and optimally obtainable resolution

To determine the minimal localization precision, a special antibody-staining was prepared. Cells were fixed, permeabilized and stained with primary antibodies against microtubles. Then, a standard concentration of secondary antibodies labeled with Alexa Fluor 488 was mixed with 0.02 % of secondary antibodies labeled with Alexa Fluor 647 or Dyomics 678 to get a very sparsely labeled biological sample in the far red portion of the spectrum. The Alexa Fluor 488 was applied to find the right focal plane within the sample, before switching to high laser powers at 643 nm wavelength. The entire field of view of the camera was showing microtubles in the 488 nm channel and the focal plane was selected in such a manner that localizations could occur above and below the focal plane, for both the two and the three dimensional case. The whole process was repeated three times and all resulting localization information was pooled for statistical analysis. Every cluster of localizations with at least five localizations was transferred to a coordinate system with its center of intensity as origin. In general the equation of such a weighted coordinate transformation is

$$\overrightarrow{O} = \frac{1}{I_{sum}} \sum_{i=1}^{n} I_i \left(\overrightarrow{r_i} - \left(\frac{1}{I_{sum}} \sum_{j=1}^{n} I_j \overrightarrow{r_j} \right) \right) \tag{5.1}$$

where $\overrightarrow{O}$ is the origin of the coordinate system, I_{sum} the sum of all intensities in one cluster of localizations, I_i the intensity of the i-th localization of the cluster, $\overrightarrow{r_i}$ the

position of the i-th localization of the cluster and n the number of localizations in the cluster [14].

This leads to an overlay of all localization clusters at the origin of a coordinate system. A frequency count for lateral (x and y combined) and z-direction was done using binning steps. The results are depicted in figure 5.18 on the following page. The frequency distribution was fitted with a Gaussian function of the type

$$f(x|\sigma) = \frac{1}{\sigma\sqrt{2\pi}} e^{-\frac{x^2}{2\sigma^2}}, \tag{5.2}$$

which resulted for Alexa Fluor 647 in a lateral full width half maximum (FWHM) of 25 nm and a axial FWHM of 67 nm. For Dyomics 678 the FWHM was determined to be 26 nm lateral and 66 nm axial. The FWHM are satisfying the Rayleigh-criterion (section 3.1.1, p. 15) and are considered as the minimal localization precision of this approach.

For a biological structure this means that the expected size will be bigger by at least the FWHM of the corresponding fluorophore. The size of the used labeling technique, e.g. primary and secondary antibodies, has to be considered in addition to this. A microtubule for instance is known to have a hollow, tubular structure with a diameter of 25 nm. When labeled with primary and secondary antibodies on the outside, those antibodies contribute roughly 10 nm in every direction. For a two-dimensional measure of a microtubule labeled in such a way, a width of 25 nm plus 10 nm for antibodies on each side should be considered. Adding the FWHM of 25 nm in x and y for Alexa Fluor 647 to this 45 nm would result in a measured width of about 70 nm for a fully, densely labeled microtubule in the 2D case. For three-dimensional measurements of the width the same is true for adding 45 nm to 67 nm for Alexa Fluor 647, a fully and densely labeled microtubule should show about 112 nm width in the z-direction of a 3D SD-*d*STORM reconstruction. That this is achievable with 3D SD-*d*STORM is depicted in figure 5.15 on page 79, showing a measured size of microtubles in z direction of 100 nm and 160 nm.

5.5. Data structure

The software SDmixer (section 5.2) was developed and further improved during this thesis. But also updates to third-party software like µmanager [9] and rapi*d*STORM [134] took place. This had a significant impact on the number and the size of files containing the raw data as well as the reconstructed images.

With µmanager version 1.4+ and a change to a 64 bit operation system on the computer controlling the microscope enabled acquisition of more than 4 GB of raw data in one

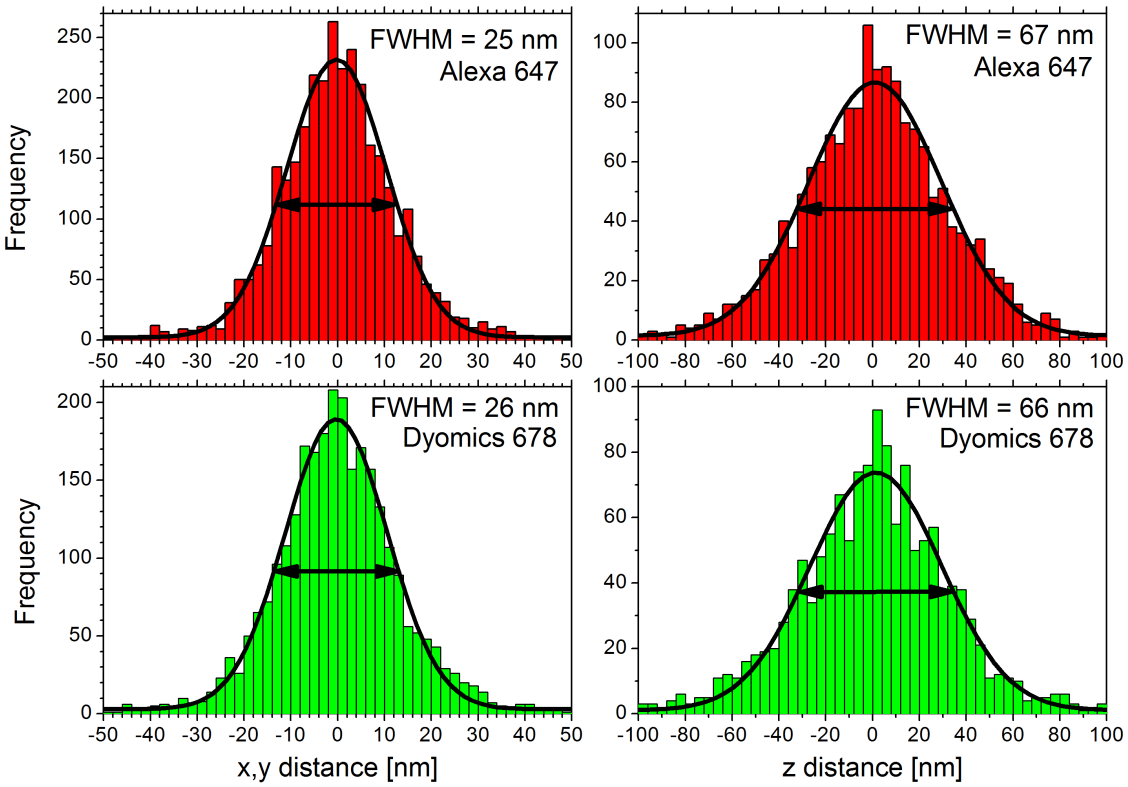

Figure 5.18.: 3D resolution of SD-*d*STORM. NIH 3T3 cells were sparsely immunostained for microtubules with either Alexa Fluor647 or Dyomics 678, co-labeled with Alexa Flour 488 (diluted 1:5000) to find the focal plane and imaged using SD-*d*STORM. Localization clusters (minimum of five localizations) were overlaid according to their center of mass and distances from the center were calculated. The frequency is shown for lateral (x and y) direction (left) and for the axial (z) direction (right) for Alexa Fluor 647 (red) and Dyomics 678 (green). The FWHM of the Gaussian fit across the distributions represents the experimental localization precision of single fluorophores [86].

SD-*d*STORM	file	size
2D & 3D	raw_data_0.TIF	4 GB
	raw_data_1.TIF	2.6 GB
	rapi*d*STORM_settings.TXT	a few kB
	rapi*d*STORM_localizations.TXT	100-900 MB
	sdmixer_log.TXT	a few kB
	SD-reconstruction-color1.TIF	1-50 MB
	SD-reconstruction-color2.TIF	1-50 MB
	localization-pairs-out.TXT	100-900 MB
	localization-pairs-filtered-out.TXT	100-900 MB
	SD-2D-intensity-space.PNG	approx. 200 kB
3D only	sigma-lookup-table.TXT	a few kB

Table 5.5.: Output files of the SD-*d*STORM approach and approximated sizes for 36 µm × 17.5 µm field of view (see figure 5.8, p. 67) and 20000 frames of raw data. The spectrally demixed reconstructions (SD-reconstruction-color1&2.TIF) are LZW compressed [138]. The given sizes are estimations for 2D and 3D cases.

measurement by automatic separation of the raw data in several 4 GB TIFF-stacks. At the same time rapi*d*STORM, from version 3 on, was capable of combining several TIFF-stacks to a single analysis. The 4 GB file-size limit was given by the definition of the TIFF format, and could not be circumvented, since no other open image-format was capable of handling uncompressed 16 bit gray-scale data. Table 5.5 shows the files and approximated sizes of a typical, two color measurement. The spectrally demixed reconstructions of the individual colors are contained in a TIF file (2D) or in a TIF-stack file (3D) and were LZW compressed. LZW is an abbreviation for Lempel-Ziv-Welch, a universal lossless data compression algorithm [158, 167].

The LZW compression of spectrally demixed reconstructions was necessary, especially in the 3D case. With a 36 µm × 17.5 µm field of view and a axial depth of about 1 µm (see section 5.3), the uncompressed reconstructed TIFF-stack for one color would be the size of 1.6 GB [138]. With LZW compression the items shown in table 5.5 already totalize to about 10 GB size for one measurement, under the assumption that more than 10^7 localizations were found.

The raw data recorded for this thesis adds up to more than 10000 GB (10 TB) of raw data organized in more than 5400 folders, containing more than six million files. Even though a strategy for naming experiments was worked out before starting the first acquisition, the same strategy was changed several times due to new developments in

the software mentioned above and due to new requirements for 3D. The latter needed a set of different files, raw data as well as intermediate results, leading to a 3D calibration in form of a sigma lookup table. It is included in table 5.5 since a sigma lookup table can also be derived from the raw data of a biological sample, since every sample needs to have standardized fiduciary markers for drift correction (see section 5.1.2).

6. Cell biology applications

The spectral demixing approach of SD-*d*STORM or the custom-build setup as a TIRF microscope was used to obtain images in different studies in the membrane biochemistry field.

6.1. GIT1 at the neuronal active zone

Synaptic transmission involves the rapid calcium-triggered exocytosis of synaptic vesicles (SVs) at presynaptic active zones (AZs) [53] followed by SV protein endocytosis at the rim of the AZ [155]. The AZ membrane is associated with an electron-dense protein matrix, named the cytomatrix of the active zone (CAZ). The components of the CAZ include giant multidomain proteins such as piccolo, bassoon and G protein coupled receptor kinase 2 interacting protein (GIT) [79] beside others. The mammalian GIT1 is a scaffold protein, which possesses a GTPase activating domain for ADP ribosylation factor 6 (Arf6) and among other factors associates with CAZ components [79]. GIT1 also regulates endocytic membrane traffic, suggesting a potential presynaptic function in SV exo-endosytosis [30]. As GIT1 is genetically linked to attention-deficit hyperactivity disorder (ADHD) [66], the understanding of the role of GIT in presynaptic SV recycling is important for the understanding of neurological and neuropsychiatric diseases. The localization and the role of GIT1 in the presynapse has been investigated in the work of Jasmin Podufall et al. [117]. We used SD-*d*STORM to analyze the localization of GIT1 and the AZ protein bassoon (Bass) at hippocampal synapses, since the size of active zones is below the diffraction limit.

The scaffold protein GIT1 localized to distinct puncta at the periphery of the active zone center defined by bassoon, shown in figure 6.1 on the next page. The mean peak distance between individual bassoon spots and GIT1 was 76 ± 8 nm (standard error of the mean, n = 30 synapses). This is similar to the distance measured by STORM for bassoon and the AZ protein RIM1 (mean ± SEM, 40 ± 5 nm) and as expected much smaller than the distance between bassoon and the postsynaptic protein Homer1 (mean ± SEM 154 ± 1.2 nm) [2]. The analysis using images acquired with SD-*d*STORM were the start-

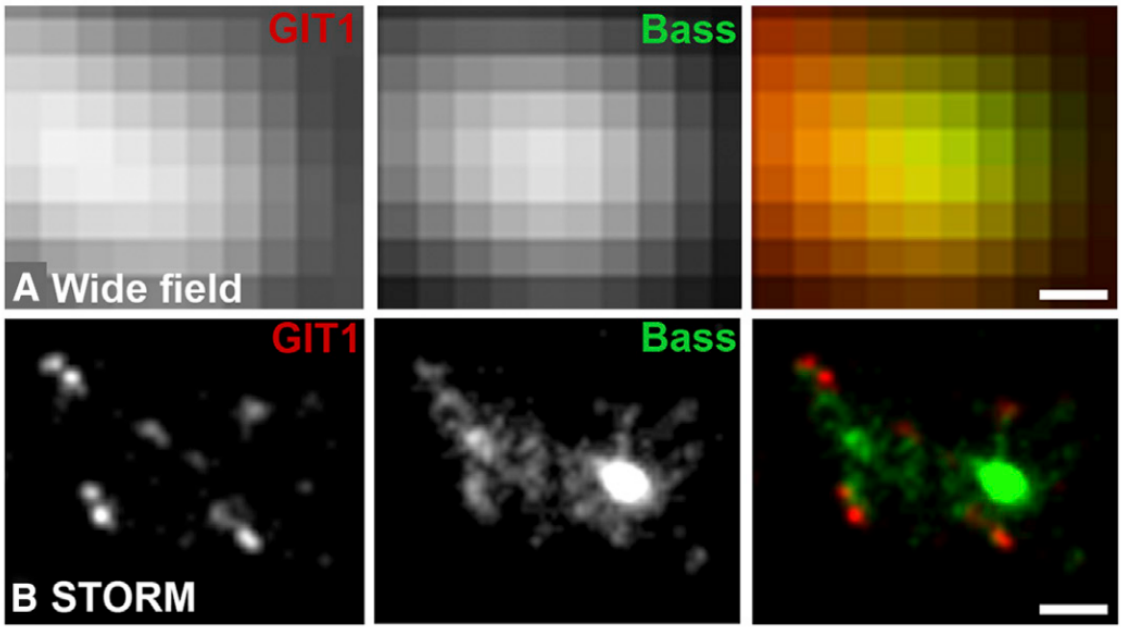

Figure 6.1.: GIT1 localizes to distinctive puncta at the periphery of the active zone center. Cultured hippocampal neurons (DIV14) co-stained for GIT1 (red, Alexa Fluor 647) and bassoon (Bass, green, Alexa Fluor 700) shown in wide field (A) or SD-*d*STORM (B). Scale bars, 200 nm ([117], figure 1).

ing point in the study published by Jasmin Podufall et al. [117]. It led to the finding that GIT1 physically and functionally associates with the endocytic adapter stonin2/stoned B. This, together with several other findings of the study, favor a hypothetical model in which GIT acts as a molecular bridge for the recruitment of stonin 2/stoned B to the periphery of the active zone. A physical connection between the AZ-based exocytic apparatus and the endocytic machinery may regulate vesicle reformation and thus availability, thereby contributing to efficient synaptic vesicle exo-endocytic cycling [155].

The preparation of the cells was done by Jasmin Podufall. The mounting in "old" SD-*d*STORM buffer (table 4.3), the application of fluorescent beads to the sample for drift correction (section 4.3.2) and the imaging was done by the author of this thesis. The first SD-*d*STORM filter setup was used for image acquisition, see table 5.3. Measurements and reconstruction of the acquired data were done in close collaboration with Jasmin Podufall.

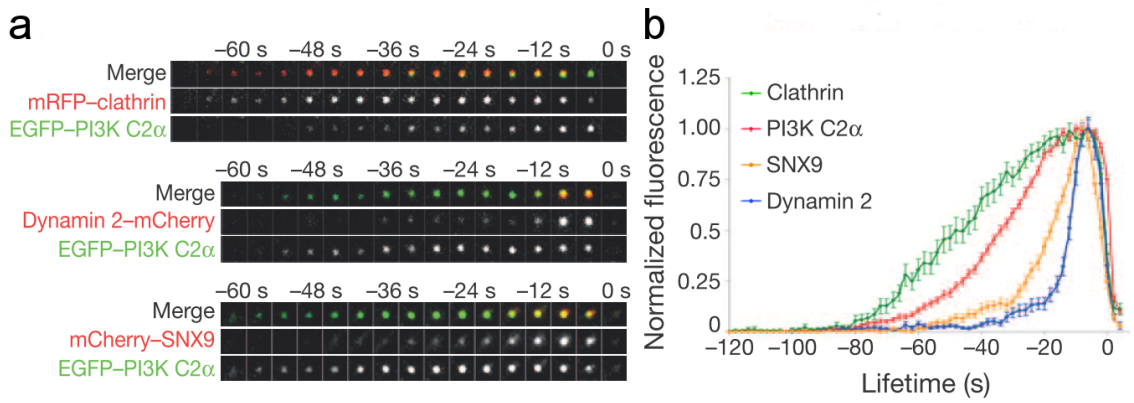

Figure 6.2.: Timing of recruitment of PI(3)KC2α and SNX9 to clathrin coated pits analyzed by TIRFM. a) Different time points of endocytic proteins at single clathrin coated pits. b) Mean time course of relative fluorescence intensity at clathrin coated pits (mean ± standard error of the mean; three experiments for clathrin, dynamin2 and PI(3)KC2α, two for SNX9; total number n of clathrin coated pits: n = 59 for clathrin, n = 85 for dynamin2, n = 248 for PI(3)KC2α, n = 100 for SNX9), modified from [165].

6.2. SNX9 recruitment

The PX-BAR domain scaffold protein Sorting Nexin 9 (SNX9) is a member of the sorting nexin family. All members of that family have in common that they possess a characteristic lipid binding PX domain. The role of the different SNX proteins is determined by a variety of additional domains [33]. In the case of SNX9, the PX domain binds specificly to phosphatidylinositol-4,5-bisphosphate ($PI(4,5)P_2$) and to phosphatidylinositol-3,4-bisphosphate ($PI(3,4)P_2$) as well as to phosphatidylinositol-3-phosphate (PI(3)P), a lipid absent from the plasma membrane [165, 163, 94, 132]. SNX9 prefers association with $PI(3,4)P_2$ compared to $PI(4,5)P_2$, which itself is preferably bound by many other adaptor proteins like AP-2α. Thus, SNX9 is a putative $PI(3,4)P_2$ effector in clathrin mediated endocytosis.

In our study Posor et al. [165] we observed dynamic growth of short SNX9 tubules from clathrin coated pits immediately prior to fission (see time points in figure 6.2). An important protein also involved in this is dynamin2, a GTPase recruited very late to the site of a newly formed vesicle, just prior to scission. How the presence of dynamin2 influences the growth of SNX9 tubules from clathrin coated pits was also an open question. SD-*d*STORM was used to address this question by acquiring super resolution images of endogenous SNX9 and PI(3)KC2α (figure 6.3).

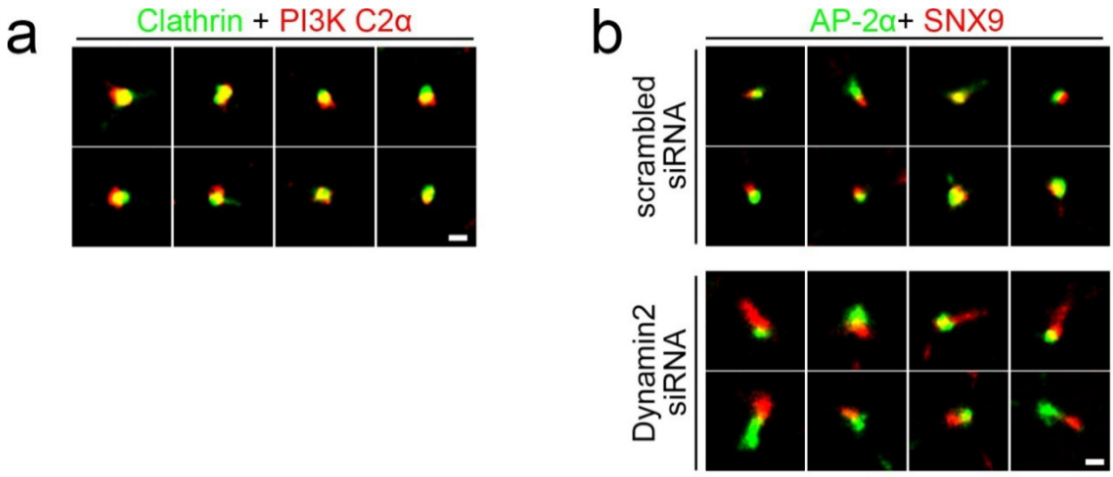

Figure 6.3.: Localization of endogenous SNX9 at clathrin coated pits in Cos7 cells. a) A Gallery of clathrin (Alexa Fluor 700) and Pi3K C2α (Alexa Fluor 647) at endocytic CCPs. b) Two galleries, endogenous AP-2α (Alexa Fluor 700) and SNX9 (Alexa Fluor 647) at endocytic CCPs, top panel: control conditions, bottom panel: dynamin2-depleted conditions. Scale bars 150 nm.

The scaffolding protein clathrin and PI(3)KC2α show a close overlap (figure 6.3a) but SNX9 appeared rather adjacent to the endocytic protein coat, which was made visible by staining AP-2α with fluorophore coupled antibodies. The effect appeared more distinct when dynamin2 was depleted (figure 6.3b, lower gallery). These elongated structures are most likely the necks of stalled clathrin coated pits.

The preparation of the cells was done by York Posor, described also in [165]. The mounting in "old" SD-*d*STORM buffer (table 4.3), the application of fluorescent beads to the sample for drift correction (section 4.3.2) and the imaging was done by the author of this thesis and in part by York Posor. The first SD-*d*STORM filter setup was used, see table 5.3. Reconstruction of the acquired data and measurements were done in close collaboration with York Posor.

6.3. STOML3 in sensory neurons

The mouse stomatin-like protein 3 (STOML3) is a member of the stomatin-domain family of proteins that is required for normal mechanotransduction in touch receptors [29]. STOML3 can tune the sensitivity of sensory neurons to mechanical stimuli by interacting with piezo proteins [77], which have been identified as true mechanosensitive ion channels

implicated in sensory mechanotransduction, in rat dorsal root ganglia (DRG) neurons as well as in fruit fly larvae [17, 32, 136]. The modulation of mechanotransduction by STOML3 is dependent on its ability to oligomerize [77].

The *d*STORM technique described in this thesis was used in a study led by Gary Lewin and Kathryn Poole to investigate the clustering of STOML3 in the plasma membrane of sensory neurons (manuscript in review). The sizes of STOML3 clusters at the plasma membrane under different conditions were quantified. It could be shown that STOML3 was present in distinctive microdomains at the plasma membrane (figure 6.4A, page 92).

The finding is consistent with previous studies suggesting that stomatin-domain proteins may associate with cholesterol-rich lipid raft microdomains [64, 91]. The size of the STOML3 clusters were variable with a measured full width half maximum (FWHM) of 24.6 ± 2.8 nm. These domains must contain more than one STOML3 dimer, as their size was predicted to be about 10 nm^2 [25]. Introduction of the V190P mutation disrupts oligomerization of STOML3 and abolishes its ability to modulate Piezo1 channels [77]. This STOML3-V190P variant exhibits significantly smaller clusters in the plasma membrane, shown in figure 6.4B, demonstrating that by disrupting STOML3 oligomerization one can manipulate and observe nanoscale changes in STOML3 cluster size. For the other conditions shown in figure 6.4, the STOML3-FLAG expressing N2A cells were preincubated with one of four different small molecule compounds. These small molecules were screened for their ability to prevent (OB-1 and OB-2) or accelerate (OE-1 and OE-2) de novo STOML3 self-association. Both OB-1 and OB-2 treated cells exhibited significantly reduced STOML3-FLAG cluster sizes compared with untreated cells. The opposite effect was observed in cells treated with OE-1 with cluster size increasing significantly compared to controls. The OE-2 molecule had no significant effect on cluster size. The effects of OB-1 and OE-1 could not be attributed to changes in the levels of Stoml3 mRNA in these cells. These data suggest that STOML3 clustering at the plasma membrane can be manipulated directly by controlling STOML3 oligomerization.

The preparation of the cells were carried out by Kathryn Poole. The mounting in single color *d*STORM buffer (table 4.3) and the development of a protocol to have fluorescent beads in the sample for drift correction (section 4.3.2) as well as the imaging was done by the author of this thesis. Reconstruction of the acquired data and measurements were done in close collaboration with Kathryn Poole.

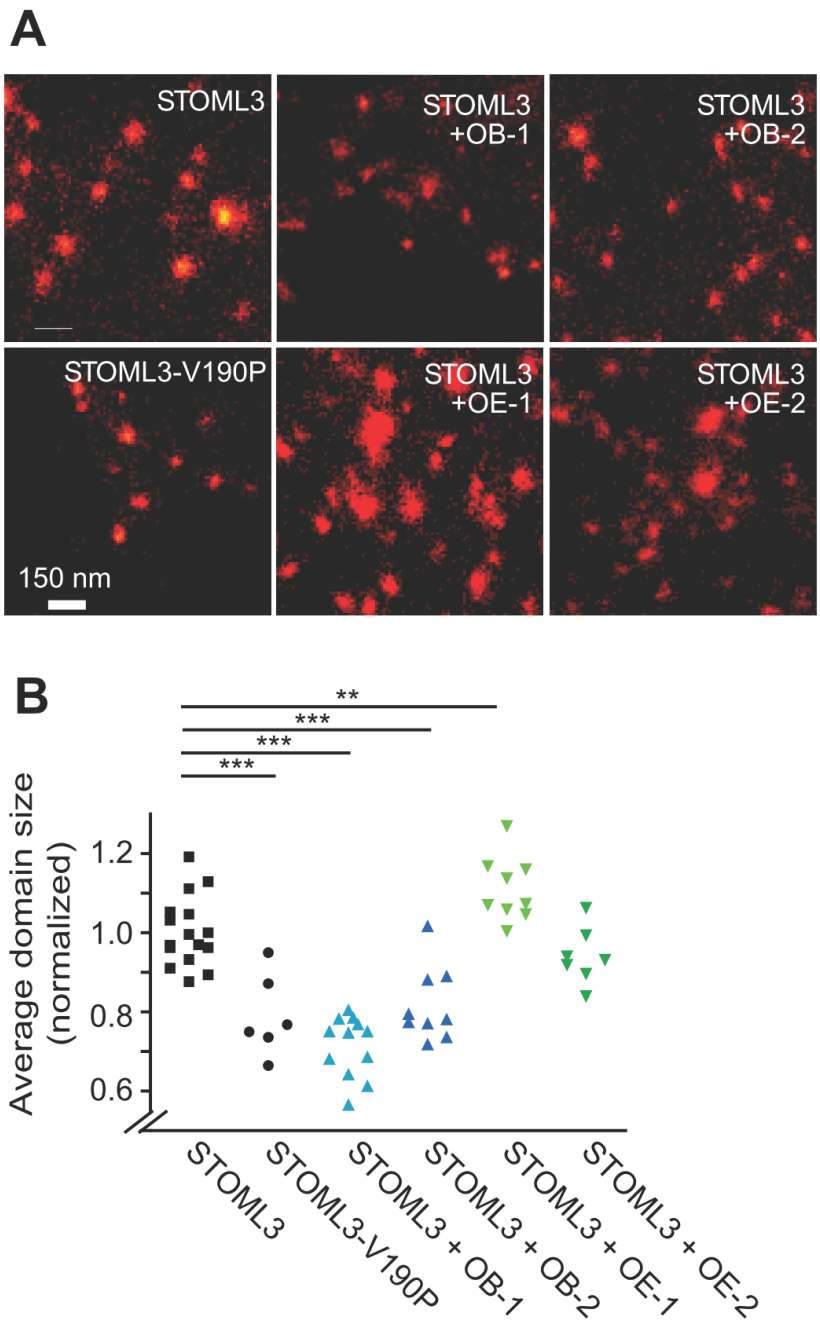

Figure 6.4.: Effects of STOML3 modulating molecules on the size of STOML3 domains in the plasma membrane. A) Representative reconstructed *d*STORM images of STORML3-FLAG overexpressed in N2A cells, labeled with Alexa Fluor 647, imaged in single color *d*STORM buffer. B) Normalized distribution of STORML3-FLAG domain size as detected by *d*STORM imaging. Each data point represents a single cell, for each cell the FWHM of 100 randomly chosen domains was measured. Figure from Poole et al., manuscript under review.

6.4. GPCRs and the setup as a single molecule TIRF microscope

The G protein-coupled receptors (GPCRs) are a large protein family of receptors that sense signals on the outside of the cell and activate signal pathways on the inside, when triggered. They are also referred to as seven-transmembrane receptors because they pass through the cell membrane seven times [146]. GPCRs are one of the most important drug targets, since they are the largest group of transmembrane receptors in the plasma membrane of mammalian cells. It is known that the smallest functional unit of a prototypical GPCR is a monomer [44, 159, 120]. Meanwhile it became clear that most of the receptors form homo-, heterodimers or different oligomers [143, 92]. An exclusive expression of a GPCR as a monomer seems to be rare and was experimentally shown only for a limited amount of GPCRs, such as the $CRF_{2(a)}R$ [140]. The functional significance of GPCR dimerization or oligomerization was shown to play a role for different functions such as receptor trafficking [116], ligand binding [149] and G protein coupling and selectivity [4].

The vast majority of the studies addressed GPCR dimerization only at a qualitative level, i.e. it was analyzed whether or not dimers are formed. Only very recently, it was examined whether dimeric GPCRs are expressed exclusively as dimers or as a mixture of monomers and dimers. In these studies, it was shown by single molecule total internal reflection microscopy (smTIRFM) that the M1 muscarinic receptor [59], the N-formyl peptide receptor [74], and the β1-and β2-adrenergic receptors [27] are expressed in the plasma membrane as such a mixture. Moreover, it was demonstrated that dimers can fall apart, suggesting that the interaction of the individual protomers is dynamic. The detected amount of dimers was different and varied between 20 % for the M1 muscarinic receptor [59] up to 60 % for the β2-adrenergic receptor [27].

However, studies addressing the monomer/dimer equilibrium of GPCRs did mainly use smTIRFM [59, 27, 74]. Although this technique has many advantages such as the possibility of defining the exact dimeric/oligomeric state of GPCRs and the dynamic interactions of the protomers at a single molecule level, it also has one major drawback. The measurements are limited to the plasma membrane, and consequently, the monomer/dimer equilibrium of GPCRs in intracellular compartments cannot be studied.

In collaboration with Anke Teichmann, we used the single molecule imaging capabilities of our setup to show that the GPCR CRF_1R is partly dimerized at the plasma membrane [139]. GPCRs are functional as monomers but the vast majority of the receptors forms dimers. These dimers can fall apart, i.e. the interaction of the individual protomers is dynamic. The work of Anke Teichmann uses fluorescence cross-correlation spectroscopy

(FCCS) to address the question of monomer/dimer equilibrium of GPCRs. Here, to be comparable to previous works, the SD-*d*STORM setup was used to do smTIRFM, taking benefit of the high sensitivity of our EMCCD camera and the capability of switching to TIRF mode. Apart from comparability, smTIRFM offered the opportunity to investigate if dimeric, tetrameric or oligomeric structures of endogenous GPCR CRF_1R could be found. This question is inaccessible by FCCS.

The 488 nm laser of the laser combiner was set to a power resulting in an average laser intensity at the sample plane of 8 $\mu W/\mu m^2$. It is important to have this defined laser power density to see single molecule bleaching steps, as shown by others [59, 27, 74]. The used filters were the Di01-405/488/561/635 in the filter cube of the turret, emission filter BL HC 525/45 in the filter wheel in front of the OptoSplit. No cube or filter was introduced to the OptoSplit so that the emission light was imaged completely on the transmission side of the OptoSplit (see figure 5.2). The EMCCD was running at 20 ms frame rate and a gain of 120 to 300. TIRF was established by moving the laser focus from the center of the BFP to the edge (translation of L3, see section 5.1.1). The analysis of the acquired data was done using GMimPro [98], which is a single molecule tracking software. To calibrate the setup, the intensity of immobilized yellow fluorescent proteins (YFP) were analyzed and single-step photo-bleaching could be observed. Those single-step photo-bleaching events were a direct measure for the intensity of a single YFP. Following this calibration experiment was the acquisition of transiently transfected HEK 293 cells expressing the GPCR CRF_1R YFP where single molecule detection at the basal plasma membrane was performed and the intensities of different fluorescent spots were analyzed. Discrete steps in intensity loss, indicating bleaching events of tracked fluorescent spots were observed. Teichmann et al. [139] were able to show for the first time, that the GPCR CRF_1R is partly dimerized at the plasma membrane, using the SD-*d*STORM setup as a smTIRFM. The results from this analysis are shown in figure 6.5 on the facing page.

The preparation of the cells and mounting in a live-cell dish was carried out by Anke Teichmann. The laser-power calibration and imaging was done by the author of this thesis. Analysis of the acquired data and measurements were achieved in close collaboration with Anke Teichmann.

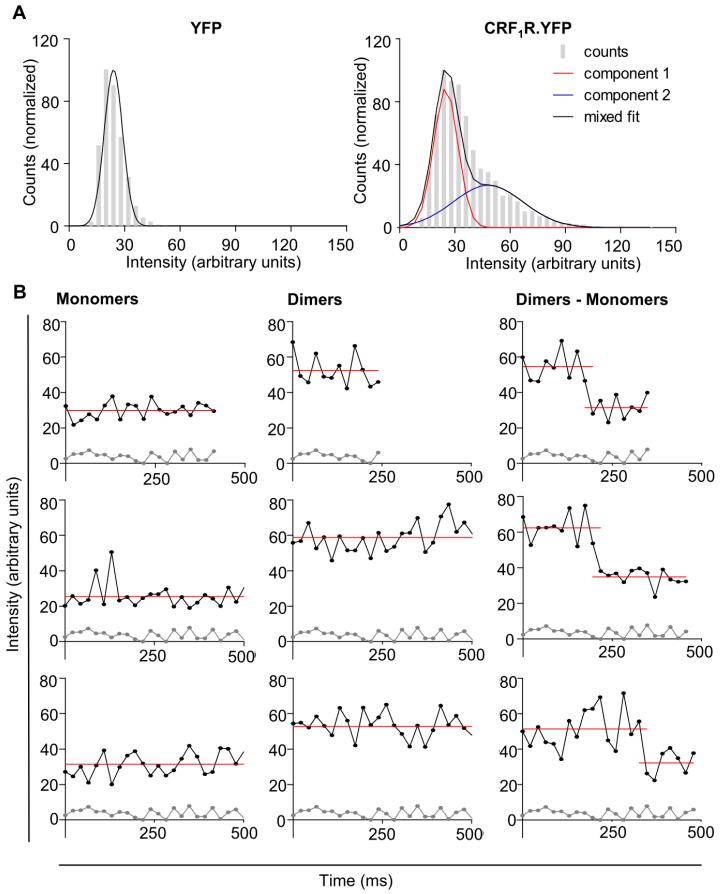

Figure 6.5.: Detection of $CRF_1R.YFP$ dimers in the plasma membrane of transiently transfected HEK 293 cells using smTIRFM. (A) Left: Normalized intensity distribution histogram of purified YFP immobilized by a monoclonal GFP/YFP antibody on a poly-L-lysine-coated cover slip. In four independent experiments, 2534 fluorescent YFP spots were detected. Best fitting by a Gaussian function with a mean value of 25 ± 6 a.U. Right: Normalized intensity distribution histogram of $CRF_1R.YFP$. In 4 independent experiments, 7594 fluorescent spots were analyzed (at least 5 cells in each experiment). Best fitting by a 2 Gaussian function. The mean of the first component represents monomeric CRF1R.YFP (25 ± 6 a.U.; red curve), the mean of the second component represents dimeric CRF1R.YFP (50 ± 11 a.U.; black curve). (B) Intensity changes of individual tracks of $CRF_1R.YFP$. Left: Examples for intensity traces of moving fluorescent spots representing monomeric $CRF_1R.YFP$ (upper traces) in comparison to traces resulting from areas containing no fluorescently labeled receptors (lower traces). Middle: As above, but examples for intensity traces representing dimeric $CRF_1R.YFP$ are shown. Right: As above, but examples for intensity traces representing dimeric $CRF_1R.YFP$ are shown which shift abruptly to the level of a single YFP fluorophore, either by photo-bleaching or by dimer dissociation. The red line indicates the mean value of the individual traces. [139]

7. Discussion

In this thesis a variant of a multicolor 3D SMLM approach was built, optimized and applied to address biological questions in the field of membrane traffic. The precise nanoscale localization of different proteins within the cell on a molecular level is of fundamental interest in biology. The presented method of 3D SD-*d*STORM can be used to answer questions including super-resolved co-localization experiments or by measuring cluster sizes of, or distances between proteins (see section 6). Most importantly, this method offers precise multicolor co-localization paired with nanoscale resolution, thus presenting great advantages over electron microscopy (EM). EM with its superior resolution in the single digits nanometer range, offers dual immunogold labeling but only with a low density, which limits dual color approaches severely.

7.1. Advantages and limitations of the SD-*d*STORM platform

Since SD-*d*STORM is part of the SMLM family, all advantages and disadvantages of SMLM apply to it as well. The limitations of current super-resolution approaches have been presented and compared in section 3.5 on page 37. A short summary of the capabilities of SMLM done on a single objective wide-field setup:

- SMLM provides measurements of the position and distances of individual molecules, information that no other fluorescence super-resolution technique can access [93, 28, 19]
- imaging with more than two colors have been proven to work [83, 97, 24, 89]
- lateral resolution in biological samples was achieved down to 20 nm, in special cases down to the single digit nanometer range. [128, 101, 99]
- 3D imaging with a resolution of 50 nm to 70 nm in z-direction, confined to a range of 0.8 µm to 1.4 µm. [15, 19]

- compatible with one or more additional colors, which are not super-resolved [85, 5, 162]

- Live-cell imaging is possible but very limited due to low temporal resolution and compromises in label density [83, 130, 50]

- not only the positions of fluorophores but more information can be gathered from the raw data of SMLM approaches by better and more sophisticated algorithms [34, 141, 125]

- application of high light intensities from 0.5 - 10 kW/cm^2 which can lead to light-induced cell damage and photo-bleaching [109, 156, 151]

- for some dye combinations rather harsh buffer conditions are needed [85, 152, 69]

The SD-*d*STORM approach combines all those advantages. Super-resolving two colors on biological structures is possible (sections 5.2, and 6) with a lateral resolution of 25 nm (section 5.4). SD-*d*STORM is also suitable for the reconstruction of three dimensional structures with a resolution in z-direction of 66 nm in two colors (sections 5.3 and 5.4). The technique is compatible with additional, non-super-resolved colors like Alexa Fluor 488, which was used during the experiments to determine the experimental localization precision and optimally obtainable resolution (section 5.4). Live-cell experiments in combination with super-resolution have never been tried with SD-*d*STORM also the two color approach seems to be impossible with the described buffer conditions because of the high concentration of reducing agent (table 4.3). However, a few dye combinations suggested by Lehmann et al. [89] could allow two color live-cell super-resolution imaging. SD-*d*STORM was used to measure the size of STOML3 clusters and distances between the protein basson and GIT1 puncta (chapter 6). The multi-color approach achieved by spectral demixing is done after the acquisition of the raw data and falls under the category of post-processing. The presented, super-resolved images in this thesis were acquired with laser powers around 5 kW/cm^2 for up to 10 min, which led to photo-bleaching of a bigger part of the dyes in the field of view (section 5.1). The buffer conditions are rather harsh for the two dye pairs presented in this thesis, with 300 mM MEA for Alexa Fluor 647 and 700 and 420 mM β-ME for Alexa Fluor 647 and Dyomics 678. The advantages and limitations of the SD-*d*STORM approach are discussed in detail in the following sections and possible improvements are suggested.

7.1.1. Multicolor with SD-*d*STORM

One major improvement of the spectral demixing approach, not only compared to other SMLMs but to all super-resolution techniques, is the registration and aberration free reconstruction of two colors (section 5.2). This is due to the fact that localizations from both colors are reconstructed from one channel (short-wavelength or long-wavelength, respectively), and the other channel is only required to assign a color to a localization. The trade-off for this advantage is the net loss of localizations for reconstruction. This loss of localizations is not a disadvantage though as all localizations are checked whether they originate from a blinking event of a fluorophore or are contributed by noise. Most SMLM techniques identify localizations just based on an intensity threshold. Spectral demixing with its pair-finding adds a second step to this identification process. Discarded localizations after this second step are rejected if they do not originate from a single blinking event. This approach leads to reduced single molecule localization noise in areas of the cell or in tissue where the noise levels are high, due to off focus light or other means (section 5.2.5).

But not only the noise reduction of SD-*d*STORM is a consequence of this. Co-localization experiments can be carried out with resulting precision down to the optimally obtainable resolution of 25 nm in x/y and 66 nm in z-direction (including drift, section 5.4). Most other techniques acquire multi-color data sequentially and have to rely on error-prone alignment procedures of the different channels [71, 16, 144, 7]. This alignment introduces an error into the data set, which is at least in the order of magnitude of 10 nm, about half the minimal localization precision and has to be taken into account for co-localization experiments. Recently an even higher resolution with two colors was reported using SD-*d*STORM and reductive caging of fluorescent dyes followed by UV-induced recovery. A multicolor localization precision below 15 nm was achieved [88].

The intensity of a single localization in SD-*d*STORM is lower compared to other *d*STORM approaches, since the emission light is split spectrally between two channels. But the optimally obtainable localization precision is hardly affected by this compared to other techniques, showing a localization precisions between 20 nm and 30 nm [57, 107, 128, 63] (section 5.4).

7.1.1.1. More than two colors

From a spectral point of view it seems possible to apply spectral demixing to more than two colors (compare figures 5.5 and 5.4d). For the presented dye pair of Alexa

Fluor 647 and Dyomics 678, the use of a third dye, probably with a longer emission wavelength than the other two, is possible. The carbocyanine Cy7-derived Alexa Fluor 750 is a potential candidate due to its well fitting blinking characteristics [35]. This would require a different dichroic mirror in the OptoSplit II (see table 5.2) and the use of a longer wavelength laser like the 661 nm laser already presented, but probably with higher power output. Also in the green to yellow emission range of the visible spectrum, from 500 nm to 580 nm, some fluorophores exist, which could be suitable even for a triple color SD-*d*STORM, Atto 520, Cy3B and Alexa Fluor 568 for example, described by Lehmann et al. [89] and Dempsey et al. [35]. For the purpose of three colors, two laser lines for the excitation of the used fluorophores could be used, but this would require a more sophisticated blocking filter in the filter wheel in front of the OptoSplit II. For optimal performance such a filter should have two small bands to only block the two used laser lines. Such filters (Multi-Notch-Filters) are not available for every combination of laser lines or do not possess the necessary optical density to efficiently block lasers with powers above 100 mW. Another approach to introduce a third color would be the overlay of a single color and a two color spectral demixing measurement using registration [89]. This would lead to registration errors and some drawbacks already described in section 3.4.1, but could still be advantageous, since reliable co-localization in three colors is seldom needed.

In any case, a third and fourth non super-resolved color could always be used in SD-*d*STORM, acquired in normal wide-field mode. Co-staining with Alexa 488 was done to measure the optimally obtainable resolution (section 5.4) but every fluorophore excitable with the 405 nm, 488 nm and 568 nm laser line of the setup can potentially be used. The dichroic used in the turret underneath the objective is capable of reflecting all of those into the sample, providing transmission windows for the emission of said fluorophores at the same time (table 5.2).

7.1.2. Fluorescent dyes, buffers and labeling density

As pointed out in the introduction about fluorescent ligands (section 3.1.4) there is a vast variety of fluorescent probes available that have to be optimized in regard to the sample, the available light sources and imaging modes. The selectable set of fluorescent probes gets even more restricted when any super-resolution technique is used. The least restrictive approach in terms of choice of fluorophores would be SIM, but constraints to photon-yield and photostability of the used fluorophores get narrow even in SIM, that uses regular dyes [55, 126]. For SMLM approaches the blinking characteristics of the fluorescent ligand have to be suited for the technique, which narrows the choice

of fluorophores even further [35, 141, 70]. For multicolor SD-*d*STORM the choice is restricted to the two dye pairs presented in this thesis (Alexa Fluor 647/Dyomics 678 and Alexa Fluor 647/Alexa Fluor 700) and to those discussed and demonstrated by Lehmann et al. [89]. The dye pairs Alexa Fluor 647/Dyomics 678 and Alexa Fluor 647/Alexa Fluor 700 emitting in the far-red part of the visible spectrum and will not interfere with most standard probes emitting in other parts of the spectrum.

The demand for a high reducing potential in the imaging buffer constitutes a major limitation for live-cell imaging. For the pair of Alexa Fluor 647 and Alexa Fluor 700 300 mM MEA [85] has to be present in the buffer during acquisition, for Alexa Fluor 647 and Dyomics 678 420 mM β-ME [86]. However, there are alternative dye pairs for the spectral demixing approach described by Lehmann et al. [89] with a lower concentration of the reducing agent, down to 10 mM MEA.

None of those two pairs presented in this thesis could be used in live-cell experiments, since the reducing potential of the cytosol is only in the range of 10 mM MEA [142]. Also for thick tissue samples or embedded samples this poses a problem, since the concentration of the reducing agent could be lowered locally due to low diffusion in the sample.

7.1.2.1. Different labeling strategies

In this work mainly primary and secondary antibodies were used for immunolabeling. Since most investigated structures in this thesis, like the STOMAL3 clusters or the clathrin coated pits (chapter 6) were confined to two dimensions or shaped convexly, the labeling density to resolve these structures was achieved. As already mentioned in the section about labeling density and the Nyquist-criterion (section 3.3): to achieve a resolution of 20 nm at least a fluorescent probe every 10 nm in every dimension the structure extends is needed. This could present difficulties when the protein of interest is e.g. located on the inside of a CCP, since it would be a restriction to a concave surface and narrow the number of binding antibodies. A higher labeling density of a biological structure could be achieved with the use of antibodies derived from llamas, camels or sharks, so called nanobodies [71]. In contrast to antibodies from mice, rat, rabbit and others, which consist of two Fab segments and one Fc segment, nanobodies are only one tenth of the size of an antibody, in structure comparable with a single-chain variable fragment (scFv). A comparison of the different structures and the respective weights is shown in figure 7.1 on the following page. Nanobodies have been used successfully in different super-resolution applications.

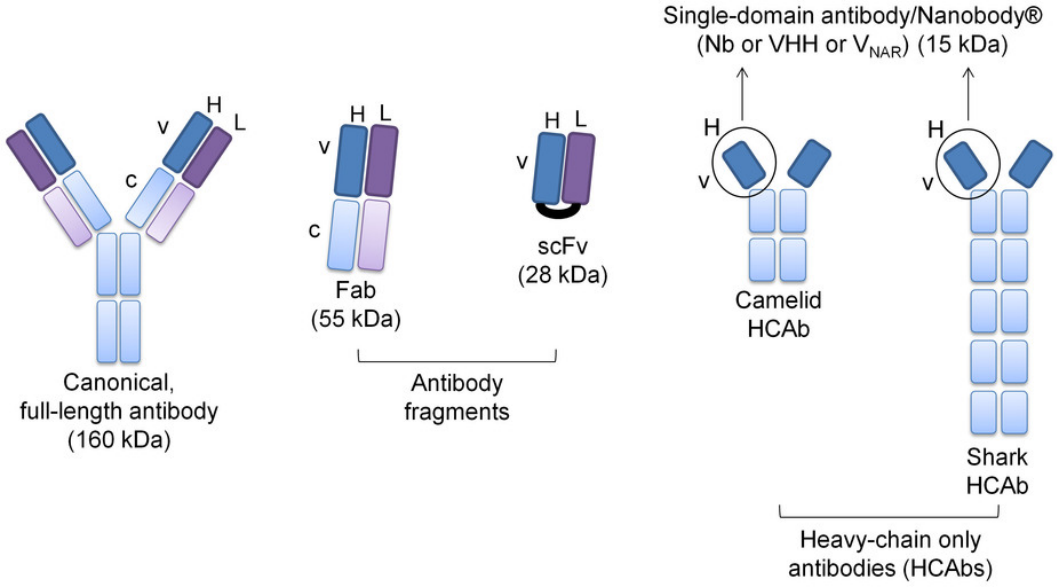

Figure 7.1.: Compared to regular antibodies (160 kDa) and their fragments (fragment antigen-binding, Fab - 65 kDa; single-chain variable fragment, scFv - 28 kDa), the molecular size of single-domain Nanobodies is the smallest (15 kDa). Nanobodies can be derived from the heavy-chain only antibodies that occur naturally in camelids and sharks (modified from [124]).

7.1.3. Three dimensions

There are different ways to achieve three dimensional imaging with SMLM (section 3.4.2). Common examples are biplane and distortion of the PSF of a localization. The biplane approach will be compared to the approach presented in this thesis in section 7.1.3.2, since it is fundamentally different from astigmatism. Determining z-positions from distorted PSFs can be done in different ways [118]. The most complicated approach would be the double-helix PSF approach, where the point spread function of a localization is shaped to two dots. The z-position is encoded in the angle of an imaginary line passing through those two dots. The name double-helix PSF originates from the appearance of a 3D representation of this, since the two dots rotate around a common center when many images of different z-positions are stacked on top of each other [114]. This technique demands a custom detection path in the microscope and, far more important, a specialized quantification software. Another approach is phase ramp imaging localization microscopy (PRILM). Here the PSF is split into two lobes, encoding the position in z-direction [12]. The latter is comparable to the astigmatism approach, which introduces a cylindrical lens into the detection light-path (figure 5.12) as used in the 3D experi-

ments presented in this thesis. Astigmatism was first introduced to SMLM by Huang et al. in 2008 [20, 19] and integration of a cylindrical lens presented the least modification to a SMLM setup. Because of this others adapted this approach on the setup side as well as on the software side [122, 125] (section 7.1.4). Not only the easy integration in the SD-*d*STORM setup of a cylindrical lens and the multitude of software capable of handling astigmatism was the reason for the choice of that approach, also the quantity of literature played a role [61, 15, 108]. There are already astigmatism approaches with improved range and resolution in z, but this often calls for more complicated setups like a second objective and detection path from the other side, and is impossible to implement into the presented SD-*d*STORM setup without a complete rework [93].

Any 3D approach in SMLM suffers from the problem of distributed localizations. In the 2D case all localizations contribute to the reconstruction of one image. In 3D localizations are distributed to different image planes. For a range of 800 nm in z, this results in 32 image planes with a distance of 25 nm (section 5.3). Indeed, the depth of sharpness of an objective is improved by the cylindrical lens and more localizations can be detected compared to the 2D case, but the increase is in the range of three- to eight-fold and not 32-fold. For 3D SD-*d*STORM a longer acquisition time would be indicated and further optimization of all components of the microscope and the used probes and labeling strategies.

Taken together with all other remarks from this section, the 3D SD-*d*STORM is probably best used on fixed cells or thin tissue samples, where at high background fluorescence or three dimensional, extended structures with a high labeling density pose no complication. The optimal obtainable localization precision of 25 nm in x/y and 67 nm in z for Alexa Fluor 647 and 26 nm in x/y and 66 nm in z for Dyomics 678 is comparable to localization precisions of other SMLM approaches (section 3.5). However, it outperforms the resolution achievable with SIM or STED in x/y and z [110, 147, 121]. The range of 3D SD-*d*STORM in z is restricted to about 1 µm and, by this, only inferior to SIM, which is capable of imaging volumes tenth of micrometers deep [126].

7.1.3.1. Thermal stability

As indicated in section 5.3.2, heating of the sample induced by illumination with the laser during the measurement was not investigated. It was discussed that a temperature change of only 2 °C would void the 3D calibration due to heat-difference induced changes in the optical components. Therefore at least for 3D SD-*d*STORM, a temperature stabilization is mandatory. But so far the stabilization is only done by controlling the room temperature and adjusting the temperature inside the enclosure carefully by a feedback

loop of temperature measurements during acquisition and subsequent heating. Illumination of the sample with high laser intensities in the order of 2 to 5 kW/cm^2 could lead to a temperature gradient in the sample as well as the objective. If precise measurements of the temperature of the sample and the objective would be accessible, a potential source of distortions in the optics could be ruled out. Alternatively, a way to correct for this in the post-processing of the data is possible, which could be a potential improvement of the experimental localization precision and optimally obtainable resolution in 2D and 3D.

7.1.3.2. Biplane vs. astigmatism

The range in z-direction of 3D SD-*d*STORM is restricted to about 1 µm per measurement due to astigmatism. The cylindrical lens distorting the image of localizations with respect to their z-position is limited by the depth of sharpness of the used objective. Biplane has the potential to extend the range in z-direction, since this approach is not so strictly limited by the depth of sharpness of the objective.

SD-*d*STORM needs a setup where the field of view is imaged twice, just spectrally separated with the dichroic mirror used in the OptoSplit II. The prerequisites for 3D with biplane are already fulfilled. However, an introduction of an off-set in z-direction between the focal plane of the short-λ-channel and the long-λ-channel in the SD-*d*STORM setup for 3D imaging using the biplane approach would make a complete rework of the SDmixer software necessary. The localization software rapi*d*STORM is not capable of deriving z-coordinates from biplane, so a different localization software would be needed. This presents only a minor problem, since the SDmixer software was designed to handle all kinds of raw text coordinate data, but the coordinate sets generated by biplane would differ fundamentally from those coordinates generated by astigmatism. While the latter would only change the shape of a localization event with respect to its z-position, biplane computes z-positions not only from differences between its two channels. Also it can construct a position in z from a localization in one channel, treating an empty channel as a localization too far away from the focal plane of that channel. It is not clear if the pair-finding approach of spectral demixing would work as well with 3D data generated by biplane, due to the off-set in z-direction between short- and long-λ-channel. First of all it is not clear if this would have an influence on the x/y precision of finding pairs. Second, there would be more localizations without a partner, when a localization is found at the edge of the z-range, leading to only one localization in one of the channels, since the image in the other channel is too far out of focus. Third, the off-set would be hard to control in the present setup using an OptoSplit II, just because the product is not

designed to introduce a certain off-set but comes only with some lenses to correct for an off-set.

Considering all those differences and complications, it would still be worth a try using biplane with the SD-*d*STORM approach. Getting rid of the cylindrical lens and replacing this optical element by another lens just in the light-path of one of the spectral demixing channels, might increase the signal to noise ratio in the spectral demixing channel without the off-set lens. With biplane, there would also be the possibility that, the 3D calibration becomes more robust compared to astigmatism, since the cylindrical lens is very sensitive to temperature changes, but this is a speculation. If this indeed were the case, the issues of drift discussed in section 5.1.2 and of temperature stability described in section 5.3.2 would have to be approached differently and could possibly turn out less complicated from a user point of view. Also the range of biplane in z-direction accessible to localization detection could be larger compared to astigmatism [96, 118].

7.1.4. Data analysis

The concept of image reconstruction from single molecule localization data is rather young. But there are already many different software packages, developed by scientist from the super-resolution field, that can analyze single molecule blinking image series and reconstruct super-resolved images. The École Polytechnique Fédérale de Lausanne (EPFL) runs a permanent project called "Benchmarking of Single-Molecule Localization Microscopy Software", that compares dozens of different localization software [125]. The major advantage of SMLM is the fact that already existing data sets can be re-analyzed using new algorithms, and even more advanced analysis tools like SDmixer presented in this thesis can be employed in the reconstruction process. The SDmixer software was designed with the capability of reading and processing different input data formats and is compatible with a multitude of localization software packages [138].

3D SD-*d*STORM does not provide a super-resolved reconstruction directly after the acquisition and should not be used on an unknown sample anyhow, but on a sample with known structure and with knowledge of the performance of the used primary antibodies. Immediate reconstruction of the image is not essential. The fact that an image is always generated in a post-processing step offers the opportunity to employ statistical tools to analyze the raw data for more than just spatial information to reconstruct an image. 3D SD-*d*STORM is a good example for exactly that, since the color assignment is done by analyzing the localizations with respect to a specific rule and parameter set prior to reconstruction [138, 86]. Since computers become more and more powerful, the opportunity arises to do post-processing even to a greater extend and gather additional

information about the sample beyond the spatial coordinates necessary to reconstruct an image. As already mentioned in section 3.5, the apparent disadvantage of post-processing of SMLM approaches like SD-*d*STORM might become an advantage in the long run.

7.1.5. A comparison to electron microscopy

Electron microscopy (EM) is the gold standard with its resolution in the single digits nanometer range. However, electron microscopy lacks specificity for single protein species, despite its superior resolution power compared to super-resolution light microscopy. Staining for specific proteins in EM is done with immunogold, beads of gold variable in size [123]. But to distinguish them from tissue structure, their size has to be in the nanometer range. In addition to this, the standard staining strategy involves the use of primary and secondary antibodies comparable to light microscopy. This leads to a distance of about 15-30 nm of an individual gold bead to the structure it should label, the same problem light microscopy has to deal with. But in contrast to light microscopy, the more complex preparation protocols for EM causes a lower labeling density of the target protein [119]. Different labeling strategies (see 7.1.2.1) would not overcome this easily for EM as they might for super-resolution light microscopy approaches.

A combination of the *d*STORM technique and electron microscopy has been shown but the registration error between the images of the different techniques are still in the range of 50 nm [131]. This correlative imaging approach, when developed further with lower error margins in registration, has the potential to combine the high resolution structure determination capability of electron microscopy with the possibility of labeling a certain protein very specificly. With the accuracy of multicolor registration of SD-*d*STORM (see section 5.2.3 and figure 5.8), further development to more than one color would be possible.

7.2. Advantages of using SD-*d*STORM in cell biology

In chapter 6 four application examples for the setup were introduced, of which three questions addressed the resolution beyond the diffraction barrier of microscopes using the SD-*d*STORM approach.

7.2.1. Membrane cell biology

The spatial relation between scaffolding protein GIT1 and a giant multidomain protein of the CAZ bassoon in the presynapse was investigated using SD-*d*STORM in the study

presented by Podufall et al. [117] (section 6.1). Measuring distances between two proteins stained with two colors is always a problem in super-resolution approaches. SD-*d*STORM with its aberration free and two color capabilities without registration errors was a perfect fit for the distance estimation between GIT1 and bassoon. SMLM experiments have been carried out with other proteins at the active zone. Distances between bassoon and the AZ protein RIM1 and between bassoon and the postsynaptic protein Homer1 were determined by using STORM [2].

How the presence of the GTPase dynamin2 influences the growth of sortin nexin 9 (SNX9) tubules from clathrin coated pits could also be answered using SD-*d*STORM. The study by Posor et al. [165] investigated, besides other important topics, also the recruitment of different proteins to clathrin coated pit prior to fission (figure 6.2). Two color SD-*d*STORM reconstructions revealed the formation of SNX9 tubules attached to a CCP, with an enhanced growth when dynamin2 was depleted. Clathrin coated pits and vesicles are an excellent target for SMLM approaches because of their size of about 150 nm [97]. Their dimensions are below the diffraction barrier, but substantially larger than the optimally obtainable resolution of SMLM techniques. The shape of CCPs is also advantageous when imaged in SMLM, since the convex shape offers enough room on the surface to reach a sufficient labeling density using primary and secondary antibodies (section 3.3).

7.2.2. Further biological targets

Suited biological targets for 3D SD-*d*STORM can be found by just looking at sizes and distances. Every biological structure with at least one dimension below the diffraction barrier (section 3.1.1 and equation 3.2) but above the optimally obtainable resolution of the described technique (section 5.4) would be a potential target for three dimensional multicolor SD-*d*STORM. An example for structures with sizes below the diffraction barrier in two dimensions are microtubles, super-resolved with 3D SD-*d*STORM and shown in figure 5.15. Also actin filaments, intermediate filaments as well as tubular structures attached to clathrin coated pits in dynamin2 depleted cells (figure 6.3), are suitable targets with two dimensions below the diffraction barrier but in the order of magnitude of the optimally obtainable resolution of 3D SD-*d*STORM. Besides SNX9, an example discussed in section 6.2, intermediate filaments could be a worthwhile target, since they are comprised of up to 60 different building blocks [60]. Their underlying sub-structure could be accessible by 3D SD-*d*STORM, even in thicker parts of the cell, because of the noise-reduction potential discussed in section 5.2.5. In many cases the thickest part of the cell is in proximity to the nucleus containing the cells DNA. While the diameter of

DNA is below the resolution limit of every light microscopy technique, its filamentous structure in correlation to proteins of interest of the epigenetic field or the research on DNA regulation in general could be an application area for 3D SD-*d*STORM.

Another example, with a size below the diffraction barrier in all three dimensions, are vesicles, shown in a 3D reconstruction in figure 5.14. With a size close to the diffraction barrier, structures inside or on the surface of vesicles could be investigated with 3D SD-*d*STORM. Similar targets like the HIV or other viruses were successfully imaged using SMLM techniques [28, 103]. Even structures surrounding the T-bar in active zones of Drosophila's synapses comprised of the protein bruchpilot have been imaged using *d*STORM [39], showing the potential for a vast variety of applications also for 3D SD-*d*STORM in the widely observed field of molecular neuroscience.

The 2014 published work of Lorenzo et al. [93] investigated long-range transport of organelles required for axon growth. They identified a new pathway based on the class PI3-kinase (PIK3C3), ankyrin-B (AnkB), and dynactin, which promotes fast axonal transport of synaptic vesicles, mitochondria, endosomes, and lysosomes. A cornerstone of the study was the use of 3D-STORM, which revealed that the organization of spectrin–actin axonal rings in AnkB knockout neurons was not affected. Another publication from 2014 by Zhong et al. [166] investigated the periodic sub-membrane lattice structure in axons, comprised of actin, spectrin and associated molecules using 3D-STORM. The study included 3D super-resolution imaging of the early stages of axon development, of the propagation of the early formed structures during maturation and of overexpression and knockout experiments in matured neuronal cells. Both studies are good examples for STORM-based use of super-resolution imaging techniques in a biological context.

With the noise-reduction of SD-*d*STORM (section 5.2.5) biological targets in tissue sections could be more easily accessible. Every variant of super-resolution approaches has been proven to work in tissue samples, may it be structured illumination microscopy (SIM) [126], the STED technique [148] or *d*STORM [107]. But all of them have to deal with high photo-toxicity, especially *d*STORM and STED [156], due to the high laser powers needed for those techniques (section 3.5). The noise-reduction of SD-*d*STORM could lower illumination times or even excitation powers, since the second level of noise-reduction by pair-finding is not solely relying on a high threshold for the reconstruction of a super-resolved image, as shown in figure 5.11. Lower laser powers and lower acquisition times would reduce the photo-toxicity while other parameters of SD-*d*STORM, like the optimal obtainable resolution, would persist unchanged. This advantage is a direct consequence of sophisticated post-processing analysis of the raw data, mentioned at the end of section 3.5.

7.3. Further optimization of SD-*d*STORM

7.3.1. Camera

An improved camera for detection of single-molecule signals could be included into the SD-*d*STORM setup, for example an EMCCD camera with a bigger chip than 512 x 512 px as used in the described setup. Those cameras are available (e.g. Andor iXon Ultra 888) with a higher sensitivity in the spectral range above 800 nm and with a higher frame rate, which are both beneficial for SD-*d*STORM. It would also allow the use of fluorophores emitting at longer wavelengths beyond 750 nm, which would have suited blinking characteristics for the spectral demixing approach. A shift to longer wavelengths would also be very advantageous for the use of D_2O imaging buffer, since the effect of a higher quantum yield increases with the wavelength (sec. 5.2.2). Furthermore, a high sensitivity sCMOS (scientific Complementary Metal-Oxide-Semiconductor, e.g. Andor Neo 5.5 sCMOS) camera could be tried with an even larger field of view and a higher frame rate. A sCMOS camera would pose other problems, but first results using this kind of camera and *d*STORM have been documented by Huang et al. [63]. In all cases the use of a more powerful laser, to reach the necessary power density of a larger field of view, is important (see next section).

7.3.2. Higher laser powers

In the case of Alexa Fluor 700 it would be very useful to have higher laser powers for the initial illumination to push the fluorophores in the OFF state. While the buffer condition for decent blinking for both, Alexa Fluor 647 and Alexa Fluor 700 were in a rather big range of concentration of the reducing agent, for most concentrations the initial illumination took several minutes to push Alexa Fluor 700 into the OFF state, while Alexa Fluor 647 already showed descent blinking after a few seconds. Initial illumination could be shortened by a higher concentration of the reducing agent, which was a trade-off, since the intensities of both fluorophores were reduced using this buffer condition. A higher laser power for the initial illumination would most certainly allow a lower concentration of the reduction agent. Commercial laser diodes, while expensive, are already available in the 640 nm range with powers up to 300 mW, which would be double the power available in the SD-*d*STORM setup (sec. 5.1.1). This would also be beneficial to acquire localization data from a larger field of view, since the power-density needed for the photochemical induced blinking of the fluorophores with the SD-*d*STORM approach could be matched for a larger area with a more powerful laser. This is also true for different fluorophores suited for SD-*d*STORM described in detail by Lehmann et al.

[89].

7.3.3. Automated color filters and time analysis

The multicolor assignment procedure was performed based on intensity (figure 5.5 and figure 5.4d). Each fluorophore shows distinct pattern of intensity in the two-dimensional histogram. Thus, it would be possible to improve the procedure by writing a pattern recognition algorithm. Such a an algorithm can replace the single-color experiments and filter designing beforehand. This would result in a more streamlined workflow, since no single color experiments for each used dye would be needed to create the filters for spectral demixing. However, in this case the fraction of false color-assigned localizations would have to be measured in a different way.

A similar improvement to the SDmixer software is the addition of an output function, which analyzes the development of intensities over time. In the presented form SDmixer processes all localization without the context when a localization was recorded. It was shown that the average intensity of fluorophores decreases [57] as well as the number of found localizations over time. An automated feedback in SDmixer could inform about those two parameters, which are not easy accessible. This could help with decisions about the used excitation laser power, buffer composition and the power and frequency of the secondary laser, stimulating the return from the OFF state of fluorophores. It could even be useful to decide whether the number of acquired images is too big or too little, from a number of localization per time interval point of view.

7.3.4. Multi-candidate pairs

As mentioned in section 5.2.1, the pair-finding algorithm sometimes finds more than one localization candidate to form a pair with the localization that originated from the vector for searching a partner (i.e. two or more localization within the search radius at the end of the off-set vector). Assuming that there are only three localizations involved, one on the short-wavelength-side, and two localization candidates on the long-wavelength side. If the intensities of the two candidates do not differ from each other in that way, that both would lead to the same color assignment if paired with the localization in the short-wavelength-channel, then no false-color assignment would occur. Or rephrased as an analysis question: Would pairing of the two candidates lead to the same color assignment? However, in the presented algorithm those three localizations would be discarded from the data set, since the criterion applied allows that only one candidate for pairing. This is due to the nature of the procedural approach we chose to write the

software. The pair-finding procedure is run before the module making the color decision. This could be altered so that also localization pairs with more then one candidate could be considered for the final data that is reconstructed. Since in our experiments no data set exceeded more than 0.01 % of multi-candidate pairs, this seems marginal, but could be more important when investigating the possibility of demixing three or more colors in the described way or changing to a different fluorescent dye pair [89].

8. Conclusion and outlook

Taken together, in this thesis the hard- and software, as well as the underlying principles of the 3D SD-*d*STORM setup were described. Furthermore, the capabilities and performance levels of the setup were investigated (e. g. sample drift in section 5.1.2) and the general concepts of the software SDmixer for spectral demixing were discussed. We could show that two spectrally overlapping organic dyes can be separated as presented in a two dimensional intensity histogram. Using this approach, robust co-localization studies with a resolution of around 25 nm are possible, compared to about 200 nm with standard imaging techniques such as confocal microscopy. This co-localization precision can be achieved without an error-prone channel registration process and the rate of false color assignment is adjustable. These last two points are a big advantage of the presented approach, which is also recognized by others in the field [70, 34, 99, 141]. The work of Klehs et al. on the effects of heavy water in the imaging buffer [82] were shown to be also beneficial to 3D SD-*d*STORM. The presented buffer conditions for the pairs of Alexa Fluor 647 and Alexa Fluor 700 as well as Alexa Fluor 647 and Dyomics 678, stating conditions for those dye pairs to show blinking simultaneously suitable for *d*STORM contributed to the scientific discussion about buffer conditions in general [69, 108, 152]. In addition to this, the noise-reduction of SD-*d*STORM was demonstrated, making regions of cells and tissue more easily accessible to super-resolution microscopy. Since the early variant of SD-*d*STORM [85] we were aware that this technique is suited for 3D localization-based super-resolution microscopy [15], and we could show the three dimensional multicolor potential of SD-*d*STORM [86, 138] later on. Possible extensions and further development of the presented approach, e.g. different labeling strategies, higher laser powers or the use of more than two colors were discussed in sections 7.1 and 7.3.

The technique was applied to resolve nanoscale details in cellular samples stained for targets in the membrane trafficking machinery (section 6). The versatility of the setup was shown using it as a smTIRFM in the work of Teichmann et al. on GPCRs [139]. The potential to investigate structures below the diffraction barrier of microscopes was exhibited on the clustering of STOML3 in sensory neurons (paper under review, see appendix A), the spatial correlation of GIT1 to bassoon in the synapse [117] and by

visualizing the SNX9 tubular structure attached to clathrin coated pits in dynamin2 depleted cells [165]. Further biological targets are discussed (section 7.2). However, the presented approach is not multipurpose and belonging to the SMLM technique-family certain limitations apply. Photo-sensitive live-samples are not suited for the approach, as well as thick specimen of tissue as these impose difficulties in acquisition.

No super-resolution technique is a multipurpose approach to research questions in the field of life sciences. The SMLM techniques, however, possesses the potential to become something like the gold-standard for investigations below the diffraction limit. Due to SMLMs modular character, these approaches benefit the most from new developments like fast, high-sensitive sCMOS cameras or advances in laser technology. There is no restriction to do PALM or uPAINT on the described 3D SD-*d*STORM setup in this thesis, since the main difference is the sample preparation and rather independent of the setup itself. Furthermore, the need for post-processing in every SMLM approach has become a fundamental starting-point for advanced analysis, like the presented software SDmixer and could lead to a versatile set of SMLM approaches with reciprocal advantages and draw-backs.

In conclusion, 3D SD-*d*STORM provides a way of performing multicolor SMLM derived from a single measurement of a sample excited with one laser line. The approach is robust and accurate especially for co-localization with the potential to bridge the gap from light microscopy to EM.

List of Figures

List of Tables

Nomenclature

ADHD	Attention-deficit hyperactivity disorder
ANSOM	Aperture free near-field scanning optical microscope
AOTF	Acoustic-optical tunable filter
APD	Avalanche photo diode
Arf6	ADP ribosylation factor 6
AZs	Active zones
Bass	Bassoon
BFP	Back focal plane
BSA	Bovine serum albumin
CAZ	Cytomatrix of the active zone
CCP	Clathrin coated pit
Dk	Donkey
DMEM	Dulbecco's modified Eagle's medium
DOL	Degree of labeling
dSTORM	Direct stochastic optical reconstruction microscopy
EM	Electron microscopy
EMCCD	Electron multiplying charged-coupled device
EPR	Electron paramagnetic resonance
FCCS	Fluorescence cross-correlation spectroscopy

FOV	Field of view
FWHM	Full width half maximum
GIT	G protein coupled receptor kinase 2 interacting protein
GPCRs	G protein-coupled receptors
GSDB	Goat serum dilution buffer
GSDIM	ground state depletion microscopy followed by individual molecule return
LZW	Lempel-Ziv-Welch
M	Mouse
NA	Numerical aperture
NORM	Near-field optical random mapping microscopy
NSOM	Near-field scanning optical microscope
OD	Optical density
OTF	Optical transfer function
PALM	Photo-activated localization microscopy
PBS	Phosphate-buffered saline
PFA	Paraformaldehyde
PLL	Poly-L-lysine
PRILM	Phase ramp imaging localization microscopy
PSF	Point spread function
Rb	Rabbit
sCMOS	Scientific Complementary Metal-Oxide-Semiconductor
SD-dSTORM	Spectral demixing direct stochastic optical reconstruction microscopy
SIM	Structured-illumination microscopy
SMLM	Single molecule localization-based super-resolution microscopy

SNX9	Sorting Nexin 9
SOFI	Super-resolution optical fluctuation imaging
STED	Stimulated emission depletion
STOML3	Stomatin-like protein 3
STORM	Stochastic optical reconstruction microscopy
SVs	Synaptic vesicles
TIFF	Tagged image file format
TIRFM	Total internal reflection fluorescence microscope
uPAINT	Universal point accumulation for imaging in nanoscale topography
YFP	Yellow fluorescent protein

Bibliography

[1] Ernst Abbe. Beitraege zur theorie des mikroskops und der mikroskopischen wahrnehmung. *Archiv fuer Mikroskopische Anatomie*, 9:413–418, 1873.

[2] Joseph Bergan Cathrine Dulac Xiaowei Zhuang Adish Dani, Bo Huang. Superresolution imaging of chemical synapses in the brain. *Neuron*, 68:843–856, 2010.

[3] G. B. Airy. On the diffraction of an object-glass with circular aperture. *Transactions of the Cambridge Philosophical Society*, 5:283–291, 1835.

[4] Michael D. Allen, Susanne Neumann, and Marvin C. Gershengorn. Occupancy of both sites on the thyrotropin (tsh) receptor dimer is necessary for phosphoinositide signaling. *The FASEB Journal*, 25(10):3687–3694, 2011.

[5] Pedro Almada, Sian Culley, and Ricardo Henriques. Palm and storm: Into large fields and high-throughput microscopy with scmos detectors. *Methods*, 88:109–121, 2015. Super-resolution Light Microscopy.

[6] E. J. Ambrose. A surface contact microscope for the study of cell movements. *Nature*, 178, 1956.

[7] Marie-Christine Dabauvalle Bernd Rieger Mike Heilemann-Georg Krohne Anna Loeschberger, Sebastian van de Linde and Markus Sauer. Super-resolution imaging visualizes the eightfold symmetry of gp210 proteins around the nuclear pore complex and resolves the central channel with nanometer resolution. *J Cell Sci*, 125:570–575, 2012.

[8] Paolo Annibale, Stefano Vanni, Marco Scarselli, Ursula Rothlisberger, and Aleksandra Radenovic. Quantitative photo activated localization microscopy: Unraveling the effects of photoblinking. *PLoS ONE*, 6(7):e22678, 07 2011.

[9] Nenad Amodaj Henry Pinkard Ronald D. Vale Arthur D. Edelstein, Mark A. Tsuchida and Nico Stuurman. Advanced methods of microscope control using micromanager software. *Journal of Biological Methods*, 1(2), 2014.

[10] P.W. Atkins, editor. *Quanta: A handbook of concepts.* Oxford University Press, 1974.

[11] D Axelrod. Cell-substrate contacts illuminated by total internal reflection fluorescence. *The Journal of Cell Biology*, 89(1):141–145, 1981.

[12] David Baddeley, MarkB. Cannell, and Christian Soeller. Three-dimensional sub-100 nm super-resolution imaging of biological samples using a phase ramp in the objective pupil. *Nano Research*, 4(6):589–598, 2011.

[13] David Baddeley, David Crossman, Sabrina Rossberger, Juliette E. Cheyne, Johanna M. Montgomery, Isuru D. Jayasinghe, Christoph Cremer, Mark B. Cannell, and Christian Soeller. 4d super-resolution microscopy with conventional fluorophores and single wavelength excitation in optically thick cells and tissues. *PLoS ONE*, 6(5):e20645, 05 2011.

[14] Margaret E. Baron. *The origins of the infinitesimal calculus.* Dover Publ., 2003. ISBN 0-486-49544-2.

[15] Ignacio Izeddin Xavier Darzacq Bassam Hajj, Mohamed El Beheiry and Maxime Dahan. Accessing the third dimension in localization-based super-resolution microscopy. *Phys. Chem. Chem. Phys.*, 16, 2014.

[16] Mark Bates, Graham T. Dempsey, Kok Hao Chen, and Xiaowei Zhuang. Multicolor super-resolution fluorescence imaging via multi-parameter fluorophore detection. *ChemPhysChem*, 13(1):99–107, 2012.

[17] Jose S. Santos Ruhma Syeda Joerg Grandl Kathryn S. Spencer Sung Eun Kim Manuela Schmidt Jayanti Mathur Adrienne E. Dubin Mauricio Montal Bertrand Coste, Bailong Xiao and Ardem Patapoutian. Piezo proteins are pore-forming subunits of mechanically activated channels. *Nature*, 483:176–181, 2012.

[18] E. Betzig. Proposed method for molecular optical imaging. *Opt. Lett.*, 20(3):237–239, Feb 1995.

[19] Boerries Brandenburg & Xiaowei Zhuang Bo Huang, Sara A Jones. Whole-cell 3d storm reveals interactions between cellular structures with nanometer-scale resolution. *Nature Methods*, 5:1047–1052, 2008.

[20] M Bates X Zhuang Bo Huang, W Wang. Three-dimensional super-resolution imaging by stochastic optical reconstruction microscopy. *Science*, 319(5864):810–813, 2008.

[21] Niels Bohr. On the consitution of atoms and molecules, part i. *Philosophical Magazine*, 26:1–24, 1913.

[22] Niels Bohr. On the consitution of atoms and molecules, part ii. *Philosophical Magazine*, 26:476–502, 1913.

[23] M. Born and R. Oppenheimer. Zur quantentheorie der molekeln. *Annalen der Physik*, 389(20):457–484, 1927.

[24] Mariano Bossi, Jonas Foelling, Vladimir N. Belov, Vadim P. Boyarskiy, Rebecca Medda, Alexander Egner, Christian Eggeling, Andreas Schoenle, and Stefan W. Hell. Multicolor far-field fluorescence nanoscopy through isolated detection of distinct molecular species. *Nano Letters*, 8(8):2463–2468, 2008. PMID: 18642961.

[25] Janko Brand, Ewan St J Smith, David Schwefel, Liudmila Lapatsina, Kate Poole, Damir Omerbašić, Alexey Kozlenkov, Joachim Behlke, Gary R Lewin, and Oliver Daumke. A stomatin dimer modulates the activity of acid-sensing ion channels. *The EMBO Journal*, 31(17):3635–3646, 2012.

[26] D. Lansing Taylor & Frederick Lanni Brent Bailey, Daniel L. Farkas. Enhancement of axial resolution in fluorescence microscopy by standing-wave excitation. *Nature*, 366:44–48, 1993.

[27] Davide Calebiro, Finn Rieken, Julia Wagner, Titiwat Sungkaworn, Ulrike Zabel, Alfio Borzi, Emanuele Cocucci, Alexander Zuern, and Martin J. Lohse. Single-molecule analysis of fluorescently labeled g-protein-coupled receptors reveals complexes with distinct dynamics and organization. *Proceedings of the National Academy of Sciences*, 110(2):743–748, 2013.

[28] Dylan M Owen Johnson Mak Candida F Pereira, Jeremie Rossy and Katharina Gaus. Hiv taken by storm: Super-resolution fluorescence microscopy of a viral infection. *Virol. J.*, 9, 2012.

[29] Dieter Riethmacher Anne Benckendorff Lena Harder Andreas Eilers Rabih Moshourab Alexey Kozlenkov Dominika Labuz Ombretta Caspani Bettina Erdmann Halina Machelska Paul A. Heppenstall Christiane Wetzel, Jing Hu and Gary R. Lewin. A stomatin-domain protein essential for touch sensation in the mouse. *Nature*, 445:206–209, 2006.

[30] Audrey Claing, Stephen J. Perry, Mircea Achiriloaie, Julia K. L. Walker, Joseph P. Albanesi, Robert J. Lefkowitz, and Richard T. Premont. Multiple endocytic pathways of g protein-coupled receptors delineated by git1 sensitivity. *Proceedings of the National Academy of Sciences*, 97(3):1119–1124, 2000.

[31] Edward Condon. A theory of intensity distribution in band systems. *Phys. Rev.*, 28:1182–1201, Dec 1926.

[32] Bertrand Coste, Jayanti Mathur, Manuela Schmidt, Taryn J. Earley, Sanjeev Ranade, Matt J. Petrus, Adrienne E. Dubin, and Ardem Patapoutian. Piezo1 and piezo2 are essential components of distinct mechanically activated cation channels. *Science*, 330(6000):55–60, 2010.

[33] Peter J. Cullen. Endosomal sorting and signalling: an emerging role for sorting nexins. *Nature Reviews Molecular Cell Biology*, 9:574–582, 2008.

[34] Matthew T Parent Dahan Kim, Nikki M Curthoys and Samuel T Hess. Bleed-through correction for rendering and correlation analysis in multi-colour localization microscopy. *J. Opt.*, 15, 2013.

[35] Graham T Dempsey, Joshua C Vaughan, Kok Hao Chen, Mark Bates, and Xiaowei Zhuang. Evaluation of fluorophores for optimal performance in localization-based super-resolution imaging. *Nat Meth*, 8(12):1027–1036, December 2011.

[36] Elisa D'Este, Dirk Kamin, Fabian Goettfert, Ahmed El-Hady, and StefanÂ W. Hell. Sted nanoscopy reveals the ubiquity of subcortical cytoskeleton periodicity in living neurons. *Cell Reports*, 10(8):1246–1251.

[37] U. Duerig, D. W. Pohl, and F. Rohner. Near-field optical-scanning microscopy. *Journal of Applied Physics*, 59(10):3318–3327, 1986.

[38] CC Huang GS Couch DM Greenblatt EC Meng TE Ferrin EF Pettersen, TD Goddard. Ucsf chimera–a visualization system for exploratory research and analysis. *J Comput Chem*, 25(13):1605–12, 2004.

[39] Nadine Ehmann, Sebastian van de Linde, Amit Alon, Dmitrij Ljaschenko, Xi Zhen Keung, Thorge Holm, Annika Rings, Aaron DiAntonio, Stefan Hallermann, Uri Ashery, Manfred Heckmann, Markus Sauer, and Robert J. Kittel. Quantitative super-resolution imaging of bruchpilot distinguishes active zone states. *Nat Commun*, 5:–, August 2014.

[40] Albert Einstein. Ueber einen die erzeugung und verwandlung des lichtes betreffenden heuristischen gesichtspunkt. *Annalen der Physik*, 322:132–148, 1905.

[41] Albert Einstein. Strahlungs-emission und -absorption nach der quantentheorie. *Verhandlungen der Deutschen Physikalischen Gesellschaft*, 18:318–323, 1916.

[42] Rachid Sougrat O. Wolf Lindwasser Scott Olenych Juan S. Bonifacino Michael W. Davidson Jennifer Lippincott-Schwartz Eric Betzig, George H. Patterson and Harald F. Hess. Imaging intracellular fluorescent proteins at nanometer resolution. *Science*, 313 (5793):1652–1645, 2006.

[43] Lukas Novotny Erik J. Sanchez and X. Sunney Xie. Near-field fluorescence microscopy based on two-photon excitation with metal tips. *Phys. Rev. Lett.*, 82, 1999.

[44] Oliver P. Ernst, Verena Gramse, Michael Kolbe, Klaus Peter Hofmann, and Martin Heck. Monomeric g protein-coupled receptor rhodopsin in solution activates its g protein transducin at the diffusion limit. *Proceedings of the National Academy of Sciences*, 104(26):10859–10864, 2007.

[45] J. Franck and E. G. Dymond. Elementary processes of photochemical reactions. *Trans. Faraday Soc.*, 21:536–542, 1926.

[46] Joseph Fraunhofer. Bestimmung des brechungs- und des farben-zerstreuungs - vermoegens verschiedener glasarten, in bezug auf die vervollkommnung achromatischer fernrohre. *Denkschriften der Koeniglichen Akademie der Wissenschaften zu Muenchen*, 5:193–226, 1814-1815.

[47] Lord Rayleigh F.R.S. Xxxi. investigations in optics, with special reference to the spectroscope. *Philosophical Magazine Series 5*, 8(49):261–274, 1879.

[48] Stefan Geissbuehler, Claudio Dellagiacoma, and Theo Lasser. Comparison between sofi and storm. *Biomed. Opt. Express*, 2(3):408–420, Mar 2011.

[49] Derek Greenfield, Ann L. McEvoy, Hari Shroff, Gavin E. Crooks, Ned S. Wingreen, Eric Betzig, and Jan Liphardt. Self-organization of the escherichia coli chemotaxis network imaged with super-resolution light microscopy. *PLoS Biol*, 7(6):e1000137, 06 2009.

[50] Jean-Baptiste Sibarita Daniel Choquet Laurent Cogne Gregory Giannone, Eric Hosy. High content super-resolution imaging of live cell by upaint. *Methods Biol Mol,*, 950:95–110, 2013.

[51] Ulf Grenander. *Probability and Statistics: The Harald Cramer Volume - The Nyquist frequency is that frequency whose period is two sampling intervals.* Wiley, 1959.

[52] Joe Grove, Daniel J. Metcalf, Alex E. Knight, Silene T. Wavre-Shapton, Tony Sun, Emmanouil D. Protonotarios, Lewis D. Griffin, Jennifer Lippincott-Schwartz, and Mark Marsh. Flat clathrin lattices: stable features of the plasma membrane. *Molecular Biology of the Cell*, 25(22):3581–3594, 2014.

[53] Eckart D Gundelfinger and Anna Fejtova. Molecular organization and plasticity of the cytomatrix at the active zone. *Current Opinion in Neurobiology*, 22(3):423 – 430, 2012. Synaptic structure and function.

[54] M. G. L. Gustafsson. Surpassing the lateral resolution limit by a factor of two using structured illumination microscopy. *Journal of Microscopy*, 198(2):82–87, 2000.

[55] Mats G. L. Gustafsson. Nonlinear structured-illumination microscopy: Wide-field fluorescence imaging with theoretically unlimited resolution. *Proceedings of the National Academy of Sciences of the United States of America*, 102(37):13081–13086, 2005.

[56] G. Britton H.A. Frank, A.J. Young and R.J. Cogdell. *The Photochemistry of Carotenoids.* Kluwer Academic Publishers, Dordrecht, 1999.

[57] Mike Heilemann, Sebastian van de Linde, Mark Schuettpelz, Robert Kasper, Britta Seefeldt, Anindita Mukherjee, Philip Tinnefeld, and Markus Sauer. Subdiffraction-resolution fluorescence imaging with conventional fluorescent probes. *Angewandte Chemie International Edition*, 47(33):6172–6176, 2008.

[58] Stefan W. Hell, Steffen Lindek, Christoph Cremer, and Ernst H. K. Stelzer. Confocal microscopy with an increased detection aperture: type-b 4pi confocal microscopy. *Opt. Lett.*, 19(3):222–224, Feb 1994.

[59] Jonathan A. Hern, Asma H. Baig, Gregory I. Mashanov, Berry Birdsall, John E. T. Corrie, Sebastian Lazareno, Justin E. Molloy, and Nigel J. M. Birdsall. Formation and dissociation of m1 muscarinic receptor dimers seen by total internal reflection fluorescence imaging of single molecules. *Proceedings of the National Academy of Sciences*, 107(6):2693–2698, 2010.

[60] Harald Herrmann, Harald Baer, Laurent Kreplak, Sergei V. Strelkov, and Ueli Aebi. Intermediate filaments: from cell architecture to nanomechanics. *Nat Rev Mol Cell Biol*, 8(7):562–573, July 2007.

[61] Laurent Holtzer, Tobias Meckel, and Thomas Schmidt. Nanometric three-dimensional tracking of individual quantum dots in cells. *Applied Physics Letters*, 90(5):–, 2007.

[62] Hope E. Hopps, Barbara C. Bernheim, Ananda Nisalak, Joe Hin Tjio, and Joseph E. Smadel. Biologic characteristics of a continuous kidney cell line derived from the african green monkey. *The Journal of Immunology*, 91(3):416–424, 1963.

[63] Fang Huang, Tobias M P Hartwich, Felix E Rivera-Molina, Yu Lin, Whitney C Duim, Jane J Long, Pradeep D Uchil, Jordan R Myers, Michelle A Baird, Walther Mothes, Michael W Davidson, Derek Toomre, and Joerg Bewersdorf. Video-rate nanoscopy using scmos camera-specific single-molecule localization algorithms. *Nat Meth*, 10(7):653–658, July 2013.

[64] Tobias B. Huber, Bernhard Schermer, Roman Ulrich Mueller, Martin Hoehne, Malte Bartram, Andrea Calixto, Henning Hagmann, Christian Reinhardt, Fabienne Koos, Karl Kunzelmann, Elena Shirokova, Dietmar Krautwurst, Christian Harteneck, Matias Simons, Hermann Pavenstaedt, Dontscho Kerjaschki, Christoph Thiele, Gerd Walz, Martin Chalfie, and Thomas Benzing. Podocin and mec-2 bind cholesterol to regulate the activity of associated ion channels. *Proceedings of the National Academy of Sciences*, 103(46):17079–17086, 2006.

[65] F Hundt. Zur deutung der molekelspektren. *Zeitschrift fuer Physik*, 36:657–674, 1926.

[66] Eunjin Kim Jae-Won Kim Eun-Kyoung Hahm Myoung-Hwan Kim Sukhee Cho Jeongjin Kim Hyeran Jang Soo-Churl Cho Boong-Nyun Kim Min-Sup Shin Jinsoo Seo Jaeseung Jeong Se-Young Choi Daesoo Kim Changwon Kang Hyejung Won, Won Mah and Eunjoon Kim. Git1 is associated with adhd in humans and adhd-like behaviors in mice. *Nature Medicine*, 17:566–572, 2011.

[67] E Frise-I Frise J Schindelin, I Arganda-Carreras. Fiji: an open-source platform for biological-image analysis. *Nat. Methods*, 9(7):676–682, 2012.

[68] A. Jablonski. Efficiency of anti-stokes fluorescence in dyes. *Nature*, 131:839–840, 1933.

[69] Stephen T. Ross John R. Allen and Michael W. Davidson. Sample preparation for single molecule localization microscopy. *Phys. Chem. Chem. Phys.*, 15, 2013.

[70] Stephen T Ross John R Allen and Michael W Davidson. Single molecule localization microscopy for superresolution. *J Opt.*, 15, 2013.

[71] Evgenia Platonova Hadi Eghlidi & Helge Ewers Jonas Ries, Charlotte Kaplan. A simple, versatile method for gfp-based super-resolution microscopy via nanobodies. *Nat. Meth.*, 9:582 – 584, 2012.

[72] Chen Liu Junjia Liu and Wei He. Fluorophores and their applications as molecular probes in living cells. *Curr. Org. Chem.*, 17(6):564–579, 2013.

[73] Pakorn Kanchanawong, Gleb Shtengel, Ana M. Pasapera, Ericka B. Ramko, Michael W. Davidson, Harald F. Hess, and Clare M. Waterman. Nanoscale architecture of integrin-based cell adhesions. *Nature*, 468(7323):580–584, November 2010.

[74] Rinshi S. Kasai, Kenichi G. N. Suzuki, Eric R. Prossnitz, Ikuko Koyama-Honda, Chieko Nakada, Takahiro K. Fujiwara, and Akihiro Kusumi. Full characterization of gpcr monomer-dimer dynamic equilibrium by single molecule imaging. *The Journal of Cell Biology*, 192(3):463–480, 2011.

[75] M. Kasha and R. E. Powell. On the correlation of the spectroscopic and thermal energy differences between the fluorescence and phosphorescence levels of dye molecules. *Journal of the American Chemical Society*, 69(11):2909–2910, 1947.

[76] Michael. Kasha. Phosphorescence and the rle of the triplet state in the electronic excitation of complex molecules. *Chemical Reviews*, 41(2):401–419, 1947. PMID: 18901152.

[77] Liudmila Lapatsina Ha-Duong Ngo Kate Poole, Regina Herget and Gary R. Lewin. Tuning piezo ion channels to detect molecular-scale movements relevant for fine touch. *Nature Communications*, 5, 2014.

[78] Jan Keller, Andreas Schönle, and Stefan W. Hell. Efficient fluorescence inhibition patterns for resolft microscopy. *Opt. Express*, 15(6):3361–3371, Mar 2007.

[79] Seho Kim, Jaewon Ko, Hyewon Shin, Jae-Ran Lee, Chunghun Lim, Jin-Hee Han, Wilko D. Altrock, Craig C. Garner, Eckart D. Gundelfinger, Richard T. Premont,

Bong-Kiun Kaang, and Eunjoon Kim. The git family of proteins forms multimers and associates with the presynaptic cytomatrix protein piccolo. *Journal of Biological Chemistry*, 278(8):6291–6300, 2003.

[80] James A Spudich & Henrik Flyvbjerg Kim I Mortensen, L Stirling Churchman. Optimized localization analysis for single-molecule tracking and super-resolution microscopy. *Nat. Methods*, 7:377–381, 2010.

[81] K Kinosita, H Itoh, S Ishiwata, K Hirano, T Nishizaka, and T Hayakawa. Dual-view microscopy with a single camera: real-time imaging of molecular orientations and calcium. *The Journal of Cell Biology*, 115(1):67–73, 1991.

[82] Kathrin Klehs, Christoph Spahn, Ulrike Endesfelder, Steven F. Lee, Alexandre Fuerstenberg, and Mike Heilemann. Increasing the brightness of cyanine fluorophores for single-molecule and superresolution imaging. *ChemPhysChem*, 15(4):637–641, 2014.

[83] Teresa Klein, Sven Proppert, and Markus Sauer. Eight years of single-molecule localization microscopy. *Histochemistry and Cell Biology*, 141(6):561–575, 2014.

[84] Joseph R Lakowicz. *Principles of Fluorescence Spectroscopy*. Springer, New York, 3rd edition, 2006.

[85] Andre Lampe, Volker Haucke, Stephan J. Sigrist, Mike Heilemann, and Jan Schmoranzer. Multi-colour direct storm and with red and emitting carbocyanines. Biol. Cell (2012) 104, 229-237 DOI: 10.1111/boc.201100011 Research article, 2012.

[86] Andre Lampe, Georgi Tadeus, and Jan Schmoranzer. Spectral demixing avoids registration errors and reduces noise in multicolor localization-based super-resolution microscopy. *Methods and Applications in Fluorescence*, 3(3):034006, 2015.

[87] Sang-Hyuk Lee, Jae Yen Shin, Antony Lee, and Carlos Bustamante. Counting single photoactivatable fluorescent molecules by photoactivated localization microscopy (palm). *Proceedings of the National Academy of Sciences*, 109(43):17436–17441, 2012.

[88] Martin Lehmann, Benjamin Gottschalk, Dmytro Puchkov, Peter Schmieder, Sergej Schwagerus, Christian P. R. Hackenberger, Volker Haucke, and Jan Schmoranzer. Multicolor caged dstorm resolves the ultrastructure of synaptic vesicles in the brain. *Angewandte Chemie International Edition*, 54(45):13230–13235, 2015.

[89] Martin Lehmann, Gregor Lichtner, Haider Klenz, and Jan Schmoranzer. Novel organic dyes for multicolor localization-based super-resolution microscopy. *Journal of Biophotonics*, pages n/a–n/a, 2015.

[90] Sir John Lennard-Jones. The electronic structure of some diatomic molecules. *Transaction of the Faraday Society*, 25:668–686, 1929.

[91] Kate Poole Oliver Daumke Gary R. Lewin Liudmilla Lapatsina, Janko Brand. Stomatin-domain proteins. *Eur. J. Cell Biol.*, 91:240–245, 2012.

[92] Martin J Lohse. Dimerization in gpcr mobility and signaling. *Current Opinion in Pharmacology*, 10(1):53 – 58, 2010. {GPCR}.

[93] Damaris Nadia Lorenzo, Alexandra Badea, Jonathan Davis, Janell Hostettler, Jiang He, Guisheng Zhong, Xiaowei Zhuang, and Vann Bennett. A pik3c3-ankyrin-b-dynactin pathway promotes axonal growth and multiorganelle transport. *The Journal of Cell Biology*, 207(6):735–752, 2014.

[94] Richard Lundmark and Sven R. Carlsson. Sorting nexin 9 participates in clathrin-mediated endocytosis through interactions with the core components. *Journal of Biological Chemistry*, 278(47):46772–46781, 2003.

[95] Naoko Imamoto Makio Tokunaga and Kumiko Sakata-Sogawa. Highly inclined thin illumination enables clear single-molecule imaging in cells. *Nat. Methods*, 5:159–161, 2008.

[96] Mark D Lessard Michael J Mlodzianoski Bhupendra S Nagpure Brian T Bennett Samuel T Hess Manuel F Juette, Travis J Gould and Joerg Bewersdorf. Three-dimensional sub-100 nm resolution fluorescence microscopy of thick samples. *Nat. Methods*, 5:527–529, 2008.

[97] Graham T Dempsey Xiaowei Zhuang Mark Bates, Bo Huang. Multicolor super-resolution imaging with photo-switchable fluorescent probes. *Science*, 317:1749–1753, 2007.

[98] G.I. Mashanov and J.E. Molloy. Automatic detection of single fluorophores in live cells. *Biophysical Journal*, 92(6):2199–2211.

[99] David Klenerman Steven F. Lee Mathew H. Horrocks, Matthieu Palayret. The changing point spread function: single molecule based super-resolution imaging. *Histochem Cell Biol*, 141:577–585, 2014.

[100] Mark Bates Michael J. Rust and Xiaowei Zhuang. Stochastic optical reconstruction microscopy (storm) provides sub-diffraction-limit image resolution. *Nat. Methods*, 3(10):793–795, 2006.

[101] Mark Bates Michael J Rust and Xiaowei Zhuang. Sub-diffraction-limit imaging by stochastic optical reconstruction microscopy (storm). *Nat. Methods*, 3:793–796, 2006.

[102] Yu. V. Miklyaev, S. A. Asselborn, K. A. Zaytsev, and M. Ya. Darscht. Superresolution microscopy in far-field by near-field optical random mapping nanoscopy. *Applied Physics Letters*, 105(11):–, 2014.

[103] Barbara MÃŒller and Mike Heilemann. Shedding new light on viruses: superresolution microscopy for studying human immunodeficiency virus. *Trends in Microbiology*, 21(10):522–533, 2013.

[104] W. E. Moerner and David P. Fromm. Methods of single-molecule fluorescence spectroscopy and microscopy. *Review of Scientific Instruments*, 74(8):3597–3619, 2003.

[105] Ratnakar B. Mujumdar, Lauren A. Ernst, Swati R. Mujumdar, Christopher J. Lewis, and Alan S. Waggoner. Cyanine dye labeling reagents: Sulfoindocyanine succinimidyl esters. *Bioconjugate Chemistry*, 4(2):105–111, 1993. PMID: 7873641.

[106] R S Mulliken. Electronic states. iv. hund's theory; second positive nitrogen and swan bands; alternate intensities. *Phys. Rev.*, 29:637–649, 1927.

[107] Siddharth Nanguneri, Benjamin Flottmann, Heinz Horstmann, Mike Heilemann, and Thomas Kuner. Three-dimensional, tomographic super-resolution fluorescence imaging of serially sectioned thick samples. *PLoS ONE*, 7(5):e38098, 05 2012.

[108] Vinoth Sundar Rajan Pierre Goeonczy Nicolas Olivier, Debora Keller and Suliana Manley. Simple buffers for 3d storm microscopy. *Biomedical Optics Express*, 4, 2013.

[109] Shuming Nie and Richard N. Zare. Optical detection of single molecules. *Annu. Rev. Biophys. Biomol. Struct.*, 26:567–596, 1997.

[110] Christian Osseforth, Jeffrey R. Moffitt, Lothar Schermelleh, and Jens Michaelis. Simultaneous dual-color 3d sted microscopy. *Opt. Express*, 22(6):7028–7039, Mar 2014.

[111] A. Sundaramurthy G. S. Kino P. J. Schuck, D. P. Fromm and W. E. Moerner. Improving the mismatch between light and nanoscale objects with gold bowtie nanoantennas. *Phys. Rev. Lett.*, 94, 2005.

[112] O. J. F. Martin B. Hecht P. Muehlschlegel, H.-J. Eisler and D. W. Pohl. Resonant optical antennas. *Science*, 308 (5728):1607–1609, 2005.

[113] Mattia Greco Paolo Annibale, Marco Scarselli and Aleksandra Radenovic. Identification of the factors affecting co-localization precision for quantitative multicolor localization microscopy. *Optical Nanoscopy*, 1:9, 2012.

[114] Sri Rama Prasanna Pavani, Michael A. Thompson, Julie S. Biteen, Samuel J. Lord, Na Liu, Robert J. Twieg, Rafael Piestun, and W. E. Moerner. Three-dimensional, single-molecule fluorescence imaging beyond the diffraction limit by using a double-helix point spread function. *Proceedings of the National Academy of Sciences*, 106(9):2995–2999, 2009.

[115] JB Pawley, editor. *Handbook of Biological Confocal Microscopy*. Sringer, Berlin, 3rd edition, 2006.

[116] J.-P. Pin, L. Comps-Agrar, D. Maurel, C. Monnier, M. L. Rives, E. Trinquet, J. Kniazeff, P. Rondard, and L. Prezeau. G-protein-coupled receptor oligomers: two or more for what? lessons from mglu and gabab receptors. *The Journal of Physiology*, 587(22):5337–5344, 2009.

[117] Jasmin Podufall, Rui Tian, Elena Knoche, Dmytro Puchkov, AlexanderÂ M. Walter, Stefanie Rosa, Christine Quentin, Anela Vukoja, Nadja Jung, Andre Lampe, Carolin Wichmann, Mathias Boehme, Harald Depner, YongÂ Q. Zhang, Jan Schmoranzer, Stephan J. Sigrist, and Volker Haucke. A presynaptic role for the cytomatrix protein git in synaptic vesicle recycling. *Cell Reports*, 7(5):1417 – 1425, 2014.

[118] Sven Proppert, Steve Wolter, Thorge Holm, Teresa Klein, Sebastian van de Linde, and Markus Sauer. Cubic b-spline calibration for 3d super-resolution measurements using astigmatic imaging. *Opt. Express*, 22(9):10304–10316, May 2014.

[119] M. Mueller R. Hermann, P. Walther. Immunogold labeling in scanning electron microscopy. *Histochemistry and Cell Biology*, 106 (1):31–39, 1996.

[120] Soren G. F. Rasmussen, Brian T. DeVree, Yaozhong Zou, Andrew C. Kruse, Ka Young Chung, Tong Sun Kobilka, Foon Sun Thian, Pil Seok Chae, Els Pardon,

Diane Calinski, Jesper M. Mathiesen, Syed T. A. Shah, Joseph A. Lyons, Martin Caffrey, Samuel H. Gellman, Jan Steyaert, Georgios Skiniotis, William I. Weis, Roger K. Sunahara, and Brian K. Kobilka. Crystal structure of the [bgr]2 adrenergic receptor-gs protein complex. *Nature*, 477(7366):549–555, September 2011.

[121] Matthias Reuss, Johann Engelhardt, and Stefan W. Hell. Birefringent device converts a standard scanning microscope into a sted microscope that also maps molecular orientation. *Opt. Express*, 18(2):1049–1058, Jan 2010.

[122] Eugenio F Fornasiero Flavia Valtorta Christophe Zimmer & Musa M Mhlanga Ricardo Henriques, Mickael Lelek. Quickpalm: 3d real-time photoactivation nanoscopy image processing in imagej. *Nat. Methods*, 7:339–340, 2010.

[123] J Roth and M Binder. Coloidal gold, ferritin and peroxidase as markers for electron microscopic double labeling lectin techniques. *Journal of Histochemistry & Cytochemistry*, 26(3):163–9, 1978.

[124] Cecile Rose T. Vibat Norman Huang Chang-Wook Lee Rupak Doshi, Beverly R. Chen and Geoffrey Chang. In vitro nanobody discovery for integral membrane protein targets. *Scientific Reports*, 4, 2014.

[125] Daniel Sage, Hagai Kirshner, Thomas Pengo, Nico Stuurman, Junhong Min, Suliana Manley, and Michael Unser. Quantitative evaluation of software packages for single-molecule localization microscopy. *Nat Meth*, 12(8):717–724, August 2015.

[126] Lothar Schermelleh, Peter M. Carlton, Sebastian Haase, Lin Shao, Lukman Winoto, Peter Kner, Brian Burke, M. Cristina Cardoso, David A. Agard, Mats G. L. Gustafsson, Heinrich Leonhardt, and John W. Sedat. Subdiffraction multicolor imaging of the nuclear periphery with 3d structured illumination microscopy. *Science*, 320(5881):1332–1336, 2008.

[127] Lothar Schermelleh, Rainer Heintzmann, and Heinrich Leonhardt. A guide to super-resolution fluorescence microscopy. *The Journal of Cell Biology*, 190(2):165–175, 2010.

[128] Teresa Klein Meike Heidbreder Steve Wolter-Mike Heilemann Sebastian van de Linde, Anna Loeschberger and Markus Sauer. Direct stochastic optical reconstruction microscopy with standard fluorescent probes. *Nature Protocols*, 6:991–1009, 2011.

[129] CLAUDE E. SHANNON. Communication in the presence of noise. *Proc. Institute of Radio Engineers*, 37:10–21, 1949.

[130] Daria M Shcherbakova, Prabuddha Sengupta, Jennifer Lippincott-Schwartz, and Vladislav V Verkhusha. Photocontrollable fluorescent proteins for superresolution imaging. *Annual review of biophysics*, 43:303–329, 2014.

[131] Edward Hujber Richard D. Fetter Jackson Richards Berit Soehl-Kielczynski Annegret Felies Christian Rosenmund Jan Schmoranzer Erik M. Jorgensen Shigeki Watanabe, Martin Lehmann. Nanometer-resolution fluorescence electron microscopy (nano-em) in cultured cells. *Methods Mol. Biol.*, 1117:503–526, 2014.

[132] Narae Shin, Namhui Ahn, Belle Chang-Ileto, Joohyun Park, Kohji Takei, Sang-Gun Ahn, Soo-A Kim, Gilbert Di Paolo, and Sunghoe Chang. Snx9 regulates tubular invagination of the plasma membrane through interaction with actin cytoskeleton and dynamin 2. *Journal of Cell Science*, 121(8):1252–1263, 2008.

[133] Galbraith J A White H Gillette J Olenych S Davidson M W Shroff H, Galbraith C G and Betzig E. Dual-color superresolution imaging of genetically expressed probes within individual adhesion complexes. *Proc. Natl Acad. Sci.*, 104:20308 – 20313, 2007.

[134] Thorge Holm Sarah Aufmkolk Marie-Christine Dabauvalle Sebastian van de Linde Steve Wolter, Anna Loeschberger and Markus Sauer. rapidstorm: accurate, fast open-source software for localization microscopy. *Nature Methods*, 9:1040–1041, 2012.

[135] G. G. Stokes. On the change of refrangibility of light. *Philos. Trans. Roy. Soc. London*, 142:463–562, 1852.

[136] Abhishek Chadha Boaz Cook Sung Eun Kim, Bertrand Coste and Ardem Patapoutian. The role of drosophila piezo in mechanical nociception. *Nature*, 483:209–212, 2012.

[137] G. Iyer S. Weiss T. Dertinger, R. Colyer and J. Enderlein. Fast, background-free, 3d super-resolution optical fluctuation imaging (sofi). *PNAS*, 106 no. 52:22287–22292, 2009.

[138] Georgi Tadeus, Andre Lampe, and Jan Schmoranzer. Sdmixer - a versatile software tool for spectral demixing of multicolor single molecule localization data. *Methods and Applications in Fluorescence*, 3(3):037001, 2015.

[139] Anke Teichmann, Arthur Gibert, Andre Lampe, Paul Grzesik, Claudia Rutz, Jens Furkert, Jan Schmoranzer, Gerd Krause, Burkhard Wiesner, and Ralf Schuelein. The specific monomer/dimer equilibrium of the corticotropin-releasing factor receptor type 1 is established in the endoplasmic reticulum. *Journal of Biological Chemistry*, 289(35):24250–24262, 2014.

[140] Anke Teichmann, Claudia Rutz, Annika Kreuchwig, Gerd Krause, Burkhard Wiesner, and Ralf Schuelein. The pseudo signal peptide of the corticotropin-releasing factor receptor type 2a prevents receptor oligomerization. *Journal of Biological Chemistry*, 287(32):27265–27274, 2012.

[141] Markus Sauer Teresa Klein, Sven Proppert. Eight years of single-molecule localization microscopy. *Histochem Cell Biol*, 141:561–575, 2014.

[142] Sven Proppert Steve Wolter Sebastian van de Linde Teresa Klein, Anna Loeschberger and Markus Sauer. Live-cell dstorm with snap-tag fusion proteins. *Nat. Methods*, 8:7–9, 2011.

[143] Sonia Terrillon and Michel Bouvier. Roles of g-protein-coupled receptor dimerization. *EMBO reports*, 5(1):30–34, 2004.

[144] Medda R Rothermel E von Middendorf C Foelling J Jakobs S Schoenle A Hell S W Testa I, Wurm C A and Eggeling C. Multicolor fluorescence nanoscopy in fixed and living cells by exciting conventional fluorophores with a single wavelength. *Biophys. J.*, 2010.

[145] Gorge J. Todaro and Howard Green. Quantitative studies of the growth of mouse embryo cells in culture and their development into established lines. *J Cell Biol.*, 17(2):299–313, 1963.

[146] B Trzaskowski, D Latek, S Yuan, U Ghoshdastider, A Debinski, and S Filipek. Action of molecular switches in gpcrs - theoretical and experimental studies. *Current Medicinal Chemistry*, 19(8):1090–1109, January 2011.

[147] Lynne Turnbull, Michael P. Strauss, Andrew T. F. Liew, Leigh G. Monahan, Cynthia B. Whitchurch, and Elizabeth J. Harry. Super-resolution imaging of the cytokinetic z ring in live bacteria using fast 3d-structured illumination microscopy (f3d-sim). (91):e51469–, 2014.

[148] Nicolai T. Urban, Katrin I. Willig, Stefan W. Hell, and U. Valentin Naegerl. Sted nanoscopy of actin dynamics in synapses deep inside living brain slices. *Biophysical Journal*, 101(5):1277 – 1284, 2011.

[149] Eneko Urizar, Lucia Montanelli, Tiffany Loy, Marco Bonomi, Stéphane Swillens, Céline Gales, Michel Bouvier, Guillaume Smits, Gilbert Vassart, and Sabine Costagliola. Glycoprotein hormone receptors: link between receptor homodimerization and negative cooperativity. *The EMBO Journal*, 24(11):1954–1964, 2005.

[150] Sebastian van de Linde, Ulrike Endesfelder, Anindita Mukherjee, Mark Schuttpelz, Gerd Wiebusch, Steve Wolter, Mike Heilemann, and Markus Sauer. Multicolor photoswitching microscopy for subdiffraction-resolution fluorescence imaging. *Photochem. Photobiol. Sci.*, 8:465–469, 2009.

[151] Sebastian van de Linde, Ivan Krstic, Thomas Prisner, Soren Doose, Mike Heilemann, and Markus Sauer. Photoinduced formation of reversible dye radicals and their impact on super-resolution imaging. *Photochem. Photobiol. Sci.*, 10:499–506, 2011.

[152] Sebastian van de Linde and Markus Sauer. How to switch a fluorophore: from undesired blinking to controlled photoswitching. *Chem. Soc. Rev.*, 43, 2014.

[153] Jan Vogelsang, Robert Kasper, Christian Steinhauer, Britta Person, Mike Heilemann, Markus Sauer, and Philip Tinnefeld. A reducing and oxidizing system minimizes photobleaching and blinking of fluorescent dyes. *Angewandte Chemie International Edition*, 47(29):5465–5469, 2008.

[154] Kenneth D. Weston Volker Buschmann and Markus Sauer. Spectroscopic study and evaluation of red-absorbing fluorescent dyes. *Bioconjugate Chemistry*, 14(1):195–204, 2003. PMID: 12526709.

[155] Erwin Neher & Stephan J. Sigrist Volker Haucke. Protein scaffolds in the coupling of synaptic exocytosis and endocytosis. *Nat. Rev. Neurosci.*, 12:127–138, 2011.

[156] Sina Waeldchen, Julian Lehmann, Teresa Klein, Sebastian van de Linde, and Markus Sauer. Light-induced cell damage in live-cell super-resolution microscopy. *Scientific Reports*, 5:15348–, October 2015.

[157] C.A. Walker. *Handbook of Moire Measurement*. Series in Optics and Optoelectronics. CRC Press, 2003.

[158] T. A. Welch. A technique for high-performance data compression. *Computer*, 17(6):8–19, June 1984.

[159] Matthew R. Whorton, Michael P. Bokoch, SÃžren G. F. Rasmussen, Bo Huang, Richard N. Zare, Brian Kobilka, and Roger K. Sunahara. A monomeric g protein-coupled receptor isolated in a high-density lipoprotein particle efficiently activates its g protein. *Proceedings of the National Academy of Sciences*, 104(18):7682–7687, 2007.

[160] Charles S. Williams. *Introduction to the Optical Transfer Function*. SPIE - The International Society for Optical Engineering, 2002.

[161] William Hyde Wollaston. A method of examining refractive and dispersive powers, by prismatic reflection. *Philosophical Transactions of the Royal Society of London*, 92:365–380, 1802.

[162] Lei Yang, Alison R. Dun, Kirsty J. Martin, Zhen Qiu, Andrew Dunn, Gabriel J. Lord, Weiping Lu, Rory R. Duncan, and Colin Rickman. Secretory vesicles are preferentially targeted to areas of low molecular snare density. *PLoS ONE*, 7(11):e49514, Nov 2012.

[163] Defne Yarar, Mark C. Surka, Marilyn C. Leonard, and Sandra L. Schmid. Snx9 activities are regulated by multiple phosphoinositides through both px and bar domains. *Traffic*, 9(1):133–146, 2008.

[164] Mitsuru Okuda Seiji Hara Haruyuki Inoue Yasushi Oshikane, Toshihiko Kataoka and Motohiro Nakano. Observation of nanostructure by scanning near-field optical microscope with small sphere probe. *Science and Technology of Advanced Materials*, 8, 2007.

[165] Dmytro Puchkov Johannes Schoeneberg Alexander Ullrich Andre Lampe Rainer Mueller Sirus Zarbakhsh Federico Gulluni Emilio Hirsch Michael Krauss Carsten Schultz-Jan Schmoranzer Frank Noe York Posor, Marielle Eichhorn-Gruenig and Volker Haucke. Spatiotemporal control of endocytosis by phosphatidylinositol-3,4-bisphosphate. *Nature*, 499:233–237, 2013.

[166] Guisheng Zhong, Jiang He, Ruobo Zhou, Damaris Lorenzo, Hazen P Babcock, Vann Bennett, and Xiaowei Zhuang. Developmental mechanism of the periodic membrane skeleton in axons. *eLife*, 3, 2014.

[167] J. Ziv and A. Lempel. Compression of individual sequences via variable-rate coding. *IEEE Transactions on Information Theory*, 24(5):530–536, Sep 1978.

A. Publications by the author

- André Lampe, Volker Haucke, Stephan J. Sigrist, Mike Heilemann, and Jan Schmoranzer. Multi-colour direct storm with red emitting carbocyanines. Biol. Cell (2012) 104, 229-237 DOI: 10.1111/boc.201100011 Research article, 2012.

- York Posor, Marielle Eichhorn-Gruenig, Dmytro Puchkov, Johannes Schoeneberg, Alexander Ullrich, André Lampe, Rainer Müller, Sirus Zarbakhsh, Federico Gulluni, Emilio Hirsch, Michael Krauss, Carsten Schultz, Jan Schmoranzer, Frank Noé and Volker Haucke. Spatiotemporal control of endocytosis by phosphatidylinositol-3,4-bisphosphate. Nature, 499:233 237, 2013.

- Jasmin Podufall, Rui Tian, Elena Knoche, Dmytro Puchkov, Alexander M. Walter, Ste- fanie Rosa, Christine Quentin, Anela Vukoja, Nadja Jung, André Lampe, Carolin Wichmann, Mathias Böhme, Harald Depner, Yong Q. Zhang, Jan Schmoranzer, Stephan J. Sigrist, and Volker Haucke. A presynaptic role for the cytomatrix protein (GIT) in synaptic vesicle recycling. Cell Reports, 7(5):1417 1425, 2014.

- Anke Teichmann, Arthur Gibert, André Lampe, Paul Grzesik, Claudia Rutz, Jens Furkert, Jan Schmoranzer, Gerd Krause, Burkhard Wiesner, and Ralf Schuelein. The specic monomer/dimer equilibrium of the corticotropin-releasing factor receptor type 1 is estab- lished in the endoplasmic reticulum. Journal of Biological Chemistry, 289(35):2425024262, 2014.

- André Lampe, Georgi Tadeus, and Jan Schmoranzer. Spectral demixing avoids registration errors and reduces noise in multicolor localization-based super-resolution microscopy. Methods and Applications in Fluorescence, 3(3):034006, 2015.

- Georgi Tadeus, André Lampe, and Jan Schmoranzer. SDmixer - a versatile software tool for spectral demixing of multicolor single molecule localization data. Methods and Applications in Fluorescence, 3(3):037001, 2015.

- Christiane Wetzel, Simone Pifferi, Cristina Picci, Caglar Gök, Diana Hoffmann, Kiran K. Bali, André Lampe, Liudmila Lapatsina, Raluca Fleischer, Ewan St.

John Smith, Mirko Moroni, Luc Estebanez, Valerie Bégay, Johannes Kühnemund, Edgar Specker, Martin Neuenschwander, Jens Peter von Kries, Volker Haucke, Rohini Kuner, James F.A. Poulet, Jan Schmoranzer, Kate Poole and Gary R. Lewin. Small-molecule inhibition of STOML3 oligomerization reverses pathological mechanical hypersensitivity. Nature Neuroscience 20, 209-218 (2017).

B. SDmixer software

The principle of the used software was described in 5.2 on page 58. The Software was further developed in collaboration with Georgi Tadeus, who transferred the algorithm to the higher programming Language C++ and built in faster processing pipelines for the application in 3D SD-*d*STORM, as well as a graphical user interface. This is described in Tadeus et al. [138]. The Software was published as open source at GitHub and prebuilt binaries and Windows installer of the software, as well as the manual, are available at Source Forge. This software is compiled for 64 bit Windows Systems only. The important links are listed below.

- prebuilt binaries for Windows 64bit: http://sourceforge.net/projects/sdmixer/
- manual and example data-set: http://sourceforge.net/projects/sdmixer/files/
- source code: https://github.com/gtadeus/sdmixer2

I want to thank Georgi Tadeus for the inspiring and fruitful collaboration on this software project. The usability and speed of the software would be very poor without his work. Three dimensional spectral demixing *d*STORM would not be part of this thesis, had he not participated in the great challenge to push the resolution limit of our setup. I am very grateful that I had the opportunity to work and publish papers with him.

C. Script for laser control

The shown Python script was written by Ricardo Henriques [122] and was altered to fit the parameters of our used laser lines. The section called "dev power", line 135 to 165, was altered to fit the maximal and minimal intensities of our lasers to match the minimal and maximal values of the slider displayed by the software. This listing shows the whole script, as demanded by the author Ricardo Henriques. The original version of this script can be downloaded from

- https://code.google.com/p/quickpalm/downloads/list.

```
1  #!/usr/bin/env python
2  # Laser Control for QuickPALM
3  # Copyright (c) 2010, Ricardo Henriques
4  # All rights reserved.
5  # Redistribution and use in source and binary forms, with or without
6  # modification, are permitted provided that the following conditions are met:
7  #     * Redistributions of source code must retain the above copyright notice,
8  #       this list of conditions and the following disclaimer.
9  #     * Redistributions in binary form must reproduce the above copyright
10 #       notice, this list of conditions and the following disclaimer in the
11 #       documentation and/or other materials provided with the distribution.
12 #     * Neither the name of the author nor the names of its contributors
13 #       may be used to endorse or promote products derived from this software
14 #       without specific prior written permission.
15 #
16 # THIS SOFTWARE IS PROVIDED BY THE COPYRIGHT HOLDERS AND CONTRIBUTORS "AS IS"
17 # AND ANY EXPRESS OR IMPLIED WARRANTIES, INCLUDING, BUT NOT LIMITED TO, THE
18 # IMPLIED WARRANTIES OF MERCHANTABILITY AND FITNESS FOR A PARTICULAR PURPOSE
19 # ARE DISCLAIMED. IN NO EVENT SHALL THE COPYRIGHT OWNER OR CONTRIBUTORS BE
20 # LIABLE FOR ANY DIRECT, INDIRECT, INCIDENTAL, SPECIAL, EXEMPLARY, OR
21 # CONSEQUENTIAL DAMAGES (INCLUDING, BUT NOT LIMITED TO, PROCUREMENT OF
22 # SUBSTITUTE GOODS OR SERVICES; LOSS OF USE, DATA, OR PROFITS; OR BUSINESS
23 # INTERRUPTION) HOWEVER CAUSED AND ON ANY THEORY OF LIABILITY, WHETHER IN
24 # CONTRACT, STRICT LIABILITY, OR TORT (INCLUDING NEGLIGENCE OR OTHERWISE)
25 # ARISING IN ANY WAY OUT OF THE USE OF THIS SOFTWARE, EVEN IF ADVISED OF
26 # THE POSSIBILITY OF SUCH DAMAGE.
```

```
27
28 import wx, atexit, thread, serial, time, sys, os, ConfigParser
29
30 class LCFrame(wx.Frame):
31   logfile=None
32   show_log_gui = False
33
34   def __init__(self, *args, **kwds):
35     # Load configuration file
36     if '__file__' in dir():
37         cfgpath=os.path.split(os.path.abspath(__file__))[0]
38     else: # fix for py2exe
39         cfgpath=sys.prefix
40     cfgpath=os.path.join(cfgpath, "cfg.txt")
41     self.cfg=ConfigParser.ConfigParser()
42     self.cfg.readfp(open(cfgpath))
43
44     # Detect number of laser lines
45     sections = self.cfg.sections()
46     if "serial port" not in sections:
47         raise Exception, "invalid configuration file"
48     self.laserlabels = sections
49     self.laserlabels.remove("serial port")
50     self.laserlabels.sort()
51     self.nlines=len(self.laserlabels)
52     self._power=[0]*self.nlines
53     self._shutter=[0]*self.nlines
54
55     kwds["style"] = wx.DEFAULT_FRAME_STYLE
56     wx.Frame.__init__(self, *args, **kwds)
57     self.panel_2 = wx.Panel(self, -1)
58     self.panel_1 = wx.Panel(self, -1)
59     self.frame_1_statusbar = self.CreateStatusBar(1, 0)
60
61     self.wxLabel=[]
62     self.wxShutter=[]
63     self.wxPower=[]
64     self.wxPulse=[]
65     self.wxPulseD=[]
66
67     for laserlabel in self.laserlabels:
68       self.wxLabel.append(wx.StaticText(self.panel_1, -1, laserlabel))
69       self.wxShutter.append(wx.ToggleButton(self.panel_1, -1, "Shutter"))
70       self.wxPower.append(wx.Slider(self.panel_1, -1, 0, 0, 100,
```

```
71  style=wx.SL_HORIZONTAL|wx.SL_LABELS))
72        self.wxPulseD.append(wx.TextCtrl(self.panel_1, -1, "0.01",
73  style=wx.TE_CENTRE))
74        self.wxPulse.append(wx.Button(self.panel_1, -1, "Pulse"))
75
76      self.label_5 = wx.StaticText(self.panel_2, -1, " Repetitive pulsing... ")
77      self.combo_box_1 = wx.ComboBox(self.panel_2, -1,
78  choices=self.laserlabels, style=wx.CB_DROPDOWN|wx.CB_READONLY)
79      self.text_ctrl_2 = wx.TextCtrl(self.panel_2, -1, "1",
80  style=wx.TE_CENTRE)
81      self.button_2 = wx.ToggleButton(self.panel_2, -1, "Start pulsing")
82      self.path = wx.TextCtrl(self, -1, "Copy directory root here...")
83      self.prefix = wx.TextCtrl(self, -1, "Copy name prefix here...")
84      self.button_1 = wx.ToggleButton(self, -1, "Observe Acquisition")
85
86      self.__set_properties()
87      self.__do_layout()
88
89      mybind = lambda evt, f, n, obj: self.Bind(evt, lambda e: f(n), obj)
90      for n in xrange(len(self.laserlabels)):
91        mybind(wx.EVT_TOGGLEBUTTON, self.actionShutter, n, self.wxShutter[n])
92        mybind(wx.EVT_COMMAND_SCROLL, self.actionPower, n, self.wxPower[n])
93        mybind(wx.EVT_COMMAND_SCROLL_ENDSCROLL, self.actionPower, n, self.wxPower[n])
94        mybind(wx.EVT_BUTTON, self.actionPulse, n, self.wxPulse[n])
95
96      self.Bind(wx.EVT_TOGGLEBUTTON, self.actionStartPulsing, self.button_2)
97      self.Bind(wx.EVT_TOGGLEBUTTON, self.actionObserveAcquisition, self.button_1)
98
99      # Prepare threads and initialize AOTF connection
100     self.lock=thread.allocate_lock()
101     #   note, on PySerial lib the serial ports are N-1,
102     #   so serial 2 will be represented by 1
103     self.nserial=self.cfg.getint("serial port", "number")-1
104     if self.nserial == -1: # Emulation mode
105       self.aotfcmd = lambda cmd: 1
106     else: # Not emulating
107       self.aotf=serial.Serial(self.nserial, 19200, timeout=1)
108       atexit.register(self.aotf.close)
109       self.aotfcmd('i0')
110     self._lastcmd_=time.time()
111     for n in range(self.nlines):
112       self.shutter(n+1,0)
113       self.power(n+1,0)
114     thread.start_new(self.__pulsing__, ())
```

```
115
116   def aotfcmd(self, cmd, wait=0):
117     self.lock.acquire()
118     self.aotf.write(cmd+"\r")
119     if wait:
120         msg=''
121         for n in xrange(10000):
122           c=self.aotf.read()
123           msg+=c
124           if c=='?': break
125     self.lock.release()
126     self._lastcmd_=time.time()
127
128   def shutter(self, channel=1, on=True):
129     if self._shutter[channel-1]==on: return
130     self.aotfcmd("x%d" % (channel), 1)
131       if on: self.aotfcmd("o1", 1)
132     else: self.aotfcmd("o0", 1)
133     self._shutter[channel-1]=on
134
135   def power(self, channel, percentage):
136     # print "entered power"
137     # print (repr(channel))
138     channel = int(channel)
139     if self._power[channel-1]==percentage: return
140     if channel == 5:
141       p=(float(percentage)/100.)*1023 # 661nm (not gauged yet)
142       # print "nothing"
143     if channel == 4:
144       p=(float(percentage)/100.)*872 # 643nm (1st gauge: 880)
145       # print "3 baby"
146     elif channel == 3:
147       p=(float(percentage)/100.)*845 # 568nm (1st gauge: 880)
148       # print "2 baby"
149     elif channel == 2:
150       p=(float(percentage)/100.)*850 # 488nm (1st gauge: 849)
151       # print "1 baby"
152     elif channel == 1:
153       p=(float(percentage)/100.)*734 # 405nm (1st gauge: 757)
154       # print "0 baby"
155     else:
156       p=(float(percentage)/100.)*1023 # else call
157
158     # p=(float(percentage)/100.)*1023
```

```
159     if p>1023: p=1023
160     elif p<0: p=0
161     p=int(round(p))
162     self.aotfcmd("l%dp%s\n\n" % (channel, str(p).zfill(4)))
163     self._power[channel-1]=percentage
164 
165   def __set_properties(self):
166     self.SetTitle("Laser Control for QuickPALM V1.0.3(Berlin)")
167     self.frame_1_statusbar.SetStatusWidths([-1])
168     # statusbar fields
169     frame_1_statusbar_fields = ["Copyright Ricardo Henriques @ Pasteur - 2010"]
170     for i in range(len(frame_1_statusbar_fields)):
171             self.frame_1_statusbar.SetStatusText(frame_1_statusbar_fields[i], i)
172 
173     for n in range(self.nlines):
174       self.wxShutter[n].SetToolTipString(self.laserlabels[n]+" shutter")
175       self.wxPower[n].SetToolTipString("change power")
176       self.wxPulseD[n].SetToolTipString("pulse duration in seconds")
177       self.wxPulse[n].SetToolTipString("make a single pulse")
178       self.combo_box_1.SetToolTipString("laser that will pulse")
179 
180    self.combo_box_1.SetSelection(0)
181    self.text_ctrl_2.SetToolTipString("pulse interval in seconds")
182    self.button_2.SetToolTipString("Rock and Roll!!!")
183 
184 
185   def __do_layout(self):
186     sizer_1 = wx.FlexGridSizer(5, 1, 0, 0)
187     sizer_3 = wx.BoxSizer(wx.HORIZONTAL)
188     grid_sizer_1 = wx.GridSizer(self.nlines, 4, 0, 0)
189 
190     for n in range(self.nlines):
191       grid_sizer_1.Add(self.wxLabel[n], 0,
192 wx.ALIGN_CENTER_HORIZONTAL|wx.ALIGN_CENTER_VERTICAL, 0)
193       grid_sizer_1.Add(self.wxShutter[n], 0,
194 wx.ALIGN_CENTER_HORIZONTAL|wx.ALIGN_CENTER_VERTICAL|wx.SHAPED, 0)
195       grid_sizer_1.Add(self.wxPower[n], 0,
196 wx.ALIGN_CENTER_HORIZONTAL|wx.ALIGN_CENTER_VERTICAL|wx.SHAPED, 0)
197       pulsesizer = wx.BoxSizer(wx.VERTICAL)
198       pulsesizer.Add(self.wxPulseD[n], 0, wx.EXPAND, 0)
199       pulsesizer.Add(self.wxPulse[n], 0,
200 wx.ALIGN_CENTER_HORIZONTAL|wx.ALIGN_CENTER_VERTICAL|wx.SHAPED, 0)
201       grid_sizer_1.Add(pulsesizer, 1, wx.EXPAND, 0)
202 
```

```
203       self.panel_1.SetSizer(grid_sizer_1)
204       sizer_1.Add(self.panel_1, 1, wx.EXPAND, 0)
205       sizer_3.Add(self.label_5, 0,
206   wx.ALIGN_CENTER_HORIZONTAL|wx.ALIGN_CENTER_VERTICAL, 0)
207       sizer_3.Add(self.combo_box_1, 1, 0, 0)
208       sizer_3.Add(self.text_ctrl_2, 0, 0, 0)
209       sizer_3.Add(self.button_2, 0, 0, 0)
210       self.panel_2.SetSizer(sizer_3)
211       sizer_1.Add(self.panel_2, 1, wx.EXPAND, 0)
212       #sizer_1.Add(self.path, 0, wx.EXPAND, 0)
213       #sizer_1.Add(self.prefix, 0, wx.EXPAND, 0)
214       #sizer_1.Add(self.button_1, 0, wx.EXPAND, 0)
215       if not self.show_log_gui:
216         self.path.Hide()
217         self.prefix.Hide()
218         self.button_1.Hide()
219       self.SetSizer(sizer_1)
220       sizer_1.Fit(self)
221       sizer_1.AddGrowableRow(0)
222       self.Layout()
223
224     def actionShutter(self, n):
225       line = self.cfg.getint(self.laserlabels[n], "line")
226       self.shutter(line, self.wxShutter[n].GetValue())
227       msg='SHUTTER %s: TIME %.8f AOTF %.2f STATUS %d' %
228   (self.laserlabels[n], time.time(), self.wxPower[n].GetValue(),
229    self.wxShutter[n].GetValue())
230       self.msg(msg)
231
232     def actionPower(self, n):
233       line = self.cfg.getint(self.laserlabels[n], "line")
234       power= self.wxPower[n].GetValue()
235       self.power(line, power)
236       if self.wxShutter[n].GetValue():
237         msg='POWER %s: TIME %.8f AOTF %.2f' % (self.laserlabels[n],
238          time.time(), power)
239         self.msg(msg)
240
241     def actionPulse(self, n):
242       line = self.cfg.getint(self.laserlabels[n], "line")
243       wait=float(self.wxPulseD[n].GetValue())
244       start=time.time()
245       self.shutter(line, 1)
246       time.sleep(wait)
```

```
247      self.shutter(line, 0)
248      stop=time.time()
249      msg='PULSE %s: START %.8f STOP %.8f DURATION %.8f' %
250  (self.laserlabels[n], start, stop, stop-start)
251      self.msg(msg)
252
253    def actionStartPulsing(self, event):
254      if event: event.Skip()
255      pass
256
257    def __pulsing__(self):
258      while 1:
259       try:
260         if self.button_2.GetValue():
261            interval=float(self.text_ctrl_2.GetValue())
262            n=self.laserlabels.index(self.combo_box_1.GetValue())
263            self.actionPulse(n)
264            time.sleep(interval)
265         except:
266            time.sleep(0.1)
267
268    def actionObserveAcquisition(self, event):
269      if event: event.Skip()
270      if self.button_1.GetValue():
271        targetdir=None
272        path=self.path.GetValue()
273        files = os.listdir(path)
274        files.sort(lambda x,y:cmp(os.path.getmtime(os.path.join(path,
275  x)),os.path.getmtime(os.path.join(path, y))))
276        files.reverse()
277        for filename in files:
278          if self.prefix.GetValue() in filename and
279  os.path.isdir(os.path.join(path, filename)):
280            targetdir=os.path.join(path, filename)
281            break
282          if targetdir!=None:
283            self.SetStatusText('Observing %s' % targetdir)
284            self.logfile=os.path.join(targetdir, 'aotflog.txt')
285            started=os.path.getctime(targetdir)
286            msg='STARTED: TIME %.8f ' % started
287            self.msg(msg)
288            for n in range(self.nlines):
289              self.actionPower(n)
290       else:
```

```
291         path=os.path.split(self.logfile)[0]
292         filetimes={}
293         for filename in os.listdir(path):
294           if '.tif' in filename:
295               filepath=os.path.join(path, filename)
296               mtime=os.path.getmtime(filepath)
297               filetimes[mtime]=filename
298 
299         self.logfile=None
300 
301   def msg(self, txt):
302     if self.logfile!=None:
303       open(self.logfile, 'a').write(txt+'\n')
304     #self.SetStatusText(txt)
305 
306 if __name__ == "__main__":
307   PALMControl = wx.PySimpleApp(0)
308   wx.InitAllImageHandlers()
309   try:
310     frame_1 = LCFrame(None, -1, "")
311     PALMControl.SetTopWindow(frame_1)
312         frame_1.Show()
313         PALMControl.MainLoop()
314   except Exception, err:
315     msg=wx.MessageDialog(None, str(err), "Error: "+str(type(err)),
316 style=wx.ICON_ERROR)
317       msg.ShowModal()
318       raise Exception, msg
```

free paper!